

DIGITAL ACCESS TO SCHOLARSHIP AT HARVARD
DASH.HARVARD.EDU

HARVARD LIBRARY


Mechanistic Studies of the Microtubule-Based Motors Dynein and Kinesin-8

Citation

Hernandez-Lopez, Rogelio Antonio. 2015. Mechanistic Studies of the Microtubule-Based Motors Dynein and Kinesin-8. Doctoral dissertation, Harvard University, Graduate School of Arts & Sciences.

Link

http://nrs.harvard.edu/urn-3:HUL.InstRepos:17467496

Terms of use

This article was downloaded from Harvard University's DASH repository, and is made available under the terms and conditions applicable to Other Posted Material (LAA), as set forth at
https://harvardwiki.atlassian.net/wiki/external/NGY5NDE4ZjgzNTc5NDQzMGIzZWZhMGFlOWI2M2EwYTg

Accessibility

https://accessibility.huit.harvard.edu/digital-accessibility-policy

Share Your Story

The Harvard community has made this article openly available.
Please share how this access benefits you. Submit a story

MECHANISTIC STUDIES OF THE MICROTUBULE-BASED MOTORS DYNEIN AND KINESIN-8

A dissertation presented
by
Rogelio Antonio Hernandez-Lopez

to
The Department of Chemistry and Chemical Biology

in partial fulfillment of the requirements

for the degree of

Doctor of Philosophy

in the subject of

Chemical Physics

Harvard University

Cambridge, Massachusetts

April 2015

© 2015 –Rogelio Antonio Hernandez-Lopez

All rights reserved.

Research Advisor: Professor Andres E. Leschziner Rogelio Antonio Hernandez-Lopez

Mechanistic studies of the microtubule-based motors dynein and kinesin-8

Abstract

The precise delivery and organization of intracellular factors in space and time relies on a set of molecules that move along and regulate the dynamics of cytoskeletal filaments. The two families of microtubule-based motors-- dyneins and kinesins-- power vital biological processes such as intracellular transport, chromosome segregation and more broadly cell-cell communication and cell polarization. Despite their role in such diverse activities, their molecular mechanisms remain poorly understood. Combining biochemistry, cryo-electron microscopy, molecular dynamics simulations and single molecule biophysics, we provide novel insights into the mechanistic basis of how dynein and kinesin-8 interact with microtubules (MTs) to regulate their function.

Cytoplasmic dynein is a homodimer that moves for long distances along MTs without dissociating, a property known as processivity. Its movement requires coupling cycles of ATP binding and hydrolysis to changes in affinity for its track. Intriguingly, the main site of ATP hydrolysis in the motor is separated from the microtubule binding domain (MTBD) by 25 nm. *How do these sites communicate with each other? What are the changes responsible for modulating the affinity between the motor and its track during dynein's mechanochemical cycle?* Furthermore, it has been shown that dynein's stepping behavior is highly variable. Dynein walks by taking a broad distribution of step sizes; some of its steps are sideways and some are backwards. *Is dynein's stepping behavior dictated by the motor's ATPase activity or dynein's affinity for MTs?* To

address these important questions, first, we solved a cryo-EM reconstruction of dynein's MTBD bound to the MT. We found that upon MT binding, dynein's MTBD undergoes a large conformational change underlying changes in its affinity for MTs. Our structural model suggested specific negatively charged residues within the MTBD that tune dynein's affinity for MTs. We mutated these residues to alanine and show a dramatic increase in dynein's MT binding affinity resulting in enhanced (~5-6 fold) motor processivity. These mutants provide us with a tool to explore the role of MT-binding affinity in dynein's stepping behavior. We characterized, using single molecule experiments, the stepping pattern of the high MT binding affinity dyneins. We found that an increased MT-binding affinity reduces dynein's stepping rate and impairs the coupling between ATPase activity and stepping. Together, our results provide a model for how dynein has evolved a finely tuned mechanism that allows its MTBD to communicate MT-binding to its motor domain. This mechanism also regulates dyneins's affinity for the MT and motor's processivity.

We then sought to understand the unique functional properties of kinesin-8. Unlike other kinesins that have the ability to either move along microtubules or regulate the dynamics of MT-ends, kinesin-8s can do both. Kip3, the budding yeast kinesin-8, is a highly processive motor capable of dwelling at the MT plus-end and it is a MT depolymerase. Given the highly conserved sequence and structure of kinesin's motor domain, *how is that Kip3 can perform these two distinct functions? Does Kip3 interact with the MT-lattice in the same manner than that at the MT-end?* We characterized, structurally, how Kip3 binds to microtubules that mimic the MT-lattice and the MT-end. We have identified and tested specific residues within Kip3 that are responsible for Kip3's processivity, MT-end dwelling and depolymerization activity.

Table of Contents

Chapter 1 Introduction **1**

Overview of cytoskeletal motors and their function in cells 2

Microtubules - structure and dynamics 5

Dynein - structure and function 8

The mechanism behind dynein stepping 12

Kinesin-8 : Overview and functions 13

Structural biology of microtubule-based motors and microtubule-associated proteins 16

Summary of results presented in this thesis 32

References 33

Chapter 2 Structural basis for microtubule binding and release by dynein **39**

Contributions 40

Abstract 41

Introduction 42

Materials and Methods 45

Results 58

Acknowledgements 86

References 87

Chapter 3 Regulatory role of the microtubule binding domain in dynein's stepping behavior **91**

Contributions 92

Abstract 93

Introduction 94

Materials and Methods 99

Results 104

Discussion 119

Acknowledgements 125

References 125

Chapter 4 Structural basis for processive motility and microtubule depolymerase activity by the yeast kinesin-8/Kip3 128

Contributions 129

Abstract 130

Introduction 131

Materials and Methods 135

Results 145

Discussion 156

Acknowledgements 168

References 168

List of figures

Figure 1.1 Schematic views of cytoplasmic dynein and kinesin-8. 4

Figure 1.2 Schematic view of helical and non-helical microtubules 6

Figure 1.3 Buttress movement initiates helix sliding in dynein's stalk 11

Figure 1.4 Three-dimensional reconstruction of proteins bound to microtubules from electron microscopy images of frozen hydrated samples 19

Figure 1.5 Diffraction pattern of a helix 25

Figure 1.6 Sindelar's method for 3D reconstruction of motors bound to MTs with a seam. 26

Figure 1.7 Processing pipeline for 3D reconstruction of motors bound to microtubules with a seam. Multi reference alignment, helical search and reconstruction. 27

Figure 2-1. Cryo-EM reconstruction of the cytoplasmic dynein high-affinity MTBD bound to a MT. 44

Figure 2-2. Three dimensional reconstruction of dynein's MTBD bound to the microtubule. 59

Figure 2.3. Complete reconstruction of the high-affinity SRS-MTBD construct bound to a MT. 60

Figure 2.4. The high-affinity, MT-bound state of the dynein MTBD is characterized by repositioning of helices H1 and CC1. 62

Figure 2.5. Molecular Dynamics study of the dynein MTBD conformations bound to MTs. 63

Figure 2.6. Comparison of 10 Å synthetic maps of the low- and high-affinity MTBD conformations with our experimental map. 64

Figure 2.7. Different atomic resolution structures of the MTBD converge on a single MT-bound conformation. 66

Figure 2.8. Conserved intermolecular MTBD-MT and intramolecular MTBD interactions in the dynein high-affinity state. 69

Figure 2.9. Formation of hydrogen bonds between the dynein MTBD and tubulin during MD simulations. 70

Figure 2.10. Effect of increasing ionic strength on dynein motility. 71

Figure 2.11. Behavior of dynamic salt bridges in the MTBD as determined by MD. 75

Figure 2.12. Dynamic salt bridges in H1 and H6 of the MTBD as observed by MD simulations. 76

Figure 2.13. Dynamic salt bridges reduce dynein motility. 77

Figure 2.14. Dynamic salt bridges temper dynein motility 78

Figure 2.15. Dynamic salt bridge mutations increase dynein processivity under more stringent motility conditions. 80

Figure 2.16. Dynamic salt bridge mutations increase dynein processivity independent of tubulin E-hooks. 81

Figure 2.17. Intraflagellar transport dynein (cytoplasmic dynein 2) lacks a key intramolecular salt bridge that tunes the affinity of cytoplasmic dynein. 82

Figure 3.1. Schematic structure of a dynein dimer. 95

Figure 3.2. Two possible models to explain dynein's variable step size distribution 98

Figure 3.3 Single point mutations in dynein's microtubule binding domain (MTBD) increase its affinity for microtubules. 107

Figure 3.4 Stepping behavior of head-labeled GST-Dyn331KDa WT and MTBD high affinity mutants. 110

Figure 3.5 On-axis dynein stepping of head-labeled GST-Dynein331kDa wild-type and MTBD high affinity mutants. 112

Figure 3.6 An increased affinity for MTs reduces dynein's stepping rate. 113

Figure 3.7 The E3107K mutation causes dynein to take longer on-axis steps 116

Figure 3.8 Dynein's catalytic cycle and rates constants of head-labeled WT dynein 117

Figure 4.1 The yeast kinesin8/Kip3 is a highly processive plus-end directed motor that is able to dwell at MT-ends and alter their dynamics. 133

Figure 4.2. High resolution Cryo-EM structure of Kip3 bound to Taxol-stabilized microtubules. 148

Figure 4.3 Cryo-EM reconstructions of Kip3 bound to the MTs stabilized by taxol or GMPCPP. 150

Figure 4.4 Key residues in Kip3's loop 11, loop8 and loop 12 regulate its processivity, dwell time and depolymerization activity. 154

Figure 4.5 Kip3 specific L1 and L2 inserts are dispensable for motility and depolymerization in vitro 158

Figure 4.6 Representative Micrographs and classification of different data sets. 159

Figure 4.7 Resolution analysis of Kip3-MTs (GDP-Taxol) 3D reconstruction. 160

Figure 4.8 Cryo-EM densities of selected regions of tubulin (GDP-taxol) 161

Figure 4.9 Comparison of the MT-bound yeast/Kip3 and free human/Kif18A kinesin-8s models 163

Figure 4.10 Structural and sequence alignment of the loop 8 and loop 2 region of representative members of the motile, non-motile depolymerase and motile depolymerase kinesins 164

List of Tables

Table 2.1. Prominent interactions involving the high-affinity state of dynein's MTBD. 83

Table 2.2 Prominent interactions involving the low-affinity state of dynein's MTBD. 84

Table 2.3. *S. cerevisiae* strains used in this study. 85

Table 3.1. ATPase activity of Dynein's MTBD mutants 108

Table 3.2 Stepping rate constants of WT and high-affinity MTBD mutants 114

Table 3.3. *S. cerevisiae* strains used in this study 124

Table 4.1. Summary of collected Cryo-EM data . 167

Abbreviations

ATP Adenosine Triphosphate

EM Electron Microscopy

GDP Guanosine Diphosphate

GMPCPP α,β-Methyleneguanosine 5′-diphosphate

GTP Guanosine Triphosphate

MD Molecular Dynamics

MDFF Molecular Dynamics Flexible Fitting

MT. Microtubule

MTBD. Dynein's Microtubule Binding Domain

SRS. Seryl-tRNA synthetase

Acknowledgements

The last six years have been full of great experiences, lots of learning, friendship, support, and both personal and academic growth. I never imagined the great joy that I am experiencing today, I am really grateful for that.

First, I want to thank Andres Leschziner. Finding a great advisor and a good thesis project are not easy tasks. I must give special recognition to Adam Cohen for the advice of reaching out to Andres at the time when I was not sure about what I wanted to do for my PhD research. Andres's guidance and mentorship have been key for my accomplishments and growth as a scientist. He has been very supportive and has given me the freedom to follow my multiple interests and to develop my ideas and projects, both scientific and non-scientific. Among the many things I learned from Andres, I would like to highlight the importance of achieving a great balance between working hard and enjoying life. I feel very lucky for all the projects, outcomes and experiences that resulted from this recipe.

I would like to thank Sam Reck-Peterson. I have had a great time collaborating with and working in her lab. I always felt that I had a second advisor and a second lab, which gave me double of benefits and support and for which I am very grateful. I want to thank Jim Hogle and Xiaowei Zhuang, members of my advising committee, for always being available despite their busy schedules and for their suggestions and support to my work. Outside of my committee I would like to thank Vince Ramey, Rachel Gaudet, Marcos Sotomayor, Chuck Sindelar, Mike Strauss, Elizabeth Villa, Gabe Lander and Alán Aspuru-Guzik, whitout their mentorship,advice and support my work at Harvard would not have been the same.

My time in the Leschziner Lab has been awesome. I feel really fortunate to have shared time and space with a very supportive and fun group of colleagues, many of which have become very good friends. My interactions with each one, past and current members, are unique and many deserve special recognition. I would like to thank Bret Redwine for his patience and support, specially at the beginning of my PhD when I was shy and insecure. Bret was a wonderful collaborator and he is someone who I always enjoy discussing science and other matters, specially when they are related to my family´s traditions, my life in Oaxaca and American culture. I appreciate the numerous interesting conversations with John Srouji and all his support and teaching while I worked in the lab. I admire John's passion and obsession when it comes to seek an answer to a problem. I want to thank Kat Toropova for being such an awesome office mate and friend, for getting me started on cryo-EM and for expanding my vocabulary with weird English words from overseas. I want to thank Vu Nguyen, Vu has become a very close friend and I hope we reunite again in the future. He has been really supportive and caring, specially at times when I was stressed out. I miss our movie outings and gossiping at night in the lab. Finally, I want to thank Mike Cianfrocco, I like exchanging thoughts with him and I appreciate his rigorous opinions on how science should be conducted and the problems we should try to fix in academia. Thanks to all the other members of the Leschziner, Reck-Peterson and Structural Biology Super groups for making it fun to come to work and for their support all these years. I would like to specially thank Liza Sholl for always dropping what she was doing when I needed help.

I want to thank Hugo Arellano Santoyo, Ema Stokasimov and David Pellman. The last year has been a great ride working with them. I am excited to see what we discover together.

Outside the lab, my student life at Harvard would not have been the same without the support of many people, specially those at the Bok Center and from the English Language Program. I want to thank Pamela Pollock, for her instruction and tutoring at the time when I needed them the most. I want to thank Virginia Maurer from her enthusiasm and support and Sarah Jessop and Marlon Kuzmick for the awesome "Theater of the classroom" class they put together. I had a lot of fun in all these courses. I would like to thank the Fundación México en Harvard and CONACYT for their financial support during the first years of my PhD.

I would like to specially thank my "chosen family". I am fortunate to have in my life many friends, in Mexico, in Cambridge , and other places in the US and abroad. I have met wonderful people during all these years and I have always felt their support and love. Living far from Mexico seemed difficult at the beginning but having you close has made me feel at home and protected all these years. Thanks for all the parties, dances, conversations, trips and meals we have shared together, I look forward to many more times like these. I should specially thank members of the "Mexican Mafia" in Boston, in particular, those who participate in "Clubes de Ciencia México". I am really honored to be part of such generation and a member of this team that promises a change to science education in Mexico. I have learned so much the past year and I look forward to see where we can take this initiative together.

Last but not least, I don't have words to thank enough my family, my parents, Yolanda and Francisco, my siblings, Jorge and Angelica, and my beloved grand ma Adelaida. You have always been a source of inspiration, love, and my biggest supporters in everything I do. I miss you so much but I think what we have accomplished together is worth the distance. ¡Muchas gracias por todo su cariño! ¡Los quiero mucho!

Chapter 1

Introduction

.

The molecular mechanism of molecular motors have been the subject of active research in many scientific fields for over 50 years. This thesis describes my studies on the microtubule-based motors cytoplasmic dynein and kinesin-8 (Figure 1.1).

In this chapter I provide an overview of cytoskeletal motors and the structure of the polymers they use as tracks, the microtubules. Then, I briefly describe the background of cytoplasmic dynein and kinesin-8 that motivated our studies. Finally, I outline the structural approaches we have taken to address the specific questions described at the end of this chapter.

Overview of cytoskeletal motors and their function in cells

The precise delivery and organization of intracellular factors in space and time allow the cell to orchestrate essential tasks. For example, neuronal function involves the transport of signaling molecules along the extended cell body and cell division requires proper segregation of the genetic material. To perform these functions the cell relies on a set of molecules that associate with, translocate along and regulate the dynamics of cytoskeletal filaments using the energy from ATP hydrolysis. These cytoskeletal motors are indispensable for intracellular transport, chromosome segregation and more broadly cell-cell communication and cell polarization (*1*). Highlighting the physiological importance of motors, defects in their functions are associated with neuronal development abnormalities, neurodegenerative and primary cilia disorders, metabolic diseases and several types of cancer (*2*).

Three families of cytoskeletal motors--dyneins, kinesins and myosins --exist in eukaryotes. The baker's yeast, *S. cerevisiae*, uses six kinesins, five myosins, and one dynein. In mammals

genes encoding more than 45 kinesins, 40 myosins and over a dozen dyneins have been identified, and their products may have distinct specialized functions (*1*, *3*).

Myosins organize and move along actin filaments. The first myosin, now classified as a myosin class II, was originally isolated in complex with actin from muscle by Kuhne (*4*) and later shown to have motor activity during muscle contraction. Other myosins, are involved in cell division, membrane trafficking and the proper function of the inner ear (*3*). Their structure and function have been reviewed in (*5*, *6*).

Research designed to test the hypothesis that myosin was responsible for intracellular axonal transport led to the discovery of kinesin (conventional kinesin) (*7*). Surprisingly, the first crystal structure of a kinesin motor domain (*8*) revealed that, despite moving along different tracks, kinesin and myosin harbor similar structural elements at the ATP and track-binding sites. Indeed, years of research have shown that myosin and kinesin have similarities in their core mechanisms (*9*, *10*). They are related to G proteins, a family of GTPases that act as molecular switches inside cells.

In contrast, Dyneins are members of the AAA+ family of ATPases. It was originally identified as an ATPase in cilia (*11*). These axonemal dyneins which also function in flagella are monomeric and do not move along microtubules. Another type of dynein, known as cytoplasmic dynein, was later isolated from brain tissue as a homodimer (*12*) and shown to drive intracellular transport towards the opposite direction to kinesin along the microtubule.

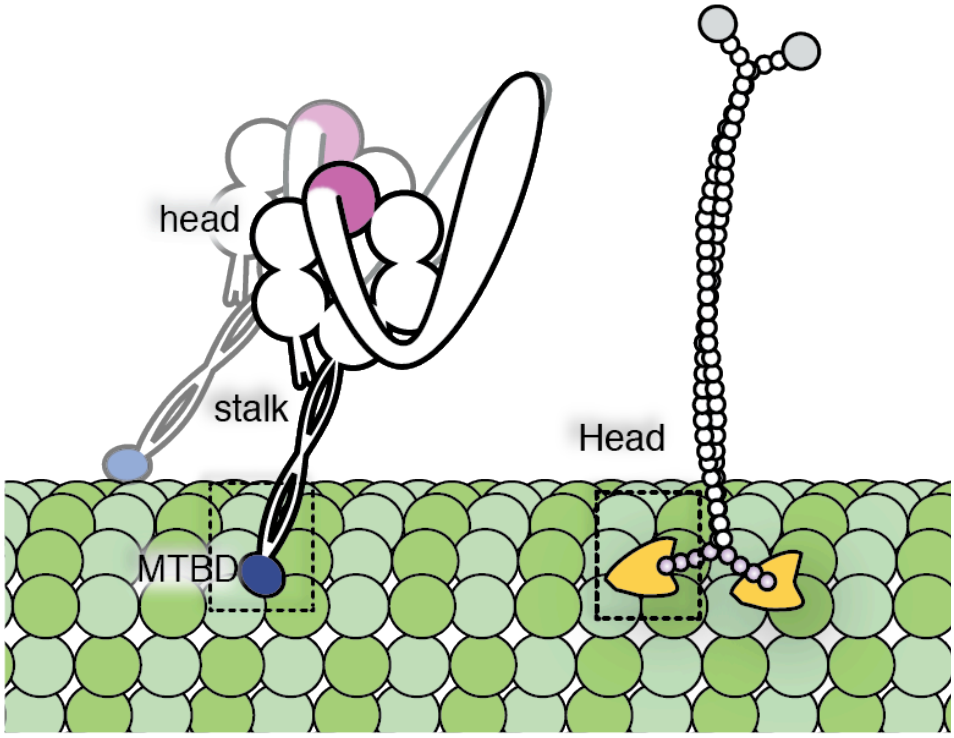


Figure 1.1 Schematic views of cytoplasmic dynein and kinesin-8.

Dynein is a processive minus-end directed motor. How the main site of ATP hydrolysis (depicted in purple) communicates with the MTBD (shown in blue) is not fully understood. Unlike other kinesins, Kip3, the budding yeast Kinesin-8, is a plus-end directed processive motor capable of dwelling at the microtubule (MT) plus-end and it is a MT depolymerase. How Kip3 performs both functions remains unresolved. The conserved kinesin's motor domain is shown in yellow. The microtubule is show in green. Microtubules are cylindrical assemblies of α-tubulin (light green) and β-tubulin (dark green) dimers.

Microtubules - structure and dynamics

Microtubules (MTs) are present in all eukaryotic cells and are important for a wide range of cellular activities, such as cell motility, intracellular transport and cell division (*13*). The structure of microtubules is conserved in all eukaryotes (*14*). They form *via* head-to-tail and lateral association of α β-tubulin heterodimers resulting in a cylindrical arrangement of ~25 nm in diameter. The longitudinal interactions of tubulin dimers form polar structures know as protofilaments. Most microtubules in cells are formed by 13 protofilaments. There are, however, various naturally occurring microtubules made up of 11-15 protofilaments (*15*). The lateral association of protofilaments occurs along a helical arrangement of monomeric tubulin units. In the 13-protofilament MT, the lateral interactions among tubulin monomers are mostly homotypic (α-α and β-β) except at one location, known as the "seam", where two protofilaments contact each other through heterotypic (α-β) interactions.

The microtubule exhibits polarity--its two opposite ends are dynamically and chemically distinct. MT growth and disassembly occur *via* association and dissociation of tubulin dimers at the "plus-end", where ß-tubulin subunits are exposed. The "minus-end," which contains exposed α-tubulin subunits, is "capped" by the **γ**-TURC complex, which may prevent MT growth from this end. In the cell, minus-ends are often located near the nucleus where they can attach to the microtubule organizing centers and centrioles. In contrast, the plus ends are found near the cell periphery and undergo phases of rapid growth and shrinkage, a behavior known as dynamic instability (*16*).

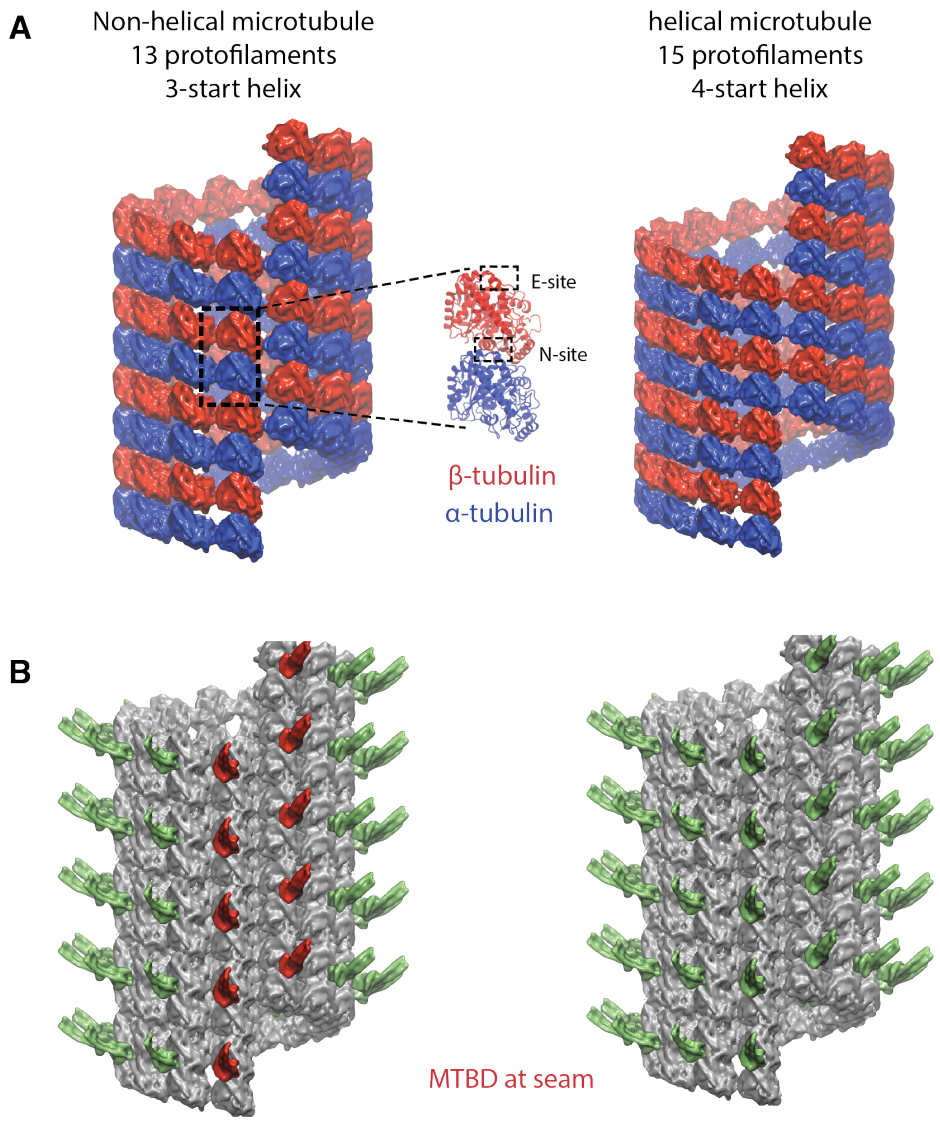


Figure 1.2 Schematic view of helical and non-helical microtubules

(A) Synthetic maps at 8 Å resolution of 13 and 15 protofilament (PF) microtubules. Microtubules form by the head to tail and lateral association of α (blue) and β-tubulin (red) dimers. *In vivo*, the most abundant MT are 13 PF microtubules. MT assembly and disassembly is controlled by the GTP state of tubulin. There are two GTP binding sites in tubulin. The binding site in α -tubulin is known as the N-site whereas the one in β-tubulin is called the E-site. **(B)** Proteins like dynein and kinesin bind at the αβ-tubulin interface. In a 13 PF microtubule the motor density along the microtubule will present a discontinuity at a location know as "the seam". In contrast, in helical microtubules, the motor density also follows a helical path.

GTP binding and hydrolysis by the tubulin units regulate MT dynamic instability. Tubulin contains two GTP binding sites. α-tubulin does not exchange nor hydrolyze GTP, which is stably bound to a site near the intradimer interface (Figure 1.2), known as the "N-site" or non-exchangeable site. The GTP-binding site in β-tubulin is called the "E-site" or exchangeable-site where GTP is frequently exchanged and hydrolyzed. Tubulin dimers can polymerize into microtubules only when GTP is bound at the E-site. It is also worth noting that GTP-hydrolysis does not happen in the unassembled tubulin but instead once tubulin is assembled into the MT-lattice. For a long time it was speculated that the tubulin conformation changes depending on the identity of the nucleotide bound to the E-site. However, structural studies (*17*) have shown that the two extreme conformations, "straight", observed in the MT-lattice, and "curved", present in the isolated αβ-tubulin, are consistent with a model where the conformational changes are due to the incorporation of tubulin into the MT-lattice. The contribution of αβ-tubulin curvature to MT dynamics has been reviewed recently (*18*).

Dynamic instability of MTs may be explained by the "GTP cap model". Incorporation of new tubulin subunits to the MT plus-end of a growing MT stimulates GTP hydrolysis at the E-site. While the MT-lattice is composed of GDP-bound β-tubulin, the MT plus-end contains GTP-bound β-tubulin. This stable "GTP cap" inhibits MT-disassembly and promotes addition of tubulin subunits whereas the relatively unstable GDP-tubulin lattice favors depolymerization, a transition called catastrophe. Recovering the cap enables MT rescue--switching to a growth phase. Dynamic stability allows MTs to rapidly explore space and control their organization and stability. This could could provide cues to the cell to rapidly reorganize the cytoskeleton when

necessary (*16*). For example, during mitosis, MTs reorganize to form the spindle and their stability is regulated to allow chromosome binding, alignment and segregation.

Dynamic instability is regulated by MT-associated proteins, or MAPs, kinesins. These factors can bind to the MT-lattice or the MT-end, modulating their growth or shrinkage. Tubulin binding ligands such as taxol, colchicine, vinblastine and nocodaxole can also affect MT dynamics.

Dynein - structure and function

Dyneins (Reviewed in (*19*)) constitute a family of cytoskeletal molecular motors with specialized functions in intracellular transport, ciliary beating and organization of the mitotic spindle. They can be divided into two major groups: axonemal dyneins, which are responsible for the movement of cilia and flagella and cytoplasmic dyneins, which are involved in cellular transport, chromosome segregation and cell division (*1*).

The dynein holoenzyme is a homodimer of 0.5 megadalton (MDa) chains. Each chain contains (Figure 1.1) an N-terminal region, known as the "tail", involved in dimerization and harboring binding sites for cargo and accessory proteins. The segment following the tail, and the first region of the motor domain, is known as the "linker" and is the force-generating element. Following the linker, there are six concatenated AAA+ domains (AAA1-6) (*20*, *21*) arranged as a ring called the "head". ATP hydrolysis by AAA1 is essential for dynein's function (*22*). Dynein binds MTs via a globular MT binding domain (MTBD) located at the end of a 15 nm long antiparallel coiled-coil that extends from AAA4. This region is termed the "stalk" (*20*, *21*).

Binding and release from MTs, which underlie dynein's ability to walk along its track, is coupled to ATP hydrolysis. Intriguingly, the main site of ATP hydrolysis (AAA1) is separated

from the MTBD by over 25 nm. This remarkable long-range communication is unique to dynein as in myosin and kinesin, the track-binding sites are found within the motor domain.

How do the head and MTBD communicate with each other? What are the changes responsible for modulating the affinity between the motor and its track during a dynein's step? The current model explaining this long-range communication, known as the "helix-sliding model", proposes that ATP hydrolysis in the motor leads to conformational changes in the "stalk", a long coiled-coil that connects the dynein's motor domain and the MTBD, thus modulating dynein's affinity for the MT. Support for this model comes from biochemical data (*23*, *24*) and structural studies including the crystal structure of the MTBD (*25*) and those of the dynein motor domain in the ADP and ATP-like states (*26*, *27*). In summary, helix-sliding within the coiled-coil stalk allows dynein to alternate between two states: (1) a high ATPase activity, low microtubule binding affinity state and (2) a slow ATPase activity, tight microtubule binding affinity state (*24*). Other more complex variations of this model that include three registries have also been proposed (*24*). Consistent with the helix-sliding model, different coiled-coil registers resulted in different affinities (*23*). Gibbons and colleagues (*23*) created small constructs that fixed the register of the coiled-coil region adjacent to the MTBD by fusing it to a seryl-tRNA synthetase (SRS), a protein that has a natural antiparallel coiled-coil and could thus serve as a platform. These results were confirmed by Kon and colleagues (*24*), who fixed the coiled-coil register directly in a full dynein monomer by engineering disulfide bridges in the stalk. Furthermore, Kon et al. showed that the register fixed by the formation of a disulfide bond depended on the nucleotide state of the dynein head. The crystal structures of the dynein motor domain bound to ADP by Kon and collegues (*26*), and bound to ADP-Vanadate (ADP-Vi) by

Schmidt et al. (*27*), offered a molecular explanation for how helix sliding is initiated and propagates through the coiled-coil stalk. ATP binding to dynein's AAA1 triggers movement of the linker (*28*, *29*), and reduces the affinity of the MTBD for microtubules. In the dynein ADP-Vi structure, where the MTBD adopts the same conformation observed in the low-affinity SRS-MTBD construct (*23*, *25*), the base of the stalk has a different conformation from the one observed in the dynein ADP structure (Figure 1.3). The element responsible for initiating helix sliding (CC2 relative to CC1) has been proposed to be the buttress, another coiled-coil helix that extends from AAA5 and contacts the stalk (*20*, *21*). The stalk and buttress emerge from AAA4 and AAA5 respectively. Their relative movement is coupled to rearrangements in the AAA ring. Thus, this long range communication between the head and MTBD may occurs as follows: upon ATP binding, closure of the AAA1 site is coupled with rearrangements of the AAA domains that include the rotation of the AAA5, effectively "pulling" the buttress and CC2 relative to CC1, thereby initiating sliding within the stalk (Figure 1.3). The molecular basis for how dynein's MTBD recognizes the MT and communicates MT-binding to the head will be presented in Chapter 2.

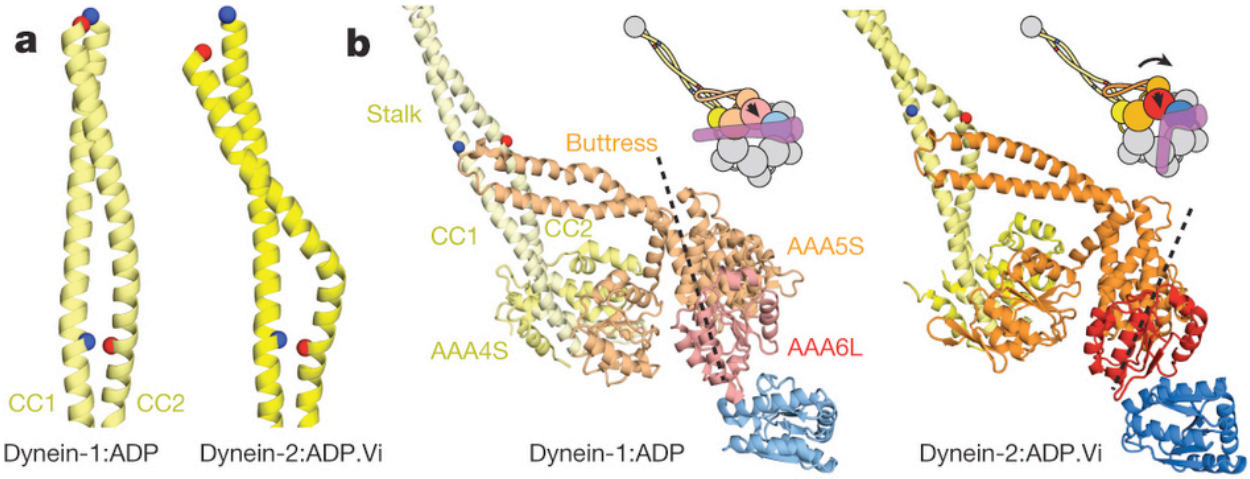


Figure 1.3 Buttress movement initiates helix sliding in dynein's stalk
(A) Ribbon representation of the dynein coiled-coil stalk (shown in yellow). In dynein-2:ADP.Vi (*27*) the stalk CC2 is kinked. Compared with the dynein-1:ADP stalk (*26*), CC2 is displaced by one turn of α-helix relative to CC1. Blue and red spheres represent equivalent amino-acid residues in the two structures. **(B)**ATP binding at AAA1 (blue) triggers linker movement (purple domain) and a rotation of the AAA domains. This rotation causes the buttress to "pull" on CC2 initiating helix sliding. Taken from (*27*)

The mechanism behind dynein's stepping

An important question remains: How does this mode of head-to-MTBD communication explain cytoplasmic dynein's motility on the MT? In other well characterized cytoskeletal motors such as Kinesin-1 and myosin-V, intermolecular tension between the two motor domains results in their alternating positions (*30*, *31*). This phenomenon underlies the discrete and uniform "steps" that these motors take along their tracks. In contrast, the mechanistic basis of dynein's stepping behavior, which is remarkably variable, as described below, is unknown. This flexible stepping behavior may allow dynein to navigate obstacles on MTs in a crowded cytoplasm (*32*) or to respond to high-load activities such as nucleokinesis.

Dynein's average step size measured by optical traps is a matter of debate. Mallik and colleagues first reported that mammalian cytoplasmic dynein takes long steps (24-32 nm) under no load (no external force), but decreases its step size to 8 nm under load. This is in marked contrast to a report by Toba *et al.* (*33*) showing that brain-purified dynein takes 8 nm steps independently of load. Gennerich *et al*. (*34*) found that under no load, yeast cytoplasmic dynein takes 8 nm steps but also larger steps (24-32 nm) as well as backwards steps. The authors of this study also found that increasing load induces dynein to take large (12-24 nm) alternating forward and backward displacements that do not produce a net movement. Recently, Nicholas and colleagues (*35*) argued that the observed differences in dynein's stepping behavior under load may be due to intrinsic functional differences between yeast and mammalian dyneins. The authors of this study reported that a mammalian-specific C-terminal sequence, located near AAA1, serves as a regulator of dynein's force production and processivity that could account for

the observed interspecies differences. It remains to be seen what else governs these differences in behavior and how they correlate with specific dynein functions.

While measuring dynein's step size under load remains a challenging pursuit, the stepping behavior of freely moving dyneins has been analyzed in great detail using one-color and two color fluorescence microscopy (*32*, *36*, *37*).

Dynein's stepping is stochastic when its two motors are close --the heads do not alternate-- and becomes coordinated, with the two heads alternating steps, when its two motors are far apart (*32*, *37*). Whether this behavior is due to the catalytic activity of the motor domains or is regulated by the MTBD remains unknown. Thus, the interaction of dynein with the MT and how this interaction is regulated is key to understand dynein's stepping mechanism as it may be one way in which dynein switches between stochastic and coordinated stepping.

Kinesin-8 : Overview and functions

Three distinct activities have been found among different members of the kinesin super-family: MT-based motility, MT-end dynamics regulation and MT-crosslinking and sliding activity. These activities may give rise to the unique functions of kinesins that classify them into at least fifteen subfamilies (*38*). Members of the kinesin-1, kinesin-2 and kinesin-3 families are known for their plus-end directed motility, which is important for the movement of cargo in neurons, cilia and flagella. Members of the kinesin-13 family are best known for their MT-end depolymerization activity that plays a crucial role in regulating MT-length. Members of the kinesin-5 family play a major role in spindle elongation during mitosis due to its MT-sliding activity. Other kinesins, for example kinesin-4, can move towards the plus-end and inhibit both MT polymerization as well as depolymerization (*39*).

Remarkably, kinesin-8s are the only motors known capable of performing all three activities. Kinesin-8s have a conserved role in regulating microtubule length (*40*). Cells lacking kinesin-8 have the common phenotype of abnormally long microtubules. Kinesin-8s are also involved in spindle positioning, kinetochore clustering and spindle elongation (*41*).

While experiments on Kip3, the budding yeast kinesin-8, have shown that a passive MT-binding site in Kip3's sequence, know as the "tail", is responsible for MT cross-linking and sliding (*42*), the elements responsible for processive motility and regulation of MT-end dynamics remain poorly understood. This is part may be due to the apparent distinct activity of members of the kinesin-8 family at MT-ends. Kip3 can depolymerize microtubules stabilized by GMPCPP, which are thought to mimic the "GTP cap" in a Kip3 dosage dependent manner (*43*, *44*). It is also a catastrophe factor on dynamic microtubules (*45*) and it is able to dwell for a long time at MT plus-ends. In contrast, the activity of others kinesin-8s at MT plus-ends remains controversial. Mayr et al (*46*) reported that Kif18a, the human kinesin-8, can depolymerize GMPCPP-MTs whereas other studies have not detected this activity. Instead these studies found that kif18a destabilized MTs by slowing microtubule growth (*47*). Whether Kip3 has acquired the unique activity of depolymerization or these apparently different functions are the result of differences in a common mode of interacting with MT plus-ends is not yet understood.

A important question remains: What are the elements responsible for kinesin-8 processive motility and MT-end dynamics regulation? Alignment of kinesin-8 sequences suggested the neck sequence as a distinctive feature of this family. Experiments with a Kip3 construct where the neck was replaced with a leucine zipper, to maintain the dimerization, shown that Kip3 is motile but the depolymerization activity is impaired (*42*). However, the depolymerization activity was

restored by adding 3 Glycines to the beginning of the Leucine zipper (Arellano-Santoyo personal communication) indicating that a flexible neck linker is necessary but not responsible for the activity. Intriguingly, the kinesin motor domain sequence is highly conserved across families. X-ray crystallography revealed that Kif18A preserves the typical kinesin structure (*48*). A low resolution cryo-EM study suggests that in addition to the conserved MT binding surface, an extended loop 2 (L2) in kinesin-8 makes a contact with alpha-tubulin (*49*). This study proposed that the additional interaction is responsible for both, increasing kinesin-8 processivity and favoring a bent conformation of the terminal tubulin at the plus-end (*49*). The role of loop2 in depolymerization is appealing given that a similar extended L2 is also found in members of the kinesin-13 family of non-motile depolymerases. Mutating the family conserved KVD sequence in L2 reduces kinesin-13 depolymerizing activity (*50*, *51*). However, unlike kinesin-13s, the most potent MT-depolymerases so far identified, kinesin-8s are weak depolymerases and do not have the KVD sequence. Thus, it is not clear how differences between the L2 sequences of kinesin-8s and kinesin-13s could explain such differences in activity. Moreover while kinesin-13s are non-motile, kinesin-8s are highly processive motors (*43*, *52*). Therefore, the role of L2 in kinesin-8s processivity or MT-end regulation activity remains untested.

Structural biology of microtubule-based motors and microtubule-associated proteins

Understanding the mechanism by which molecular motors and other microtubule associated proteins (MAPS) perform their function requires structural knowledge of their interaction with MTs.

These complexes, however, pose major challenges to classical structural approaches such as X-ray crystallography and Nuclear Magnetic Resonance (NMR). First, MTs are large polymers that do not easily crystallize nor isotropically tumble to enable NMR studies in solution. Secondly, the motors can be very large (e. g. dynein) and their oligomeric states and compositions can be quite complex. They are typically dimeric but trimeric or tetrameric forms have been observed. Furthermore, they can also associate with other factors and function as a multisubunit complexes. Finally, it is challenging to purify endogenous motors, both in terms of yield and purity. This may be surmounted thanks to recent developments of recombinant systems. These challenges make cryo-electron microscopy (cryo-EM) uniquely suited to study motors and MAPS bound to MTs. Specifically 3D structures of motors bound to the MT have yielded important functional insights into their mechanisms.

I will divide this section into two parts. First, I introduce the general strategy used to prepare samples containing motors bound to MTs. Then, I outline major features of the image-processing methodologies used for three-dimensional reconstructions. I focus this discussion on work done over the last 10 years, when single particle approaches have been implemented to study these large macromolecular complexes.

Electron microscopy: Sample preparation

Reconstruction of high resolution 3D-EM structures of MAP-MT complexes may be achieved by the procedure schematically shown in figure 1.4. In addition, the MT structure, *in vivo* and *in vitro*, has been studied by a variety of other methods, including thin sectioning of fixed and embedded material, stained in various ways, by negative staining of isolated filaments

and by freeze fracturing (*14*). Each of these techniques has made valuable contributions to our knowledge of the MT structure and the proteins that associate with it.

Typically, the macromolecule under study is applied to small (3 mm in diameter) copper grids coated with a thin layer of carbon that acts as a support. At this point, the samples can be either flash-frozen by plunging them into liquid ethane kept at liquid nitrogen temperature, know as "cryo-EM", or the aqueous buffer can be replaced with a solution of a heavy metal salt, such as uranyl acetate or formate, after which the sample is air-dried. This method is known as "negative stain".

Negatively stained samples are frequently used at the early stages of a project to get initial low-resolution models (~30 Å) of the specimen of interest. A main drawback of this type of sample is that fine structural details that are not accessible to the stain are not visible. To get high-resolution information, cryo-EM samples are needed. In cryo-EM, the sample can be kept in the same buffer as used in biochemical assays, making this technique arguably the most powerful to study macromolecules "trapped" in their "native" state or states. Unfortunately, the contrast of cryo-EM images is very low due to the low difference in density between the macromolecule and the buffer solution. Thus, large large data sets and more intensive data processing are required to reveal high resolution information.

After sample preparation, either cryo-EM or negative stain, the sample is exposed to a high-energy electron beam (120 - 400 kV) where electrons scattered by the sample form images that are projections of the macromolecule along the electron beam path. These electrons are collected in a charge coupled-device (CCD) camera, photographic film or electron direct detectors to obtain the final images. In other words, EM images contain information about the

local density of the molecule along the direction of the electron beam. The challenge of image processing in EM is to determine the relationship between individual projections in order to reconstruct the three-dimensional structure.

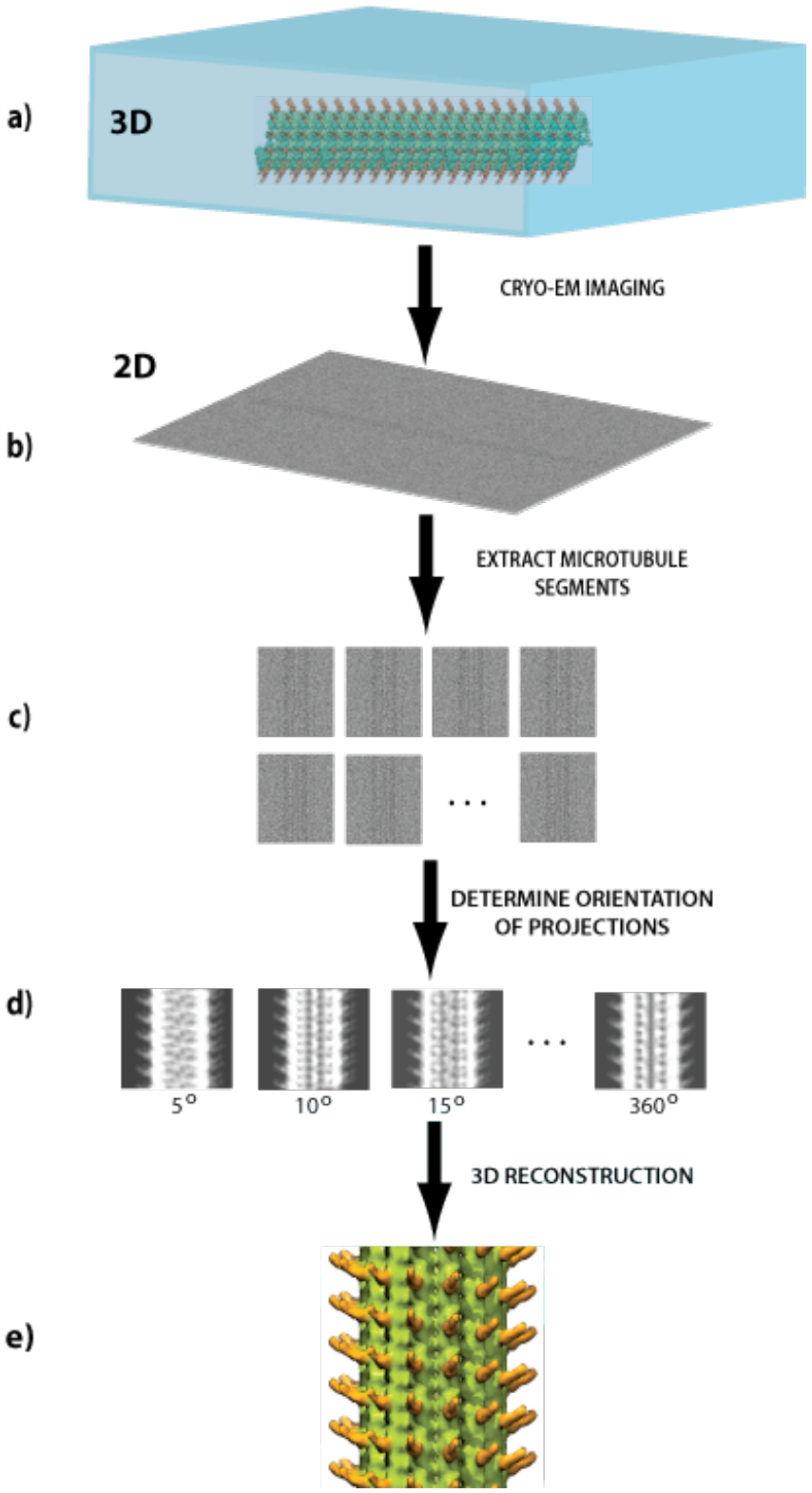


Figure 1.4 Three-dimensional reconstruction of proteins bound to microtubules from electron microscopy images of frozen hydrated samples

Figure 1.4. Three-dimensional reconstruction of proteins bound to microtubules from electron microscopy images of frozen hydrated samples (Continued)

The process of 3D reconstruction from EM images can be divided into three steps: (1) Data collection, (2) Two dimensional image processing, and (3) Three-dimensional reconstruction. **a)** A cryo-EM sample of the MT-binding protein bound to microtubules is imaged in the electron microscope and **b)** micrographs are recorded. **c)** Short segments along the microtubule are extracted from the micrographs and they are analyzed using statistical methods to find their corresponding orientations. This is done by aligning the segments against a set of references **d)**. These references are projections along known orientations (angles are shown under the projections) of a reference model (the contrast in the images in **d)** was inverted for clarity of the figure). **e)** In the final step a 3D structured is obtained combining the images in their appropriate orientations.

Methods for three-dimensional reconstruction of proteins bound to microtubules

Helical diffraction theory

For a long time, reconstructions of motors bound to MTs were achieved at resolutions lower than 30 Å. This was in part due to the image-processing algorithms used for analysis. In contrast to traditional single-particle approaches, image processing involved the careful analysis of the diffraction patterns made by MTs containing 15 protofilaments, which are perfectly helical (Figure 1.2). The theory behind this analysis, know as helical diffraction theory, resembles traditional X-ray diffraction. It is worth mentioning that the idea of using EM images for 3D reconstruction of structures started by studying helices (*53*). More details on this elegant theory can be found in the following references (*53*-*58*).

EM studies of helices have taken advantage from a consequence of the helical symmetry. A single image of a helix contains multiple views of the most basic repeating unit in a helix. This type of data is routinely collected in tomography by tilting the microscope stage to obtain multiple projections of a specimen. Conveniently, in a helix, these tilted views are provided by the rise and rotation that describe the helical structure (Figure 1.4). To make use of these different views one must first determine the helical symmetry of the molecule and then, use helical diffraction theory to reconstruct the 3-D structure.

The diffraction pattern of a helix exhibit characteristic "layer lines," (*56*)which are important in structural studies of microtubules. A helix can be thought of as a 2D lattice folded into a cylinder with the condition that at least two points of the 2D lattice overlap in the cylinder (Figure 1.5). Thus, the relationship between a helical lattice and a 2D lattice may be explained through Fourier transforms (FT). The diffraction pattern of a 2D lattice in real space is also a 2D

lattice in reciprocal space. Therefore, it is not surprising to expect diffractions at particular locations in the Fourier transform of a helix. To understand the FT of a helical lattice, lets consider the near and far sides of a helix separately (the near side is the one facing the observer). The central part of the near side looks almost like a vertical strip of a 2D lattice. As we move away from the center, there is a progressive compression of the 2D lattice points caused by the curvature. Thus, in Fourier space this results in an expansion along the same axis. The separation along the perpendicular axis remains unchanged, thus changes along this direction are not expected. The resulting diffraction pattern, rather than showing spots arranged in a 2D lattice, contains streaks. The streaks are caused by the horizontal compression. Understanding the FT for the near side of the helix allows us to predict the one for the far side, which looks essentially like the near side but is rotated 180° about the long axis of the helical helix. Therefore, its FT should look the same as the near side but is flipped about the vertical axis. The 2D diffraction pattern of a projection of a helix thus results from adding the FTs of the near and far sides. The horizontal streaks are the so called “layer lines” in the diffraction pattern of a helix. Separating the helical lattice into a near and far side makes it easier to understand why the diffraction spots have a vertical mirror axis of symmetry.

The diffraction pattern of a MT shows a characteristic layer line at 1/4 $Å^{-1}$, corresponding to the tubulin monomer repeat along a protofilament. The presence or absence of layer lines at particular locations gives us useful information about the underlying helical structure. For example dynein and kinesin bind at the intradimer tubulin interface, thus, an image of a microtubule highly decorated by these motors will show an additional layer line at 1/8 $Å^{-1}$. The position of this layer line is due to the separation of motors along a protofilament. Other useful

information that can be inferred from the diffraction patterns includes the rise per unit of a helix, the helix diameter, and the protofilament number in the case of MTs (*59*).

Helices can be analyzed by single particle methods.

For about 40 years, MTs and other helical objects were extensively studied using the helical diffraction theory. This approach assumes a perfect repeated arrangement of a minimal motif, termed asymmetric unit, the helical filament. This assumption allows the parameters that define the underlying helical symmetry to be extracted from its diffraction pattern. However, to study MTs, this theory is limited by the fact that biological helical polymers are seldom perfect and instead exhibit flexibility and/or heterogeneity. Furthermore, MTs are not perfectly helical objects. *In vivo* and *in vitro,* the most common MTs are pseudo-helical objects that contain a seam. Several modifications to the helical diffraction theory have been proposed to deal with the MT seam (*60*, *61*) without major improvements in resolution. In 2000, Egelman developed a method to process images of helices by treating individual helices as if single particles (*62*) . This was a major image processing breakthrough that has enabled high resolution 3D reconstructions of helical polymers (*63*) and proteins bound to MTs.

Egelman's method, officially known as The Iterative Helical Real Space Reconstruction (IHRSR) algorithm (*62*-*64*) works similarly to conventional single-particle methods used for macromolecules that do not adopt higher order structures. It has been shown to overcome many of the problems associated with biological filaments that are flexible and display less order than expected. This method involves alignment of small segments of the helical filament against projections of an initial reference. After a 3D reconstruction is made, a search for the helical

symmetry parameters (rise and rotational angle) is performed in real space. Finally, the symmetry parameters are used to average the multiple copies of the asymmetric unit along the helical structure. The entire process is repeated until convergence is achieved. This method, as originally developed, is only useful for MTs that display true helical symmetry (i.e. that do not contain a seam).

In the case of MTs with a seam (such as 13 and 14PF PF MTs) recent modifications to the IHRSR method have been developed (*65*, *66*). In 2007 Charles (Chuck) Sindelar developed an algorithm to study kinesin bound to 13 PF microtubules (*65*). We adapted his method to reconstruct dynein's MTBD bound to 14 PF microtubules in 2012 (*67*). This new approach mainly differs from the IHRSR method mainly in the symmetrization step, with the averaging now done along a single helix turn rather than the entire MT. In addition, it implements a quality control step to increase the accuracy of the seam position finding by looking at the consistency of alignment parameters of segments extracted from the same filaments. This also constrains the alignment parameters of contiguous boxes extracted from the same filament. This is based on the principle that for a perfectly helical rigid helix, given one segment and its alignment parameters, Euler angles and shifts, one could compute the corresponding angles and shifts for segments extracted from the same filament.

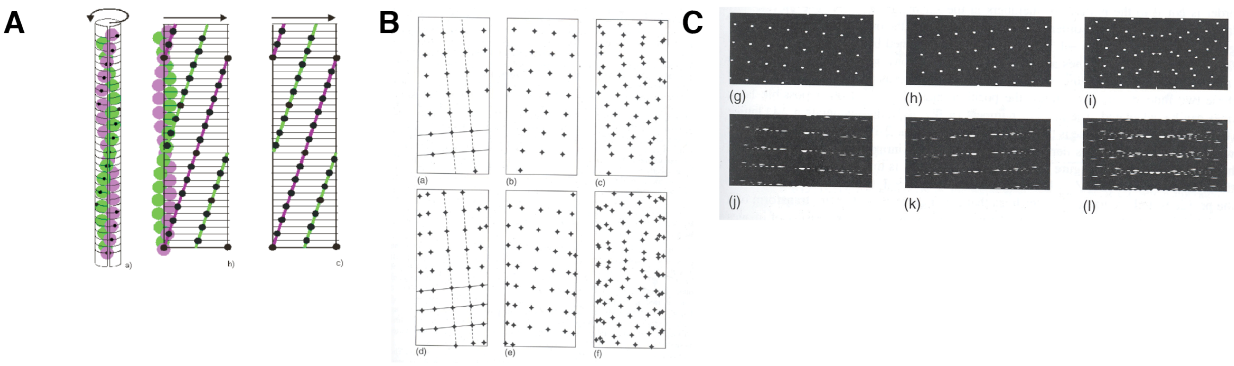


Figure 1.5 Diffraction pattern of a helix

(A) A helix can be thought of as a 2D lattice folded into a cylinder. The relationship between a helical lattice and a 2D lattice may be explained through Fourier transforms (FT). The diffraction pattern of a 2D lattice in real space **(B)** is also a 2D lattice in reciprocal space **(C)**. In **(B)** top row a 2D lattice has been divided mirror along the vertical axis and added to obtain the third panel. At the bottom the same process is shown for the case of a helix. To understand the FT of a helical lattice, lets consider the near and far sides of a helix separately (the near side is the one facing the observer). The central part of the near side looks almost like a vertical strip of a 2D lattice (Compare the top and bottom of B). As we move away from the center, there is a progressive compression of the 2D lattice points caused by the curvature. Thus, in Fourier space (panels in (C)) this results in an expansion along the same axis. The separation along the perpendicular axis remains unchanged, thus changes along this direction are not expected. The resulting diffraction pattern, rather than showing spots arranged in a 2D lattice, contains streaks. The streaks are caused by the horizontal compression. Understanding the FT for the near side of the helix allows us to predict the one for the far side, which looks essentially like the near side but is rotated 180° about the long axis of the helical helix. Therefore, its FT should look the same as the near side but is flipped about the vertical axis (compare left and middle panels in B and C). The 2D diffraction pattern of a projection of a helix thus results from adding the FTs of the near and far sides (right panel in C). The horizontal streaks are the so called “layer lines” in the diffraction pattern of a helix. Separating the helical lattice into a near and far side makes it easier to understand why the diffraction spots have a vertical mirror axis of symmetry. Taken from (*56*)

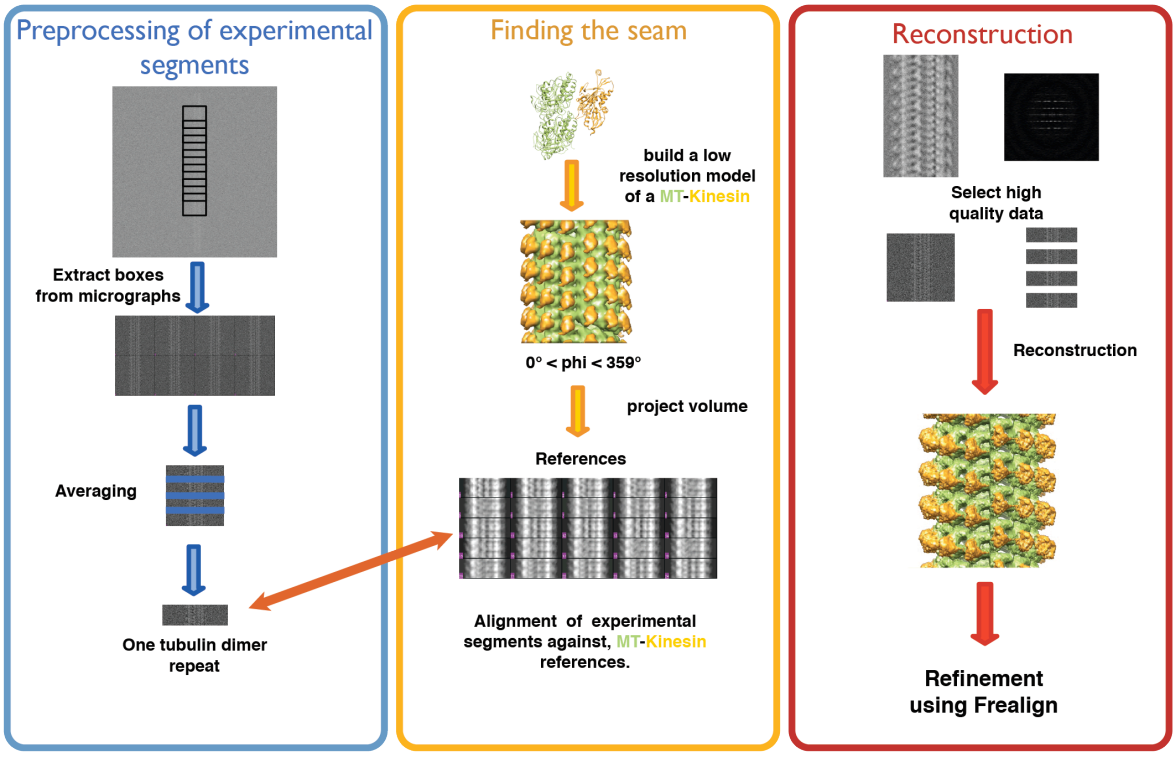


Figure 1.6 Sindelar's method for 3D reconstruction of motors bound to MTs with a seam. Image processing algorithm to obtain 3D reconstructions of motors bound to microtubules with a a seam (*65*). (Left column) Cryo-EM data is collected, microtubules are selected and boxed into overlapping segments of ~ 8-10 tubulin dimers. Each box is subdivided into 80 Å repeats (a tubulin dimer unit) and averaged to increase the contrast. (Middle column) A synthetic low resolution model is created with crystal structures using the canonical microtubule helical parameters (*68*). Multiple projections (axially and out-of-plane) are calculated; Using these as references, the dimer averages are assigned to a location, thus assigning the seam position in each microtubule.The assigned angles are used to create a reconstruction by back projection. This process (alignment and reconstruction) can be repeated to convergence. (Right panel) In the final step, FREALIGN (*69*) is used to correct the CTF and refine the reconstruction to higher resolution. Not shown is a step whereby the protofilaments are averaged and used to create a reconstruction containing 13 (or 14) copies of a single symmetrized protofilament (See figure 1.6 for details on the last step).

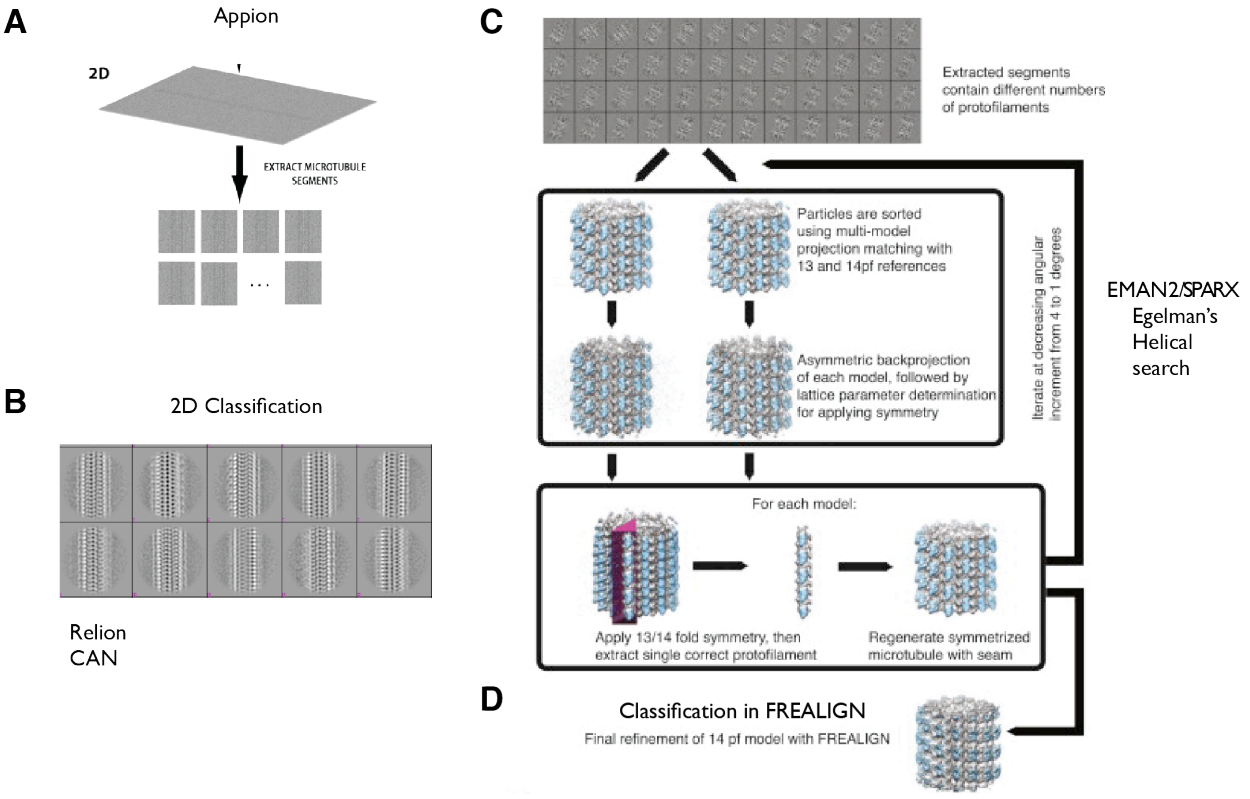


Figure 1.7 Processing pipeline for 3D reconstruction of motors bound to microtubules with a seam. Multi reference alignment, helical search and reconstruction.

Schematic of the pipeline implemented to process images of microtubules decorated with motor proteins. **(A)** Microtubule images are selected and boxed semiautomatically within Appion (*70*) **(B)** then the microtubule protofilament number is determined by classification of MT segments using a reference free, multi statistical analysis (*71*) implemented in CAN (*72*) or RELION (*73*). **(C)** Highly decorated microtubule segments are classified with 13 or 14 protofilament reconstructions by multi-reference projection matching (Adapted from (*66*)). After each round of projection matching, an asymmetric back projection is generated from each group (13 PF and 14 PF) of aligned segments, and the helical parameters (rise and twist) describing the monomeric tubulin lattice are determined using hsearch_lorentz. The symmetry is imposed in real space. In the symmetrized volume, there is only one "good" protofilament that does not have α-and β-tubulin mis-aligned due to be presence of a seam. This single good protofilament is extracted from the microtubule with a wedge-shaped 3D mask, and the same helical parameters are used to generate a new microtubule density that contains a seam. The process is repeated until convergence. A final refinement of the microtubule segment alignment parameters is performed in FREALIGN without further refinement of helical parameters. Adapted from (*66*)

Whit the exception of Ndc80, which binds at every tubulin monomer (*74*, *75*), the structures of several kinesins in different nucleotide states (*65*, *76-78*), doublecortin(*79*), EB1 (*80*) and dynein's MTBD (*67*) bound to seamed MTs were all obtained using Sindelar's method. Briefly, a synthetic model for a MT with a seam, and with all binding sites on the MT occupied by the protein of interest, is used to directly find the seam position in the experimental data. This is done by comparing segments of the highly decorated MT images with projections of the synthetic model. When the Euler angles and shifts for each MT segment are determined, 3D reconstruction and refinement of parameters are carried out.

In despite of reliably producing ~8-10 Å structures, at which resolutions α-helices may be visualized, I believe, this method has some drawbacks. First, the MT helical parameters, such as rise and angle, used in the symmetrization step, are initially assumed to be the canonical MT parameters (*68*) (For a 13 PF MT: rise = 9.346 Å, angle = -27.69°). The rise per unit is updated later by measuring the axial repeat distance in the FT (1/4 or 1/8 Å layer lines) of the images. However, this approach is very sensitive to errors in the calibrated magnification of the images (i.e. pixel size). The use of an incorrect helical symmetry during 3D reconstruction leads to an incorrect model that propagates errors during subsequent cycles of refinement (*81*). This is in marked contrast to the IHRSR method, where at each cycle of refinement the helical parameters are measured in an asymmetric reconstruction. Then, the best parameters are applied and updated until convergence. Second, as originally implemented, this processing scheme requires the knowledge, obtained by other means, of the microtubule protofilament number of each segment. Although one could expect select and discard microtubules based on their dimensions by using a similarity measurement cutoff, such as cross correlation coefficient, in my experience, MTs with

different protofilament number, are often included in the 3D reconstruction. To solve this problem, our group and others have utilized two-dimensional alignment and classification of microtubule segments. Visual inspection of both, the Moiré patterns (*71*, *82*) and the FTs of the classes allowed us to obtain homogeneous MT populations. This method was proposed by Vince Ramey (UC Berkeley) to study the rather heterogeneous binding of the DAM1 (*71*) complex to MTs.

To solve the potential problem of using the canonical MT helical parameters a hybrid method combining Chuck Sindelar's and Egelman's approaches was required. The new method also implements a multi-reference (13, 14, 15 PFs etc) refinement algorithm that includes a search step of helical parameters at each round of refinement. Gabriel Lander and Richard Hall programmed this multi-model refinement strategy using EMAN2/SPARX and IRHRS. This algorithm allowed the improvement of the resolution of the Ndc80 (*75*) structure, and may have been instrumental to obtain the most recent high-resolution (4.7 - 5.5 Å) structures of dynamic MTs and MTs stabilized by taxol or GMPCPP (*66*). To highlight the importance of obtaining the correct helical parameters, the authors of these study found that MTs stabilized by taxol or GMPCPP have an axial repeat of 83 Å rather than the canonical 81 Å repeat.

Future directions in image processing of proteins bound to microtubules

One shortcoming that all the methods outlined above have is that they rely on having all available MT binding sites occupied by the protein of interest. Even though we and others have found experimental conditions to achieve a high degree of occupancy for several proteins, our work on dynein monomers (not shown) suggests that complete occupancy of all microtubule

binding sites is unlikely for large proteins such as dynein dimers or for proteins with weak affinity for the MT. In addition, our work on kinesin-8 (Chapter 4) and *S. cerevisiae* dynein's MTBD (not shown) suggests that even for small monomeric constructs that bind tightly to MTs, there may be multiple binding modes which can not be resolved by current methods. This is due to the fact that the symmetrization step average together all differences in MT-binding, thus limiting the final resolution of heterogenous regions in the protein of interest.

One computational approach to overcome partial occupancy is to implement 3D classification to sort out heterogeneity as an extension of the single-particle approach. Rather than using a helical turn as the repeated structure, a single molecule bound to the microtubule plays that role. A synthetic reference could be generated by docking the protein of interest onto the microtubule. Alternatively, a low resolution model obtained by other methods (e.g. negative stain or tomography) may be used. Several projections can be generated from this model and small segments from images of MTs sparsely decorated with the protein can be aligned to each of these references to find the corresponding orientation. This approach does not require that the protein saturate all possible binding sites. It will build density for the motor using information from the occupied locations and ignore those that are empty. This method would prevent the loss of density that might result from averaging occupied sites and unoccupied. This idea was originally designed to pursue the structure of the dynein motor bound to MTs. Due to the size of dynein's motor domain (the "head"), we expect its density to drive the alignment during image processing; for that reason we proposed to called this method "head hunter". In support of the feasibility of this idea, 2D classes of side views of dynein dimers and the dynein-dynactin

complex bound to MTs have been achieved with great success by Stan Burgess (Leeds) (personal communication) and Chowdhury *et al.* (Scripps) (*83*), respectively.

To address the challenge of conformational flexibility and heterogeneity in proteins bound to MTs, one could use 3D classification methods implemented in softwares such as SPARX (*84*), XMIPP (*85*) or RELION (*73*). In fact, a recent paper describing the implementation of the IHRSR method in SPARX (*86*) already put forward the idea of using resampling techniques to yield information that can be used to identify multiple conformational states in the different units along a helix. In this paper, the authors showed that Codimensional Principal Component Analysis (PCA) can be used to obtain "eigenvolumes" that describe heterogeneity in a helical sample. The method, called helical PCA, was used for the analysis of conformational variability of the myosin-tropomyosin-myosin complex. However, the resolution of the symmetrized reconstruction was ~8 Å, and the variability described was in terms of lower resolution features. It would be interesting to see this methodology applied to a higher resolution structure and to implement this analysis to study pseudo-helices such as MTs.

The use of electron direct detectors has revolutionized the cryo-EM field and presented an excellent opportunity to further improve EM studies of MAP-MT complexes. It is now possible to obtain near-atomic and atomic-resolution structures of MT-bound proteins, allowing de novo tracing of protein backbone and visualization of amino-acid side-chains. Furthermore, the high resolutions will facilitate detailed analyses of the conformational flexibility of these proteins, and the effects of nucleotide. EM has experienced major advances in the past years, both at the hardware (e.g. direct detectors, phase plates, spherical aberration correctors) and software (e.g. Frealign, motion correction, RELION, IHRSR-SPARX) levels. Thanks to these developments,

near-atomic resolution structures of MTs are a reality (*66*, *87*, *88*) (Nogales Lab, personal communication), and structures of large proteins, such as the dynein dimer, bound to MTs are now entirely within reach.

Summary of results presented in this thesis

In this thesis I present our work to uncover how dynein's MTBD may communicate MT-binding to the motor domain and how it regulates its affinity. I also describe our efforts to understand dynein's complex stepping behavior. I conclude with our work to understand the processive motility and depolymerization activity of kinesin-8.

In chapter 2 we describe a sub-nanometer cryo-EM reconstruction of dynein's microtubule binding domain in complex with the microtubule. We found that upon MT binding, dynein's MTBD undergoes a large conformational change underlying changes in its affinity for MTs. Molecular dynamics simulations allowed us to identify negatively charged residues within the MTBD that tune dynein's affinity for MTs. We mutated these residues to alanine and show a dramatic increase in dynein's affinity for microtubules that results in enhanced motor processivity. These high MT-binding affinity mutants provide us with a tool to explore the role of MT-binding affinity in dynein's stepping behavior. In chapter 3, I describe single molecule experiments to study the stepping pattern of dynein. Together, our results provide a model for how dynein has evolved a finely tuned mechanism that allows its MTBD to communicate MT-binding to the motor domain and to regulate its affinity for MTs and motor processivity.

In chapter 3, I present our structural models of Kip3 bound to the MT-lattice and to the end region of microtubules. We describe structures of Kip3's motor domain bound to MTs stabilized

by taxol or GMPCPP. We identified and tested, using fluorescence imaging, single residues important for Kip3's processivity, MT-end dwelling and depolymerization activity. Our results suggest a structural mechanism for how Kip3 has acquired its functional diversity.

References

1. R. Vale, The molecular motor toolbox for intracellular transport. *Cell* **112**, 467–480 (2003).

2. R. B. Vallee, C. Y. Tai, The Role of Dynein in Disease. (2003).

3. J. A. Spudich, S. Sivaramakrishnan, Myosin VI: an innovative motor that challenged the swinging lever arm hypothesis. *Nat Rev Mol Cell Biol* **11**, 128–137 (2010).

4. A. G. Szent-Györgyi, The early history of the biochemistry of muscle contraction. *J. Gen. Physiol.* **123**, 631–641 (2004).

5. L. M. Coluccio, *Myosins* (Springer Science & Business Media, 2007).

6. F. Buss, G. Spudich, J. Kendrick-Jones, Myosin VI: cellular functions and motor properties. *Annu. Rev. Cell Dev. Biol.* **20**, 649–676 (2004).

7. R. D. Vale, How lucky can one be? A perspective from a young scientist at the right place at the right time : Nature Medicine : Nature Publishing Group. *Nature medicine* (2012).

8. F. J. Kull, E. P. Sablin, R. Lau, R. J. Fletterick, R. D. Vale, Crystal structure of the kinesin motor domain reveals a structural similarity to myosin. *Nature* **380**, 550–555 (1996).

9. F. J. Kull, S. A. Endow, Force generation by kinesin and myosin cytoskeletal motor proteins. *J. Cell. Sci.* **126**, 9–19 (2013).

10. R. D. Vale, R. A. Milligan, The way things move: looking under the hood of molecular motor proteins. *Science* **288**, 88–95 (2000).

11. I. R. Gibbons, STUDIES ON THE PROTEIN COMPONENTS OF CILIA FROM TETRAHYMENA PYRIFORMIS. *Proceedings of the National Academy of Sciences of the United States of America* **50**, 1002–1010 (1963).

12. B. M. Paschal, R. B. Vallee, Retrograde transport by the microtubule-associated protein MAP 1C. *Nature* **330**, 181–183 (1987).

13. J. S. Hyams, C. W. Lloyd, *Microtubules* (Wiley-Blackwell, 1994).

14. K. Roberts, J. S. Hyams, *Microtubules* (1979).

15. A. Akhmanova, C. C. Hoogenraad, Microtubule Minus-End-Targeting Proteins. *Curr. Biol.* **25**, R162–R171 (2015).

16. T. Mitchison, M. Kirschner, Dynamic instability of microtubule growth. *Nature* (1984).

17. L. M. Rice, E. A. Montabana, D. A. Agard, The lattice as allosteric effector: Structural studies of αβ- and γ-tubulin clarify the role of GTP in microtubule assembly. *Proceedings of the ...* (2008).

18. G. J. Brouhard, L. M. Rice, The contribution of αβ-tubulin curvature to microtubule dynamics. *The Journal of Cell Biology* **207**, 323–334 (2014).

19. A. J. Roberts, T. Kon, P. J. Knight, K. Sutoh, S. A. Burgess, Functions and mechanics of dynein motor proteins. *Nat Rev Mol Cell Biol* **14**, 713–726 (2013).

20. A. P. Carter, C. Cho, L. Jin, R. D. Vale, Crystal structure of the dynein motor domain. *Science* **331**, 1159–1165 (2011).

21. T. Kon, K. Sutoh, G. Kurisu, X-ray structure of a functional full-length dynein motor domain. *Nat Struct Mol Biol* **18**, 638–642 (2011).

22. S. L. Reck-Peterson, R. D. Vale, Molecular dissection of the roles of nucleotide binding and hydrolysis in dynein's AAA domains in Saccharomyces cerevisiae. *Proceedings of the National Academy of Sciences of the United States of America* **101**, 1491–1495 (2004).

23. I. Gibbons *et al.*, The affinity of the dynein microtubule-binding domain is modulated by the conformation of its coiled-coil stalk. *Journal of Biological Chemistry* **280**, 23960–23965 (2005).

24. T. Kon *et al.*, Helix sliding in the stalk coiled coil of dynein couples ATPase and microtubule binding. *Nat Struct Mol Biol* **16**, 325–333 (2009).

25. A. P. Carter *et al.*, Structure and functional role of dynein's microtubule-binding domain. *Science* **322**, 1691–1695 (2008).

26. T. Kon *et al.*, The 2.8 Å crystal structure of the dynein motor domain. *Nature* (2012), doi:10.1038/nature10955.

27. H. Schmidt, R. Zalyte, L. Urnavicius, A. P. Carter, Structure of human cytoplasmic dynein-2 primed for its power stroke. *Nature* (2014), doi:10.1038/nature14023.

28. A. Roberts *et al.*, AAA+ ring and linker swing mechanism in the dynein motor. *Cell* **136**, 485–495 (2009).

29. T. Kon, T. Mogami, R. Ohkura, M. Nishiura, K. Sutoh, ATP hydrolysis cycle-dependent tail motions in cytoplasmic dynein. *Nature Publishing Group* **12**, 513–519 (2005).

30. A. Yildiz, M. Tomishige, R. D. Vale, P. R. Selvin, Kinesin walks hand-over-hand. *Science* **303**, 676–678 (2004).

31. A. Yildiz, J. N. Forkey, S. A. McKinney, T. Ha, Y. E. Goldman, Myosin V Walks Hand-Over-Hand: Single Fluorophore Imaging with 1.5-nm Localization. *Science* (2003).

32. W. Qiu *et al.*, Dynein achieves processive motion using both stochastic and coordinated stepping. *Nat Struct Mol Biol* **19**, 193–200 (2012).

33. S. Toba, T. M. Watanabe, L. Yamaguchi-Okimoto, Y. Y. Toyoshima, H. Higuchi, Overlapping hand-over-hand mechanism of single molecular motility of cytoplasmic dynein. *Proceedings of the National Academy of Sciences* **103**, 5741–5745 (2006).

34. A. Gennerich, A. P. Carter, S. L. Reck-Peterson, R. D. Vale, Force-induced bidirectional stepping of cytoplasmic dynein. *Cell* **131**, 952–965 (2007).

35. M. P. Nicholas *et al.*, Control of cytoplasmic dynein force production and processivity by its C-terminal domain. *Nature Communications* **6**, 6206 (2015).

36. S. L. Reck-Peterson *et al.*, Single-molecule analysis of dynein processivity and stepping behavior. *Cell* **126**, 335–348 (2006).

37. M. A. DeWitt, A. Y. Chang, P. A. Combs, A. Yildiz, Cytoplasmic Dynein Moves Through Uncoordinated Stepping of the AAA+ Ring Domains. *Science* **335**, 221–225 (2012).

38. N. Hirokawa, Y. Noda, Y. Tanaka, S. Niwa, Kinesin superfamily motor proteins and intracellular transport : Article : Nature Reviews Molecular Cell Biology. *Nature reviews Molecular cell ...* (2009).

39. H. Bringmann, G. Skiniotis, A. Spilker, S. Kandels-Lewis, A Kinesin-like Motor Inhibits Microtubule Dynamic Instability. *Science* (2004).

40. R. Gandhi *et al.*, The Drosophila Kinesin-like Protein KLP67A Is Essential for Mitotic and Male Meiotic Spindle Assembly. *Molecular biology of ...* (2004).

41. X. Su, R. Ohi, D. Pellman, Move in for the kill: motile microtubule regulators. *Trends in cell biology* **22**, 567–575 (2012).

42. X. Su *et al.*, Microtubule-sliding activity of a kinesin-8 promotes spindle assembly and spindle-length control. *Nat Cell Biol* **15**, 948–957 (2013).

43. V. Varga *et al.*, Yeast kinesin-8 depolymerizes microtubules in a length-dependent manner. *Nature Publishing Group* **8**, 957–962 (2006).

44. V. Varga, C. Leduc, V. Bormuth, S. Diez, J. Howard, Kinesin-8 motors act cooperatively to mediate length-dependent microtubule depolymerization. *Cell* **138**, 1174–1183 (2009).

45. M. K. Gardner, M. Zanic, C. Gell, V. Bormuth, J. Howard, Depolymerizing kinesins Kip3 and MCAK shape cellular microtubule architecture by differential control of catastrophe. *Cell* **147**, 1092–1103 (2011).

46. M. I. Mayr, S. Hümmer, J. Bormann, T. Grüner, S. Adio, The Human Kinesin Kif18A Is a Motile Microtubule Depolymerase Essential for Chromosome Congression. *Current Biology* (2007).

47. Y. Du, C. A. English, R. Ohi, The kinesin-8 Kif18A dampens microtubule plus-end dynamics. *Curr. Biol.* **20**, 374–380 (2010).

48. A. Marx, A. Hoenger, E. Mandelkow, Structures of kinesin motor proteins. *Cell Motil. Cytoskeleton* **66**, 958–966 (2009).

49. C. Peters *et al.*, Insight into the molecular mechanism of the multitasking kinesin-8 motor. *EMBO J* **29**, 3437–3447 (2010).

50. T. Ogawa, R. Nitta, Y. Okada, N. Hirokawa, A Common Mechanism for Microtubule Destabilizers—M Type Kinesins Stabilize Curling of the Protofilament Using the Class-Specific Neck and Loops. *Cell* (2004).

51. C. A. Moores, R. A. Milligan, Lucky 13-microtubule depolymerisation by kinesin-13 motors. *J. Cell. Sci.* **119**, 3905–3913 (2006).

52. M. L. Gupta, P. Carvalho, D. M. Roof, D. Pellman, Plus end-specific depolymerase activity of Kip3, a kinesin-8 protein, explains its role in positioning the yeast mitotic spindle. *Nature Publishing Group* **8**, 913–923 (2006).

53. D. De Rosier, A. Klug, Reconstruction of three dimensional structures from electron micrographs. *Nature* **217**, 130–134 (1968).

54. D. DeRosier, P. Moore, Reconstruction of three-dimensional images from electron micrographs of structures with helical symmetry* 1. *Journal of Molecular Biology* **52**, 355–362 (1970).

55. A. Klug, D. De Rosier, Optical filtering of electron micrographs: reconstruction of one-sided images. (1966).

56. R. M. Glaeser, *Electron Crystallography of Biological Macromolecules* (Oxford University Press, USA, 2007).

57. *Cryo-EM Part B: 3-D Reconstruction* (Academic Press, 2010).

58. A. Klug, F. Crick, H. Wyckoff, Diffraction by helical structures. *Acta Crystallographica* **11**, 199–213 (1958).

59. R. Wade, D. Chrétien, D. Job, Characterization of microtubule protofilament numbers* 1:: How does the surface lattice accommodate? *Journal of Molecular Biology* **212**, 775–786 (1990).

60. M. Kikkawa, A new theory and algorithm for reconstructing helical structures with a seam. *Journal of Molecular Biology* **343**, 943–955 (2004).

61. H. Sosa, R. Milligan, Three-dimensional structure of ncd-decorated microtubules obtained by a back-projection method. *Journal of Molecular Biology* **260**, 743–755 (1996).

62. E. Egelman, A robust algorithm for the reconstruction of helical filaments using single-particle methods. *Ultramicroscopy* **85**, 225–234 (2000).

63. E. H. Egelman, The iterative helical real space reconstruction method: surmounting the problems posed by real polymers. *J Struct Biol* **157**, 83–94 (2007).

64. E. Egelman, Single-particle reconstruction from EM images of helical filaments. *Current Opinion in Structural Biology* **17**, 556–561 (2007).

65. C. V. Sindelar, K. H. Downing, The beginning of kinesin's force-generating cycle visualized at 9-A resolution. *The Journal of Cell Biology* **177**, 377–385 (2007).

66. G. M. Alushin *et al.*, High-Resolution Microtubule Structures Reveal the Structural Transitions in αβ-Tubulin upon GTP Hydrolysis. *Cell* **157**, 1117–1129 (2014).

67. W. B. Redwine *et al.*, Structural basis for microtubule binding and release by dynein. *Science* **337**, 1532–1536 (2012).

68. D. Chrétien, R. H. Wade, New data on the microtubule surface lattice. *Biol Cell* **71**, 161–174 (1991).

69. N. Grigorieff, FREALIGN: high-resolution refinement of single particle structures. *J Struct Biol* **157**, 117–125 (2007).

70. G. C. Lander *et al.*, Appion: an integrated, database-driven pipeline to facilitate EM image processing. *J Struct Biol* **166**, 95–102 (2009).

71. V. H. Ramey, H.-W. Wang, E. Nogales, Ab initio reconstruction of helical samples with heterogeneity, disorder and coexisting symmetries. *J Struct Biol* **167**, 97–105 (2009).

72. T. Ogura, K. Iwasaki, C. Sato, Topology representing network enables highly accurate classification of protein images taken by cryo electron-microscope without masking. *J Struct Biol* **143**, 185–200 (2003).

73. S. Scheres, ScienceDirect.com - Journal of Structural Biology - RELION: Implementation of a Bayesian approach to cryo-EM structure determination. *J Struct Biol* (2012).

74. G. M. Alushin *et al.*, The Ndc80 kinetochore complex forms oligomeric arrays along microtubules. *Nature* **467**, 805–810 (2010).

75. G. M. Alushin *et al.*, Multimodal microtubule binding by the Ndc80 kinetochore complex. *Nat Struct Mol Biol* **19**, 1161–1167 (2012).

76. C. V. Sindelar, K. H. Downing, An atomic-level mechanism for activation of the kinesin molecular motors. *Proceedings of the National Academy of Sciences* **107**, 4111–4116 (2010).

77. A. Goulet *et al.*, The Structural Basis of Force Generation by the Mitotic Motor Kinesin-5. *Journal of Biological Chemistry* **287**, 44654–44666 (2012).

78. J. Atherton *et al.*, Conserved mechanisms of microtubule-stimulated ADP release, ATP binding, and force generation in transport kinesins. *Elife* **3**, e03680–e03680 (2014).

79. F. J. Fourniol *et al.*, Template-free 13-protofilament microtubule-MAP assembly visualized at 8 A resolution. *The Journal of Cell Biology* **191**, 463–470 (2010).

80. S. P. Maurer, F. J. Fourniol, G. Bohner, C. A. Moores, T. Surrey, EBs Recognize a Nucleotide-Dependent Structural Cap at Growing Microtubule Ends. *Cell* **149**, 371–382 (2012).

81. E. H. Egelman, Reconstruction of helical filaments and tubes. *Methods in Enzymology Cryo-EM, Part C: Analyses, Interpretation, and Case studies* **482**, 167–183 (2010).

82. H. Sosa, D. Chretien, Relationship between moire patterns, tubulin shape, and microtubule polarity. *Cell Motil. Cytoskeleton* **40**, 38–43 (1998).

83. S. Chowdhury, S. A. Ketcham, T. A. Schroer, G. C. Lander, Structural organization of the dynein-dynactin complex bound to microtubules. *Nat Struct Mol Biol* (2015), doi:10.1038/nsmb.2996.

84. M. Hohn *et al.*, SPARX, a new environment for Cryo-EM image processing. *J Struct Biol* **157**, 47–55 (2007).

85. C. Sorzano *et al.*, XMIPP: a new generation of an open-source image processing package for electron microscopy. *J Struct Biol* **148**, 194–204 (2004).

86. E. Behrmann *et al.*, Real-space processing of helical filaments in SPARX. *J Struct Biol* **177**, 302–313 (2012).

87. J. von der Ecken *et al.*, Structure of the F-actin--tropomyosin complex. *Nature* (2014), doi: 10.1038/nature14033.

88. Z. Shang *et al.*, High-resolution structures of kinesin on microtubules provide a basis for nucleotide-gated force-generation. *Elife* **3**, e04686–e04686 (2014).

Chapter 2

Structural basis for microtubule binding and release by dynein

Rogelio Hernandez-Lopez, William B. Redwine, Siriu Zou, Julie Huang, Samara Reck-Peterson, Andres Leschziner

Contributions

William B. Redwine initiated the project and performed biochemistry, sample preparation, and electron microscopy data collection. Rogelio Hernandez-Lopez and William Redwine performed 3D reconstruction. Molecular dynamics was performed by Rogelio Hernandez-Lopez. Single molecule motility experiments were performed by Sirui Zou and Julie Huang. Andres Leschziner and Samara Reck-Peterson provided mentorship.

Abstract

Cytoplasmic dynein is a microtubule-based motor required for intracellular transport and cell division. Its movement involves coupling cycles of track binding and release with cycles of force-generating nucleotide hydrolysis. How this is accomplished given the ~25 nm separating dynein's track- and nucleotide-binding sites is not understood. Here, we present a sub-nanometer-resolution structure of dynein's microtubule-binding domain bound to microtubules by cryo-electron microscopy that was used to generate a pseudo-atomic model of the complex with molecular dynamics. We identified large rearrangements triggered by track binding and specific interactions, confirmed by mutagenesis and single molecule motility assays, which tune dynein's affinity for microtubules. Our results provide a molecular model for how dynein's binding to microtubules is communicated to the rest of the motor.

Introduction

Dyneins are ATP-driven molecular motors that move towards the minus ends of microtubules (MTs) (*1*). The superfamily includes axonemal dyneins, which power the movements of cilia, and those that transport cargo, which include cytoplasmic dyneins 1 ("cytoplasmic") and 2 ("intraflagellar") (*2*). The transport of organelles, ribonucleoprotein complexes and proteins by cytoplasmic dynein is required for cellular homeostasis, cell-cell communication, cell division, and cell migration (*3*) and defects in these processes result in neurological disease in humans (*4*). Despite cytoplasmic dynein's role in such diverse activities and recent advances in characterizing its structure and motility, many aspects of its molecular mechanism remain poorly understood.

The core of the cytoplasmic dynein holoenzyme is a homodimer of ~500 kDa motor-containing subunits (Figure 2.1 A). The major functional elements include: (a) a "tail" domain required for dimerization and cargo binding (*5*); (b) the force-generating "head" or "motor domain" (*6*, *7*), a ring containing six AAA+ ATPase domains (*8*-*10*); (c) a "linker" connecting the head and tail, required for motility (*6*, *7*, *11*, *12*); (d) the "stalk", a long antiparallel coiled-coil that emerges from AAA4 (*13*, *14*), and (e) the MT-binding domain (MTBD), a small alpha-helical domain at the end of the stalk responsible for binding the MT track (*15*-*17*). Unlike the other cytoskeletal molecular motors, kinesin and myosin, dynein does not have its ATPase and polymer track binding sites located within a single domain. With 25 nm separating AAA1 (purple circle Figure 2.1 A), the main site of ATP hydrolysis, and the MTBD (blue oval), an unresolved question is how dynein coordinates the cycles of nucleotide hydrolysis and MT binding and release required for its motion.

The mechanism coupling nucleotide hydrolysis to MT affinity has been suggested to be sliding in which the two helices in the stalk's coiled-coil adopt different registries by using alternative sets of hydrophobic heptad repeats (*16*, *18*, *19*). Dynein's stalk can be fixed in a specific registry by fusing it to a coiled-coil of known structure, such as that of seryl-tRNA synthetase (SRS) (*18*). Changing the length of the first stalk helix (CC1) relative to the second (CC2) shifts their alignment between high-affinity ("α") and low-affinity ("β+") registries, and alters the affinity of the MTBD for MTs by up to twenty-fold (Figure 2.1 B) (*18*). Engineered disulfide cross-linking in the monomeric dynein motor domain showed that its stalk explores multiple registries in solution, and that a given registry is coupled to a specific MT affinity. Fixing the stalk registry also uncoupled the nucleotide state of the head from MT affinity (*19*).

Understanding the molecular mechanism by which stalk sliding is coupled to nucleotide hydrolysis and MT affinity would be aided by a structure of dynein's MTBD bound to MTs. Crystal structures are available for a low-affinity dynein MTBD fused to SRS through a short segment of the stalk (Figure 2.1 B) (*16*), and an ADP-bound, presumably high-affinity dynein monomer (*14*). Only low-resolution structures of the MT-bound form have been reported (*16*, *20*). Here we describe a cryo-electron microscopy (cryo-EM) reconstruction of the MTBD bound to MTs at sub-nanometer resolution, using a high-affinity version of the SRS-MTBD construct (*18*).

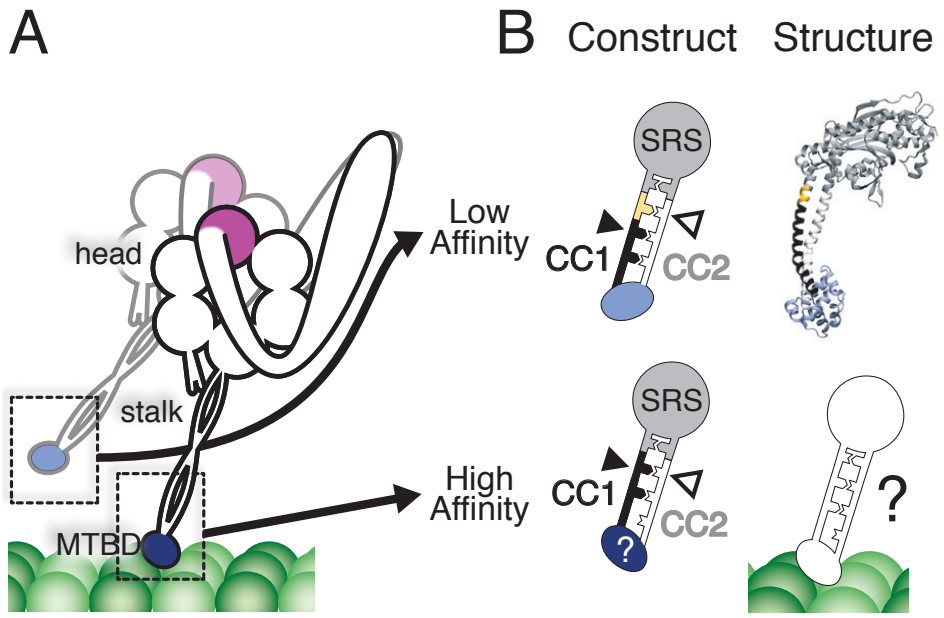


Figure 2.1. Cryo-EM reconstruction of the cytoplasmic dynein high-affinity MTBD bound to a MT.

(A) Schematic of dimeric cytoplasmic dynein. Major features relevant to this study are indicated. The MTBD is depicted in its low- (light blue) and high- (dark blue) affinity states during a step along the MT. (B) Schematic of the fusion constructs between the MTBD and seryl-tRNA synthetase (SRS) that fix the heptad registry of the stalk. The low-affinity construct has an additional 4 amino acids (yellow) inserted in CC1 (black) relative to the high-affinity construct.

Materials and Methods

SRS-MTBD purification

SRS-MTBD chimeric constructs were expressed in the Escherichia coli strain BL21 (DE3) containing the plasmid pLysS. Cells were grown in 8 L of LB broth at 37° C to an optical density at 600 nm of 0.5. The cells were chilled on ice with periodic mixing until the temperature was 16 °C. Protein expression was induced with 0.5 mM β-D-thiogalactopyranoside and the cells were further incubated at 16° C for 6 h. All subsequent steps were performed at 4° C or on ice. Cells were harvested by centrifugation and were resuspended in 70 mL lysis buffer (50 mM Tris-HCl, pH 8.0; 150 mM KOAc, 1 mM EDTA, 10% glycerol, 20 mM imidazole, 5 mM β-mercaptoethanol, 1 mM PMSF, and 1 µg/mL each pepstatin A, aprotinin, benzamidine, and leupeptin). The cells were lysed by sonication (6 continuous pulses at 80% power, with 2 minutes between pulses) and the resulting lysate was centrifuged at 120,000 x g in a Ti45 rotor (Beckman) for 30 min at 4° C. The cleared lysate was applied to a 10 mL Ni-NTA agarose column (Qiagen) by gravity. The column was then washed with 300 mL lysis buffer. Bound protein was then eluted with a linear imidazole gradient from 50 mM to 500 mM. Peak fractions containing the SRS-MTBD fusion, as determined by SDS-PAGE analysis, were pooled, dialyzed for 4 h against lysis buffer, and concentrated to ~15 mg/mL with Ultracell concentration columns with a molecular weight cut-off of 30 kDa (Millipore). A fraction of this protein was then further purified on a Superdex 200 16/60 gel filtration column equilibrated in lysis buffer. A monodisperse peak was isolated and concentrated to ~4 mg/mL as described above.

Tubulin polymerization

Highly purified, glycerol-free tubulin (Cytoskeleton, Inc.) was resuspended in BRB80 (80 mM PIPES-KOH, pH 6.8; 1 mM MgCl2, 1 mM EGTA, 1 mM DTT) to a concentration of 10 mg/mL. The resuspended tubulin was centrifuged at 100,000 x g in a TLA 100 rotor (Beckman) for 30 min at 4 °C to remove aggregates, and the protein concentration was determined using an extinction coefficient of 1.15 $(mg/mL)^{-1}$. Tubulin was then polymerized with a stepwise addition of taxol as follows: 20 µL of tubulin stock was thawed quickly and placed on ice. To this 10 µL of BRB80 supplemented with 3 mM GTP was added and the mixture was transferred to a 37°C water bath. After 15, 30, and 45 minutes, additions of 0.5, 0.5, and 1.0 µL of 2 mM taxol were added by gentle swirling. The mixture was then incubated for an additional 1 h at 37°C.

Grid preparation and imaging

Purified SRS-MTBD protein was dialyzed for 4 h against lysis buffer without glycerol and added salts (cryo buffer: 50 mM Tris-HCl, pH 8.0, 1 mM MgCl2, 1 mM EGTA, 1 mM DTT) in a spin dialyzer (Harvard Apparatus) fitted with a 10 kDa MWCO membrane. The protein was recovered and centrifuged at 20,000 x g in a TLA 100 rotor (Beckman) for 30 min at 4 °C to remove aggregates. C-flat 2/2-2C holey carbon grids (Protochips) were glow-discharged for 20 s at 30 mA in an Edwards carbon evaporator. MTs were diluted to 0.5 mg/mL in cryo buffer supplemented with 100 µM taxol, and 4 µL were added to a grid and allowed to absorb for 30 sec. The solution was manually blotted from the side with a torn Whatman #1 filter paper. Next, 4 µL of dialyzed SRS-MTBD was added and allowed to bind to the MTs for 1 min. The solution was blotted manually again, and the process of addition and blotting of SRS-MTBD was

repeated for a total of three times. The final blotting was done inside the humidity chamber of a Vitrobot Mark IV (FEI) set at 22° C and 100% humidity. The grids were then rapidly plunged into a liquid nitrogen-cooled ethane slush. Grids were stored in liquid nitrogen until imaging.

Grids were transferred to a Gatan 626 cryo-holder, and micrographs were collected on film (SO-163, Kodak) in a Tecnai F20 electron microscope (FEI) operating at 120 keV, and nominal magnification of 62,000. Final accumulated electron doses ranged between 15 and 20 electrons/ $Å^2$. The actual magnification of 63,377 was calculated using tobacco mosaic virus layer lines as a standard. Film was developed using full strength D9 developer (Kodak) for 12 min. Each film was analyzed visually on a light box for drift; those without noticeable drift were digitized on an Aztek Plateau flatbed scanner (Aztek, Inc.) with a 6.35 micron step size, resulting in a final pixel size of 0.994 Å. Images were then selected for processing on the basis of high decoration, straight MTs, and the absence of crystalline ice and drift.

Image processing and three-dimensional reconstruction

Square segments of 720 pixels were extracted from micrographs containing straight MTs using BOXER (*21*) and the "helix" option with 240 pixel overlap. Pixel intensities were normalized and segments were decimated six-fold to a pixel size of 5.964 Å. Reference-free two-dimensional classification was performed as described (*22*, *23*). This method has been shown to sort MT segments on the basis of degree of decoration and protofilament number (PF). After analyzing the power spectrum and one-dimensional projection of class averages, good quality boxes were assigned a PF number of 13, 14 or 15. We assigned PF number based on the consensus of PF number assignment for all boxes extracted from each individual MT. Out of 577

MTs, 189 13-PF and 375 14-PF MTs were selected for further processing.

The primary PF number population in our in vitro assembled MT preparations was 14. To maximize the data used for reconstruction, custom SPIDER scripts (*24*, *25*), previously used in subnanometer reconstructions of 13 PF MT complexes (*24*, *26*), were adapted to 14 PF MTs. Initially, 13 PF and 14 PF MTs were independently processed to validate our implementation. We obtained essentially the same structure at a resolution of 20 Å, at which point the 13 PF reconstruction stopped improving (data not shown).

In our implementation, a PDB model of the SRS-MTBD-MT (PDB 3ERR (*16*) and 1JFF (*27*)) complex was used to generate an initial low resolution volume from which a set of initial projection references was generated to assign the orientation of individual 80 Å experimental segments. The astigmatism and defocus values used to correct the contrast transfer function of the microscope were obtained from micrographs using CTFFIND3 (*28*) and were used during the reconstruction step. Three cycles of alignment using the SPIDER custom scripts with 3 rounds of reconstruction with FREALIGN (*26*) in each cycle, yielded a final 12.0 Å resolution structure (FSC at 0.143, a criterion shown to be reliable (*29*, *30*) for structures refined with FREALIGN. Reconstructions in cycles 1 and 2 were done with data decimated three-fold. In the last cycle the reconstruction was carried out at finer pixel sampling (1.988 Å). Within each cycle the reconstruction with the highest resolution was used to create new references that were used for a subsequent cycle of alignment. Helical parameters for three-dimensional reconstruction were obtained using the hsearch_lorentz program (*31*). The helical rise and angle converged to 9.26 Å and -25.76° respectively. For three-dimensional reconstruction, a recent implementation of a helical symmetry operator in FREALIGN was used (*23*). In this algorithm, each 80 Å segment is

included multiple times in the reconstruction, using the Euler angles and shifts, to generate symmetrically equivalent views. Due to the presence of the seam in the 14 PF MTs, each segment was inserted 14 times. As previously described (*24*, *25*), the symmetrization step causes the output reconstruction from FREALIGN to contain a single PF with all asymmetric subunits in registry. A SPIDER script was used to rebuild the MT containing the correct seam position, as described (*32*). Our final reconstruction contains data from 191 MTs equivalent to 10,419 80 Å segments or 145,866 individual tubulin dimers. Visual inspection of our reconstruction after sharpening the map revealed that the resolution for the portion of the map corresponding to the SRS is lower than the portion containing the MT-MTBD interface. We applied a cylindrical soft mask to exclude the density corresponding to the SRS and measured the resolution of the map in its absence. The resolution of the MT-MTBD map calculated from half volumes of the final reconstruction is 9.7 Å (FSC 0.143 criterion), which is more consistent with our ability to see secondary structural elements in portions of the map. The final map was sharpened using Gaussian low-pass and high-pass filters at 9.75 and 30 Å, respectively, and the high-resolution amplitudes were scaled using a b-factor of -200 $Å^2$ using the program BFACTOR with the cosine edge mask option with a radius of 9.5 Å.

Flexible fitting and targeted molecular dynamics

Our Experimental 3D map was segmented to obtain a density comprising an asymmetric tubulin dimer unit using UCSF Chimera (*33*). The atomic resolution structures for the MTBD (PDB 3ERR (*16*)), excluding 4 residues (3360 to 3363); and tubulin, obtained after flexible

fitting into a MT density (*34*), were used for rigid body docking using UCSF Chimera. Molecular dynamics flexible fitting (MDFF) (*35*, *36*) and targeted molecular dynamics (TMD) (*37*) were utilized to obtain a pseudo-atomic model of the high affinity MTBD-MT complex.

Initially, the MTBD-Tubulin system was minimized for 2000 steps and then a vacuum MDFF simulation was run for 100 ns at 300K, using a dielectric constant of 80 and a force scaling factor (ξ) of 0.5 kcal/mol. Restraints on secondary structure elements and chiral atoms were used as described (*36*). After the simulation in vacuum, the system was embedded in a box of water molecules using the VMD plugin "Solvate" with a 10 Å distance from the closest protein atoms to the box edge. The VMD plugin "Autoionize" was used to randomly place potassium and chloride ions that simulate a final KCl concentration of 0.05 M. All-atom molecular dynamics simulations were performed using the software NAMD 1.7b2 (*38*), the CHARMM27 force field with CMAP correction terms (*39*) and the TIP3P water model (*40*). The same parameters for the GDP and GTP molecules were used as described (*34*). The system was minimized for 2000 steps followed by 10 ns of MDFF at 300 K using a force-scaling factor (ξ) of 0.5 kcal/mol and constraints on secondary structure elements and chiral atoms. During MDFF simulations, the temperature was kept constant at 300K using Langevin dynamics with a damping coefficient of 5 ps-1. The long-range electrostatic interactions were calculated using the Particle Mesh Ewald method (PME) and the van der Waals interactions were computed with a 10 Å cutoff using periodic boundary conditions. After the MDFF simulation in explicit solvent the system was equilibrated for 10 ns in the NPT ensemble (see below).

After these simulations, we observed a rearrangement of the helices that form the MTBD, with no apparent shift in the registry of the stalk. As our cryo-EM data was collected with a

construct known to exist in the high affinity registry, TMD (*37*) was performed on the Cα atoms of residues 3264-3280 using a 200 kcal/molÅ2 force constant. In TMD, the positions of selected atoms are driven into the target positions by using an additional potential energy term in which the root-mean-squared deviation between the simulated and target position is minimized during the simulation. Using this approach, the registry shift from low- to high-affinity was obtained, whereas the rest of the atoms were still driven by the cryo-EM map using MDFF. Fifteen ns of MDFF/TMD at 300 K using a force-scaling factor (ξ) of 0.5 kcal/mol and constraints on secondary structure elements and chiral atoms were carried out.

To confirm that the structure for the dynein high affinity MTBD state does not depend on the multistep simulations that we carried out, we ran additional simulations as follows: the starting crystal structures of tubulin and the low-affinity MTBD (described above) were rigid body docked into our density, the output system was solvated and ions were randomly placed as described above. The system was minimized for 1000 steps followed by 20 ns of MDFF/TMD at 300 K using a force-scaling factor (ξ) of 0.5 kcal/mol and constraints on secondary structure elements and chiral atoms. A similar high affinity MTBD structure was obtained.

Equilibration simulations

After the MDFF/TMD simulations, the system was equilibrated for 20 ns in the NPT ensemble at 300 K and 1 atm using the Nose-Hoover Langevin piston with a 200 fs decay period and a 50 ps^{-1} damping time constant for the pressure and 0.1 ps^{-1} for the temperature. PME was used for long-range electrostatic interactions and a 12 Å cutoff (switching function at 10 Å) for

van der Waals interactions. A uniform integration step of 2 fs was used during these simulations. The backbone coordinates of tubulin and residues 3411 to 3427 in the dynein MTBD were constrained using harmonic forces with a force constant of 1 kcal/molÅ^2 to keep fixed the center of mass of the molecules. During the 10 first ns of these simulations, TMD with 100 and 50 kcal/molÅ^2 force constants, on the same atoms described above, were used. All TMD constraints were released during the last 10 ns.

Additional simulations were run using the low-affinity MTBD and tubulin structures without any external force, and using TMD to induce the registry shift, both without the presence of our experimental map. The systems were prepared using the tubulin coordinates obtained after equilibration of the high-affinity MTBD-Tubulin complex (see above) and the crystal structure coordinates of the low-affinity construct (PDB 3ERR (*16*)). The positions of residues 3388 to 3426 were used to align the dynein MTBD low- and high-affinity structures, as they were unchanged in both conformations. The MTBD-tubulin complex coordinates were embedded in a box of explicit water molecules and KCl ions as described above. In the case of the TMD simulations, restraints on secondary structure elements and chiral atoms were used to avoid structural distortions of the protein. Fifteen ns of TMD simulations were carried out with the same parameters as the MDFF/TMD simulation described above. The simulation of the low-affinity MTBD structure on MTs included 100 ps simulation with constraints in all backbone atoms with a force constant of 1 kcal/molÅ^2 followed by a 15 ns equilibration simulation in the NPT ensemble as described above. In the absence of the map forces, the repositioning of the helices H1, H3 and H4 was not observed during the simulated time scale, though favorable interactions between the dynein low-affinity conformation and tubulin were detected.

Analysis of trajectories

The last 10 ns of equilibration simulations were used to perform trajectory analysis using VMD (*41*). The RMSD of the high- and low-affinity MTBD equilibrated structures was measured and its convergence supports the stability of the conformers. Salt bridges were monitored if the donor-acceptor distance was less than 3.2 Å. Hydrogen bonds were counted if the donor-acceptor distance was less than 3.0 Å with a 20° cutoff for the angle formed by the donor, hydrogen, acceptor. Figures depicting molecular structures were created with UCSF Chimera (*33*) and VMD (*41*).

Comparison of our experimental high-affinity map with synthetic maps

To compare the conformational changes described by our MD-generated pseudo-atomic models with our experimental density, we generated 10 Å resolution synthetic maps of the low and high affinity conformations using SPIDER and fitted them into our experimental cryo-EM map. At this resolution secondary structure elements such as alpha helices are visible as discrete regions of density in both our synthetic and experimental maps. We calculated the cross-correlation coefficient between each of the synthetic maps and our experimental cryo-EM map (*36*). The higher similarity between the synthetic map of the high-affinity state and our experimental density (CCC 0.751) when compared to the low-affinity conformation (CCC 0.648) indicates that our map describes the large conformational changes seen in our pseudo-atomic models. In particular, the density corresponding to H1 in the low-affinity synthetic map is completely absent in our experimental EM density, whereas the high-affinity synthetic map

shows a very good match to the experimental density.

Flexible fitting of Kon et al. MTBD

We performed MDFF using our EM map and the atomic coordinates of the MTBD of an ADP-bound dynein monomer (PDB 3VKH (*14*)). This structure has the stalk's coiled-coil in the α registry but its MTBD has the same conformation as the low-affinity MTBD previously reported by Carter et al. (*16*). The crystal structures of MDFF tubulin (described above) and the MTBD (residues 3352 to 3491) were rigid-body docked into our density, the initial coordinates for the complex were solvated, and ions were randomly placed as described above. The system was minimized for 2000 steps followed by 12 ns of MDFF at 300 K using a force-scaling factor (ξ) of 0.5 kcal/mol and constraints on secondary structure elements and chiral atoms. A similar high-affinity conformation for the MTBD region (backbone RMSD 3.3 Å relative to residues 3285 to 3402 in the high-affinity conformation described above in this study) was obtained. During this simulation we observed that the final position of CC1 deviates from the one observed in our previous simulations, likely because of the absence of coordinates for the CC2 residues in the distal portion of the coiled-coil of the crystal structure reported by Kon et al.

Two-dimensional analysis of monomeric S. cerevisiae dynein bound to microtubules

Monomeric dynein protein was purified as described for dimeric dynein (*11*), bound to MTs, and imaged under cryogenic conditions. MTs were polymerized and grids were prepared as described above. Images were collected on a US4000 4k x 4k CCD (Gatan) in a Tecnai F20 electron microscope (FEI) operating at 200 keV, and nominal magnification of 50,000. Square segments of 600 x 600 pixels with 80 % overlap were extracted and alignment and classification

of data binned by 3 (final pixel size of 6.42 Å) was performed using a previously reported strategy (*22*).

Estimating the conformation of monomeric dynein on microtubules

We noticed that rigid body docking of the Kon et al. dynein monomer crystal structure (*14*) via its MTBD into our reconstruction results in the dynein head clashing with the MT. Using our MDFF-generated Kon et al. MTBD (described above) we ran additional targeted molecular dynamics simulations to position CC1 according to our high-affinity model (to correct for the deviation in CC1 due to the absence of CC2 in the Kon et al. structure). We then modeled the structure of the entire monomer using the remaining portion of the monomer crystal structure (PDB 3VKH (*14*)).

S. cerevisiae strain construction

Mutations were inserted into a truncated dynein construct that is dimerized with GST as described previously (*11*). All mutations were verified by DNA sequencing. The wild type form of this construct has been shown to have near identical properties as full-length cytoplasmic dynein (*11*).

Yeast dynein purification

Cultures of S. cerevisiae for protein purification were grown, harvested, and frozen as previously described (*11*). Dynein constructs were purified via their ZZ tags and labeled with HaloTag-TMR (Promega) as described (*11*).

Total Internal Reflection Fluorescence Microscopy (TIRF)

Fluorescently-labeled molecules were visualized using an Olympus IX-81 TIRF microscope with a 100X 1.45 N.A. oil immersion TIRF objective (Olympus) and two CW diode-pumped solid state lasers (491nm and 561nm, Cobolt). Laser power at the objective was 1.5 – 2 mW. Images were recorded with a 100 ms exposure on a back-thinned electron multiplier CCD camera (Hamamatsu), controlled by Metamorph software.

Single-molecule motility assays of mutant dyneins (Figure 2.13, 14, 15, 16) were performed with MTs containing HiLyte Fluor™ 488- and biotin-labeled tubulin (Cytoskeleton, Inc.). MTs were prepared as described (*42*). Single-molecule motility assays that addressed the effect of increasing ionic strength (Figure 2.10) on dynein motility utilized Cy5-labeled axonemes prepared as described (*11*). All assays utilized a flow chamber as described (*11*), with the following modification: TMR-labeled dynein motors were added to motility chambers in the presence of motility buffer [30 mM HEPES (pH 7.2), 2 mM MgOAc, 1 mM EGTA, 10% glycerol, 1 mM DTT, 1 mM Mg-ATP, and an oxygen scavenger system] (*11*). To determine the effect of ionic strength on dynein motility, assay buffer was supplemented with 20, 40, 60, or 80 mM KAc (Figure 2.10), or 50 mM KAc (Figure 2.13, 14, 16), or 50 mM KAc + 50 mM KCl (Figure 2.Figure 2.16). Images were recorded every 2 s for 10 min, and velocities and run lengths were calculated from kymographs generated in ImageJ (NIH) as described (*11*). Run lengths were not corrected for photobleaching of fluorophores, as this rate was determined to be negligible (data not shown).

Preparation of tubulin lacking C-terminal E-hooks

Polymerized biotin-labeled MTs (described above) were incubated with subtilisin at the

ratio of 5:1 (w/w of tubulin:subtilisin) for 1 h at 37°C. The reaction was stopped by adding 2 mM phenylmethylsulfonyl fluoride (PMSF). The digestion was monitored by SDS-PAGE to confirm complete cleavage. TIRF microscopy with subtilisin treated MTs was performed as described above.

Results

We collected images of MTs highly decorated with the SRS-MTBD under cryogenic conditions (Figure 2.2 A, Figure 2.3 A), and adapted an image processing method (*24*, *32*) to solve its structure bound to 14-protofilament MTs. The SRS-MTBD binds to α-tubulin and β-tubulin at the intradimer interface and is positioned to the side of the protofilament, as previously reported (*16*, *20*) (Figure 2.2 B, Figure 2.3 B). In the reconstruction, the portion including the MT, the MTBD and the beginning of the stalk has a resolution of 9.7 Å (Figure 2.3 D), where α-helices become visible.

We used molecular dynamics (MD) and our cryo-EM reconstruction to obtain pseudo-atomic models of the low- and high-affinity states of the MTBD bound to MTs. First, we rigid-body docked the atomic-resolution structures of the tubulin dimer (*27*, *34*) and the low-affinity MTBD into our map (Figures 2-4 A, C, and 2-5 A) and used MD to resolve steric clashes between a helix (H1) in the MTBD and the MT (Figures 2-4 A, C and 2-5 A, B). We then performed explicit-solvent molecular dynamics flexible fitting (MDFF) to shift the low-affinity MTBD structure to the high-affinity conformation in our reconstruction (Figure 2.5 C). In addition to the MD force field, MDFF uses a potential energy term derived from the experimental map and restraints on secondary structure to drive conformational changes that better fit the map (*35*, *36*). The initial MDFF model agreed well within the experimental density of the MTBD (Figure 2.5 C); however, the stalk remained in the low-affinity β+ registry present in the starting model. MDFF likely did not shift the registry of the coiled-coil due to the lower resolution at the tip of the stalk segment (Figure 2.3); a movement of the CC1 helix to the α registry would make it protrude from the map, incurring a

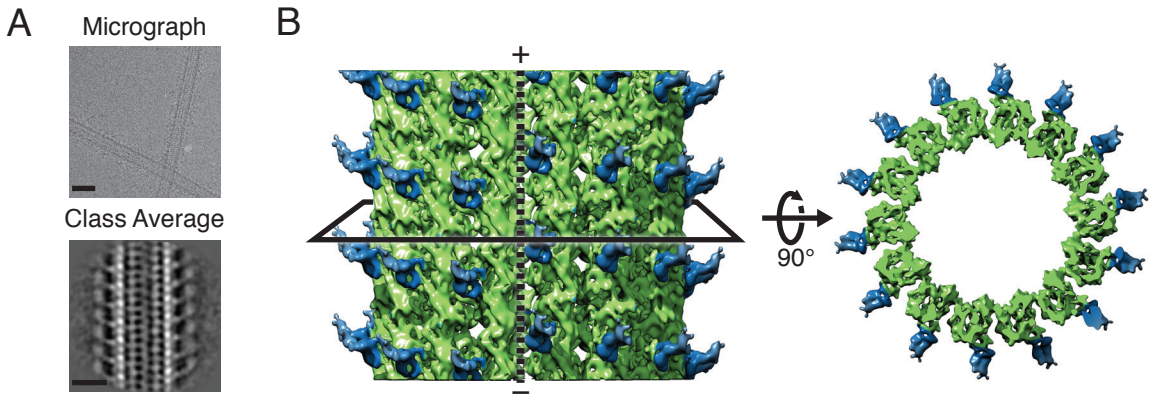


Figure 2.2. Three dimensional reconstruction of dynein's MTBD bound to the microtubule. **(A)** Cryo-EM image of MTs highly decorated with the high-affinity SRS-MTBD construct (top) and a class average generated from segments of decorated 14-protofilament MTs (bottom). Scale bars: 25 nm. (**B**) Three-dimensional reconstruction of the MTBD-MT complex, filtered to the calculated resolution of 9.7 Å (Figure 2.3). The black solid line represents a slice through the volume, which is shown on the right viewed from the minus end of the MT. The MT polarity is indicated and the dashed line shows the location of the MT seam. The SRS has been omitted due to its lower resolution (Fig. 2.3).

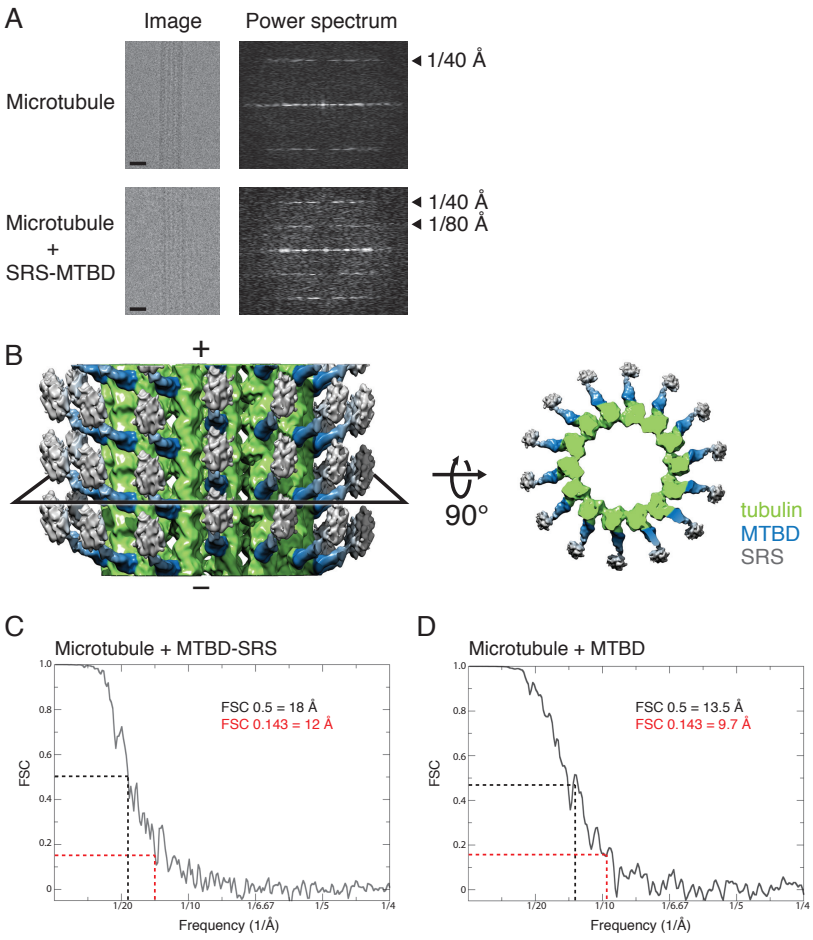


Figure 2.3. Complete reconstruction of the high-affinity SRS-MTBD construct bound to a MT.

(**A**) Left: Images containing MTs only (top) and MTs highly decorated with the high-affinity SRS-MTBD (bottom). Scale bar represents 20 nm. Right: Corresponding power spectra of the MTs. Note the layer lines at 1/40 Å and 1/80 Å, which correspond to the repeated units of tubulin monomers and SRS-MTBD, respectively. (**B**) Left: A segment of the MT + SRS-MTBD reconstruction low-pass filtered to 12 Å. MT polarity is indicated by plus and minus signs. Note that the stalk emerges from the MT at an angle of ~60º, consistent with previous observations (*16*, *20*). Right: A slice taken through the volume, related to the complete reconstruction by a 90º rotation, such that the viewer is looking down the MT from the minus end. The color of each component is indicated and refers to both views. (**C**) The estimated resolution of the complete volume, including the SRS, is 12 Å, using the 0.143 criterion (red dashed line). (**D**) The estimated resolution of the volume containing only the MT and MTBD is 9.7 Å, using the 0.143 criterion (red dashed line). The discrepancy in resolutions is likely due to a relatively less constrained SRS domain decreasing the overall resolution of the structure.

penalty in the simulations. We achieved the shift by applying targeted molecular dynamics (TMD) (*37*) to the tip of the coiled-coil (Figure 2.5 D), using the Cα coordinates of the half-heptad shift in our construct to guide the final position of the stalk during the simulations. This final model (Figure 2.4 B, D), which we refer to as the high-affinity MTBD, has the highest cross-correlation with the experimental map (Figures 2-5 and 2-6).

We repeated the MDFF calculations using the MTBD from the recent crystal structure of an ADP-bound dynein monomer (*14*) (Figure 2.7). The only difference in the resulting pseudo-atomic model is in the stalk, where the dynein monomer's structure is missing density for one of the helices next to the MTBD (Figure 2.7 A, B). The similarity in the crystal structures of the MTBD in the low-affinity and ADP-bound states is likely due to the absence of MTs; our results suggest that the conformation we observe in our MT-bound high-affinity structure is stabilized by its interactions with β-tubulin (Figure 2.8 A, Tables 1-1 and 1-2). MDFF of the ADP-bound dynein monomer's MTBD into our cryo-EM map results in a large change in the angle between the MTBD and the stalk in the dynein monomer structure (Figure 2.7 A, B). This change makes the docking of the dynein monomer into our map compatible with previously reported measurements of the MT-stalk angle (*16*, *20*) and our two-dimensional analysis of images of monomer-decorated MTs (Figure 2.7 D, E).

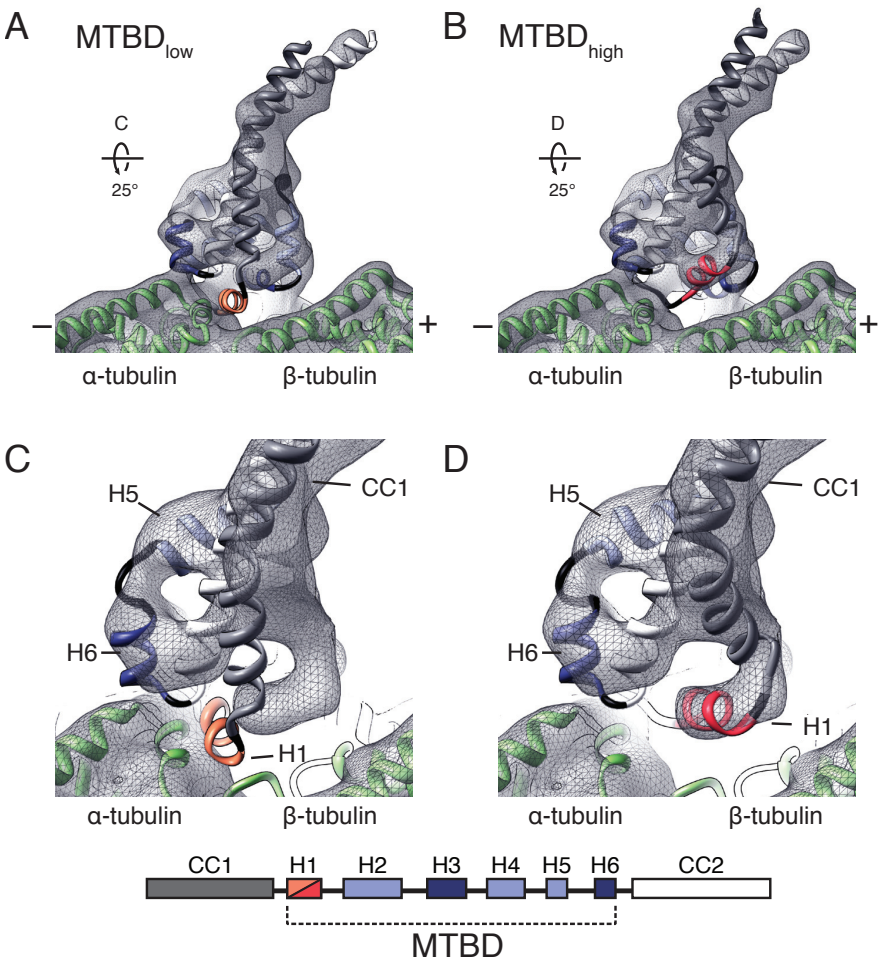


Figure 2.4. The high-affinity, MT-bound state of the dynein MTBD is characterized by repositioning of helices H1 and CC1.

(**A**) Rigid-body docking of the low-affinity MTBD structure into our cryo-EM density. (**B**) Pseudo-atomic model of the high-affinity MTBD bound to MTs generated by Molecular Dynamics Flexible Fitting (MDFF) and Targeted Molecular Dynamics (TMD) (see text for details). (**C**) Close-up of the structure shown in (A), with its orientation indicated in panel (A). (**D**) Close-up of the structure shown in (B), with its orientation indicated in panel (B). The cryo-EM map is shown as a transparent grey mesh. The MTBD is colored following the scheme shown at the bottom of the figure and structural elements are indicated in the different views. H1 (orange/red) is the element with the largest movement in the transition to the high-affinity conformation; H3 and H6 (dark blue) are major contact points with the MT (green). α- and β-tubulin are indicated (green). MT polarity is indicated in panels A and B. H1 protrudes from the cryo-EM map and clashes with the MT in the rigid-body docked low-affinity state (A and C).

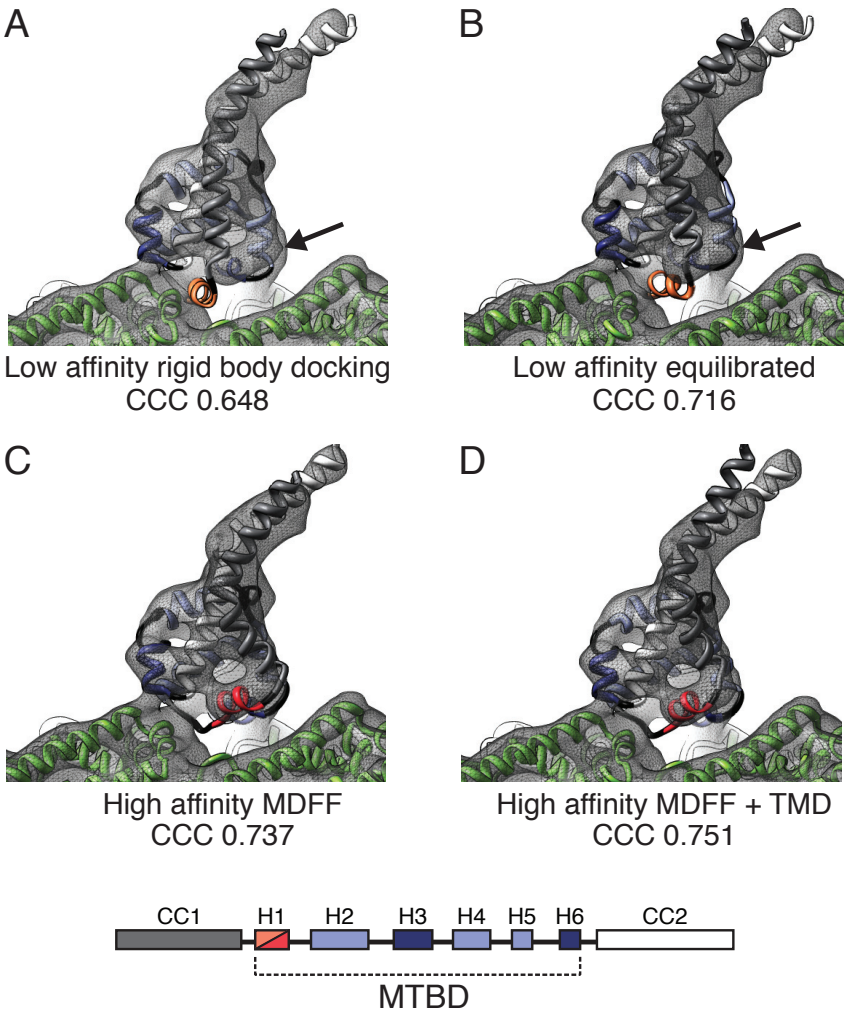


Figure 2.5. Molecular Dynamics study of the dynein MTBD conformations bound to MTs. (**A**) Crystal structures of the low-affinity conformation (PDB 3ERR (*16*)) and tubulin (*34*) rigid-body docked into our cryo-EM density map. H1 is shown in orange and displays steric clashes with the MT. Adjacent to H1 is an unoccupied portion of the map (black arrow). (**B**) Pseudo-atomic model of the low-affinity conformation bound to MTs obtained after 15 ns of MD simulations. H1 moves to a position that avoids clashes with the MT. (**C**) Pseudo-atomic model of a putative intermediate state obtained after molecular dynamics flexible fitting (MDFF). The repositioning of H1 and H3 is achieved but the coiled-coil registry is still in the low-affinity conformation. (**D**) Pseudo-atomic model of the dynein MTBD in its high-affinity state obtained after MDFF and targeted molecular dynamics (TMD). The coordinates of the Cα atoms corresponding to a shift of half heptad (4 aa) were used as a target position to guide the registry shift. The cross-correlation coefficient (CCC) between the target density map and each structure at 9.7 Å resolution is indicated below each panel. Color-coding is indicated for each set of structures.

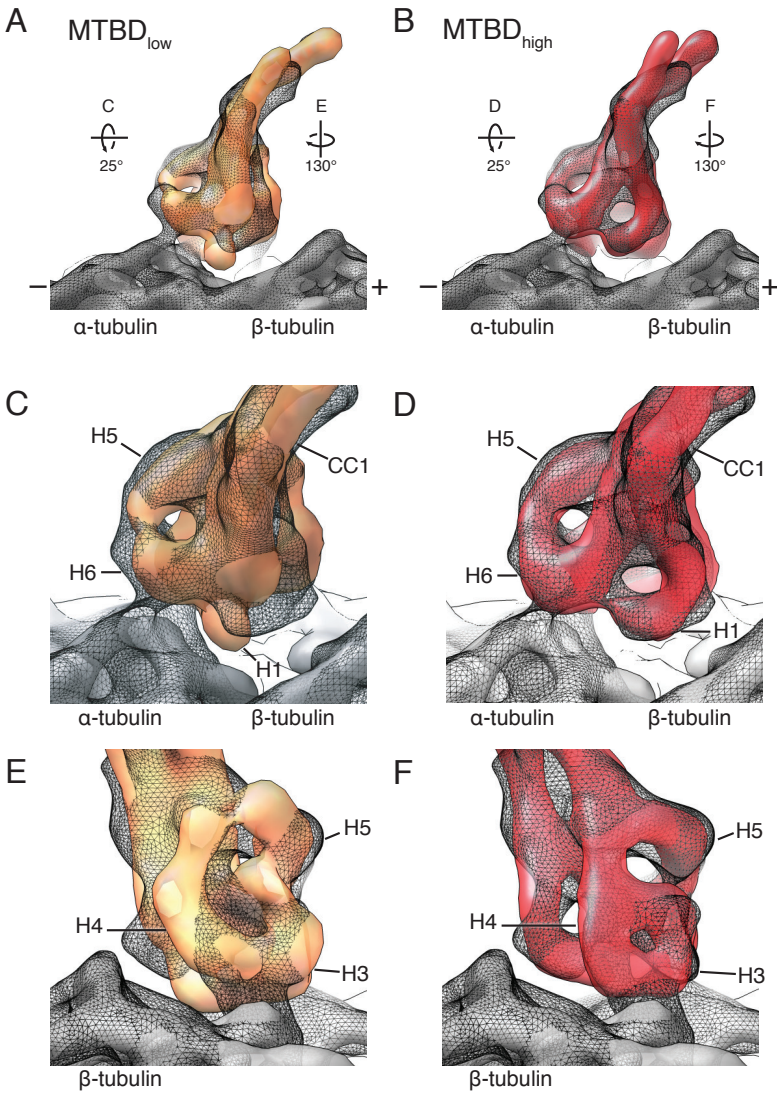


Figure 2.6. Comparison of 10 Å synthetic maps of the low- and high-affinity MTBD conformations with our experimental map.

The stalk and MTBD of the low-affinity conformation (PDB 3ERR (*16*)) and the pseudo-atomic model of the high-affinity conformation of the MTBD were converted to synthetic EM maps, filtered to a resolution of 10 Å, and oriented relative to the cryo-EM map identically to the atomic models shown in Fig. 2.4 (**A**) 10 Å synthetic map of the low-affinity conformation ($MTBD_{low}$, orange) docked into the cryo-EM map (grey mesh). (**C, E**) Close-ups of the structure shown in (A); the direction of each view is indicated in panel (A). (**B**) 10 Å synthetic map of the pseudo-atomic model of the high-affinity conformation ($MTBD_{high}$, red) docked into the cryo-EM map. (**D, F**) Close-ups of the structure shown in (B); the direction of each view is indicated in panel (B). The synthetic map of the low-affinity conformation protrudes from our experimental map at several locations (CCC = 0.648), including H1 (C) and H4 (E). In contrast, the synthetic map of the pseudo-atomic model exhibits a better overall fit to our experimental map (CCC = 0.751).

Figure 2.7

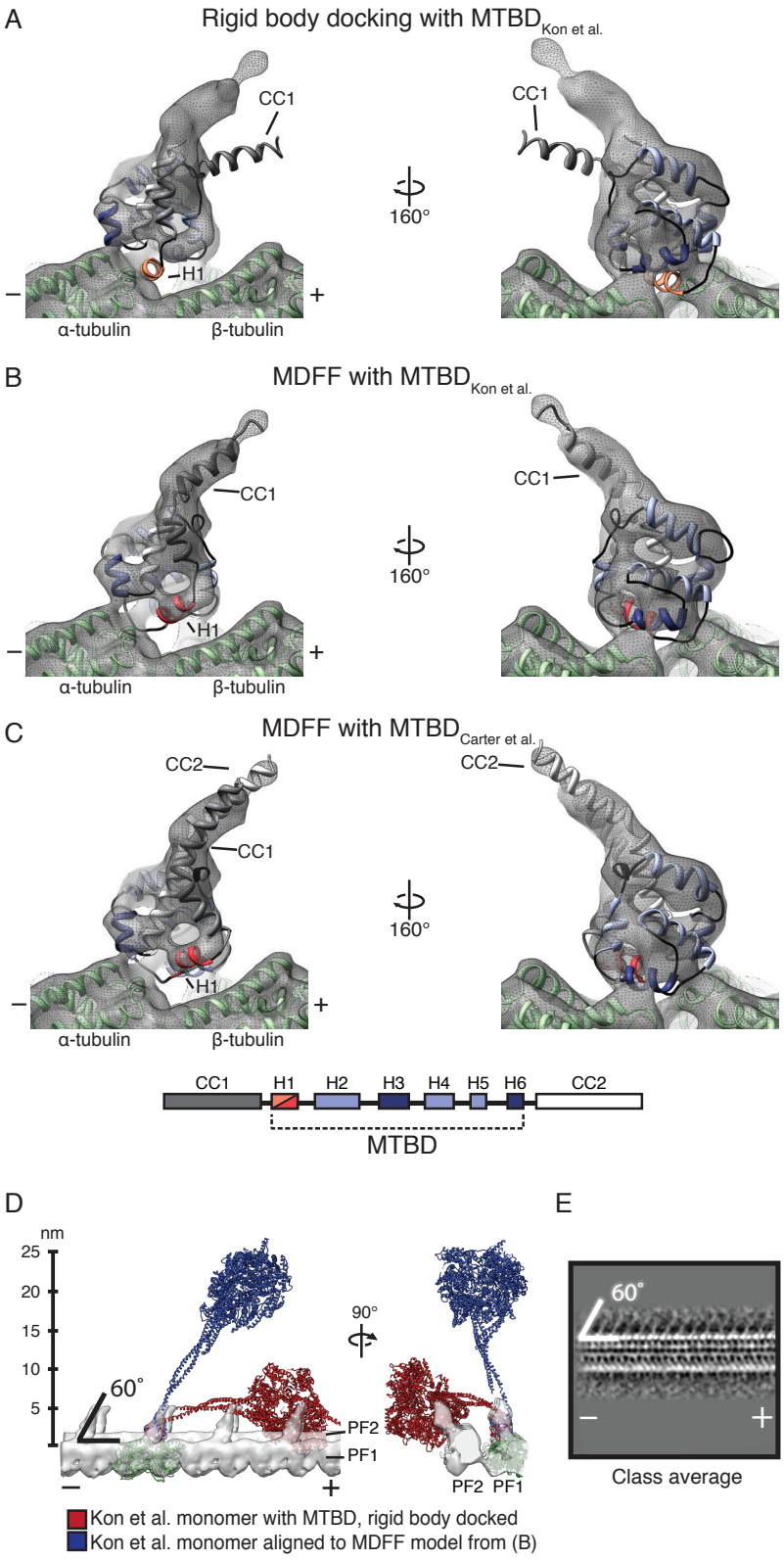

A
Rigid body docking with MTBD Kon et al.
CC1
H1
160°
α-tubulin
β-tubulin
B
MDFF with MTBD Kon et al.
CC1
H1
160°
α-tubulin
β-tubulin
C
MDFF with MTBD Carter et al.
CC2
CC1
H1
160°
α-tubulin
β-tubulin
CC1 H1 H2 H3 H4 H5 H6 CC2
MTBD
D
nm
25
20
15
10
5
60°
90°
PF2
PF1
E
60°
Class average
Kon et al. monomer with MTBD, rigid body docked
Kon et al. monomer aligned to MDFF model from (B)

Figure 2.7. Different atomic resolution structures of the MTBD converge on a single MT-bound conformation (Continued)
(**A**) The MTBD from a recently reported atomic resolution structure of ADP-bound monomeric dynein (PDB 3VKH (*14*)), labeled $MTBD_{Kon\ et\ al.}$), was rigid-body docked into the experimental map. Note that helices H1 (orange) and CC1 (grey) lie outside of the experimental map. (**B**) Conformation of $MTBD_{Kon\ et\ al.}$ after 12 ns of MDFF. Helices H1 (red) and CC1 (grey) have moved into our experimental map. The conformation of the MTBD used in this study (PDB 3ERR (*16*)) after MDFF ($MTBD_{Carter\ et\ al.}$) is shown for comparison (**C**). Note the similarity of the MDFF models in (B) and (C). (**D**) The atomic resolution structure of ADP-bound monomeric dynein (*14*), shown in red, was rigid body docked into a section of one protofilament (PF1) of the experimental map. The orientation of the MTBD is shown in (A). Tubulin is colored green. The resulting conformation of the entire monomer results in clashes with the neighboring protofilament (PF2). A second monomer model (blue) was obtained by replacing the MTBD (residues 3352 to 3491) from the crystal structure with the MDFF-generated $MTBD_{Kon\ et\ al.}$ shown in (B) (See material and methods for details). The monomer containing the MDFF-generated $MTBD_{Kon\ et\ al.}$ exhibits no clashes with our experimental map, and its overall configuration closely matches class averages of *S. cerevisiae* monomeric dynein bound to MTs (E). For panels (D) and (E) the approximate angle of the stalk relative to the MT (~60°) is indicated. For all panels MT polarity is indicated.

The cryo-EM map shows three points of density between the MT and dynein's MTBD: the H1-H2 loop and helices H3 and H6 (Figure 2.4). Several parts of the structure are unchanged by its interaction with the MT, especially helices H6, H5, and CC2, with root mean square deviations (RMSD) between the low- and high-affinity models of 1.4 Å, 1.4 Å, and 1.8 Å, respectively. The largest changes are the repositioning of H1 (RMSD = 10.1 Å) and an opening of CC1 in the coiled-coil next to the MTBD (RMSD = 8.1 Å) (Figure 2.3 A-D), a movement anchored at the proline kink present in CC1. The final position of H1 is stabilized by multiple interactions with an acidic patch in H12 of β-tubulin not fully occupied in the low-affinity state (Figure 2.8 A). This patch also stabilizes the high-affinity state of kinesin (*43*).

We monitored hydrogen bonds and salt bridges formed between the MTBD and the MT during MD simulations (Tables 1-1 and 1-2); the high-affinity MTBD formed more hydrogen bonds with the MT (Figure 2.9) and electrostatic interactions at H1, H3, and H6 (Figure 2.8, Table 1-1). Nearly all of these residues are highly conserved, and mutating them results in defects in MT binding (*18*, *44*) (Figure 2.8). The importance of salt bridges to the MTBD-MT interaction is consistent with the sensitivity of dynein's motility to ionic strength (Figure 2.10).

Figure 2.8

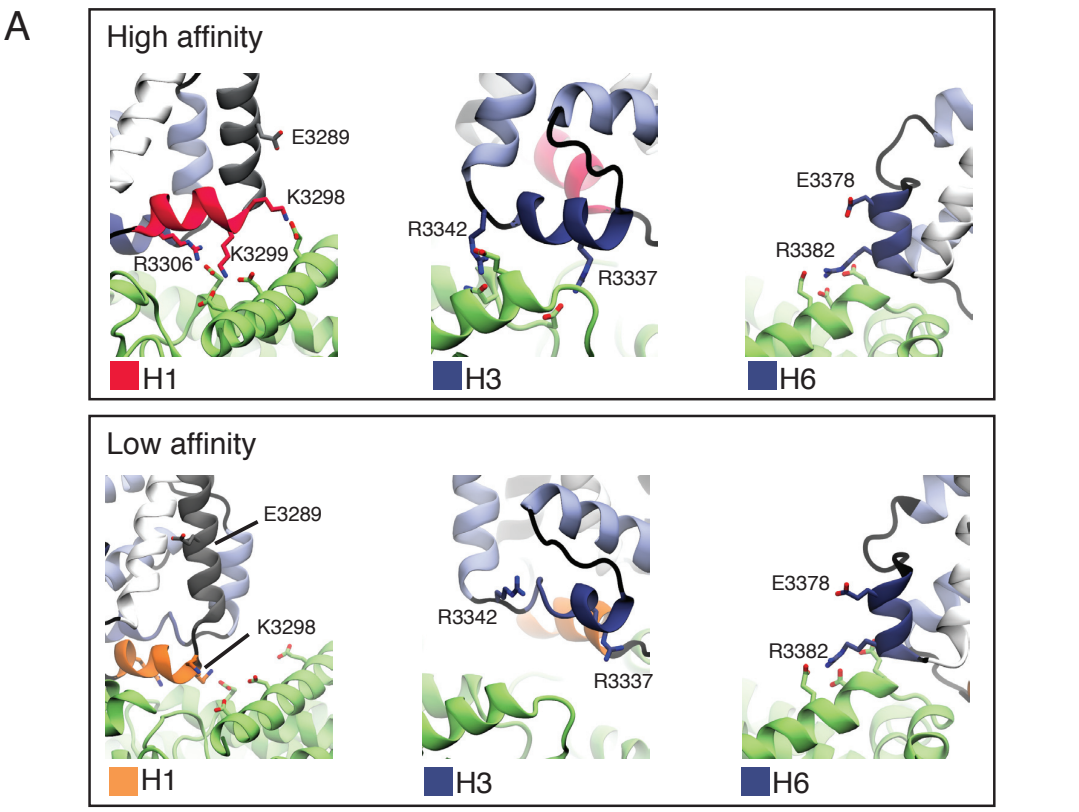

A
High affinity
E3289
K3298
K3299
R3306
R3342
R3337
E3378
R3382
H1
H3
H6
Low affinity
E3289
K3298
R3342
R3337
E3378
R3382
H1
H3
H6
B
E3289
K3298
K3299
R3306
P3311
W3333
R3337
R3342
D. discoideum
M. musculus
S. cerevisiae
C. thermophilum
N. crassa
C. elegans
D. melanogaster
H. sapiens
CC1
H1
H2
H3
E3378
R3382
H4
H5
H6
CC2
Koonce and Tikhonenko, 2000
enhanced binding
no binding
poor release from MT
This study
Microtubule-MTBD salt bridge
MTBD intramolecular interaction

Figure 2.8. Conserved intermolecular MTBD-MT and intramolecular MTBD interactions in the dynein high-affinity state (Continued)
(**A**) Top: Salt bridges formed between the MTBD and the MT, as detected by MD simulations in the high-affinity pseudo-atomic model, are labelled within the indicated helices of the MTBD. Bottom: The corresponding views for the MT-bound low-affinity state are shown. Tubulin is colored green. (**B**) Alignment of the MTBD from diverse cytoplasmic dynein sequences calculated with MAFFT (52) and visualized with Jalview (*45*) according to the Clustal coloring scheme for residues with identity ≥ 50%. Of interest to this study, basic and acidic residues are colored red and purple, respectively. Residues that are conserved between *Dictyostelium discoideum* (*Dd*) (*44*) and *Mus musculus* (*Mm*) (*18*) and form salt bridges with MT residues are labeled and annotated according to the legend above. One *Mm* residue, R3342, forms a salt bridge with the MT and is not present in *Dd* dynein. Intramolecular MTBD salt bridges (E3289-K3298 and E3378-R3382 (Figure 2.11) are connected with a dashed line, as is an intramolecular interaction between P3311 and W3333, which is maintained in both high- and low-affinity states.

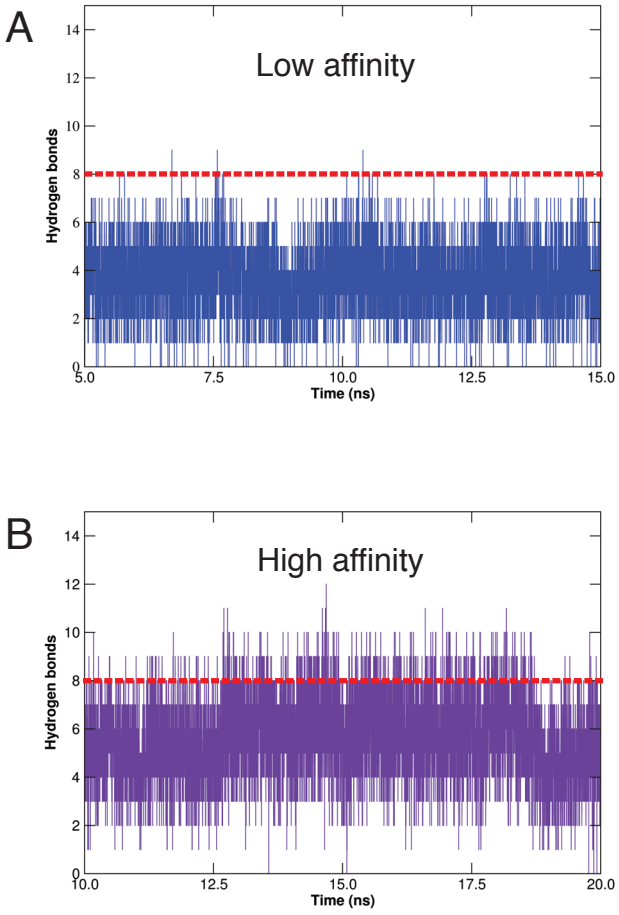


Figure 2.9. Formation of hydrogen bonds between the dynein MTBD and tubulin during MD simulations.

Hydrogen bonds formed between the dynein MTBD and tubulin over time are shown for the (**A**) dynein low-affinity state and the (**B**) dynein high-affinity state. Hydrogen bonds were counted for the last 10 ns of the final MD equilibration simulations when the distance between the donor and acceptor was within 3.0 Å and the angle between donor and hydrogen-acceptor was greater than 160° . A dashed line marks the same point on the y-axis in both graphs.

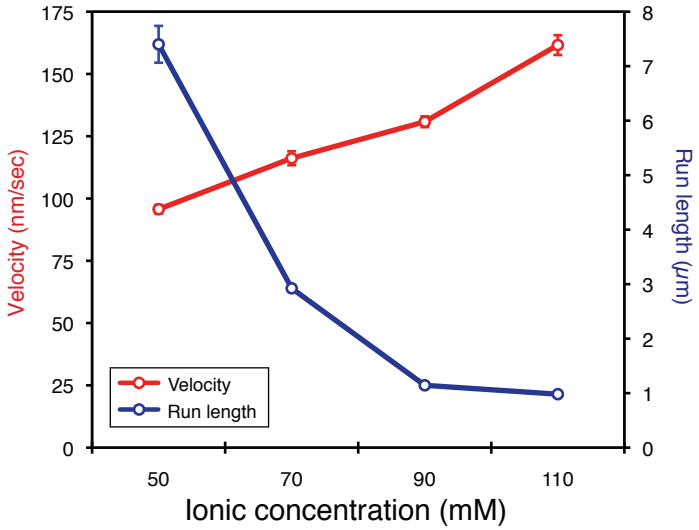


Figure 2.10. Effect of increasing ionic strength on dynein motility.
Fluorescently labeled dynein motors were tracked on axonemes by total internal reflection (TIRF) microscopy. The run length and velocity were determined in assay buffer supplemented with increasing concentrations of potassium acetate (KAc). Total ionic concentration is the sum of added KAc and a constant concentration of buffering agent. The run length at each point is the mean ± standard deviation. The velocity at each point is the mean ± standard error. The average length of analyzed axonemes (mean ± standard deviation) was 24.5 ± 8.0 μm.

Our structural analysis suggested that the MTBD contains residues that lower its own affinity for the MT. In the MD simulations, basic residues in H1 and H6 formed salt bridges that alternated between intramolecular and intermolecular partners. In the MT-bound high-affinity conformation, H1-K3298 switched between a glutamate on β-tubulin and a conserved glutamate in CC1 (E3289) (Figures 2-11 A, 2-12 A); neither contact can be formed by H1-K3298 in the low-affinity conformation (Figure 2.8 A). H6-R3382 switched from an intramolecular interaction with a conserved glutamate in the same helix (H6-E3378) in the low-affinity unbound state to an intermolecular interaction with a cluster of glutamates on α-tubulin upon binding (Figure 2.11 B, 1-12 B); the intramolecular interaction might weaken the MTBD-MT interaction in both the low- and high-affinity conformations. The importance of the two MTBD glutamates involved in the intramolecular salt bridges had previously been recognized; substitution of CC1-E3289 and H6-E3378 with alanine increased dynein's MT-binding affinity (*18*, *44*) and reduced its ATP-stimulated release from MTs, respectively (*44*). We hypothesized that these phenotypes resulted from the competition between MT and MTBD residues in CC1 and H6 for salt bridge formation with the basic residues K3298 and R3382 in the MTBD.

To test this prediction we mutated the residues equivalent to E3289 and E3378 in CC1 and H6 of *Saccharomyces cerevisiae* dynein to either an isosteric but neutral (Q) or a basic amino acid (K) to disrupt the salt bridge (Q) or introduce an intramolecular charge repulsion (K) that may favor intermolecular interactions between H1-K3298 or H6-R3382 and acidic residues on the MT surface. Single molecule motility assays that monitored the movement of purified mutant dyneins showed significant increases in dynein's run length and small decreases in velocity that paralleled the severity of the mutation (E -> Q -> K) (Figure 2.13 A, B and Figure 2.14). Most

dramatically, the basic substitutions CC1-E3289K and H6-E3378K increased dynein's run length by five-fold and six-fold, respectively (Figure 2.13 B), and the double mutant even further (Figure 2.15). These results suggest that cytoplasmic dynein has been selected for sub-maximal processivity. The effects observed with the mutants are not due to a strengthened interaction with the unstructured carboxyl-terminal tails of tubulin (E-hooks). Although their removal decreased the run length of all constructs tested, in agreement with previous studies (*46*), the trend of increasing processivity (WT -> E3289K -> E3378K) remained (Figure 2.16).

These findings provide a molecular model for how dynein couples its affinity for MTs with the nucleotide state of the motor domain (Figure 2.13 C-E). We describe the transition from low to high affinity, but suggest that the proposed changes are reversible. During a diffusive search for its next binding site (Figure 2.13 C) an unbound MTBD is in the low-affinity conformation with its stalk in the β+ registry, H1 oriented perpendicular to the MT axis and intramolecular salt bridges at key MT-binding residues. Consistent with this, an NMR study found that an unconstrained, minimal MTBD in solution exists in the β+ registry and displays low affinity for MTs (*47*). Upon binding (Figure 2.13 D), transition to a high-affinity conformation involves a large displacement of H1, stabilized by new salt bridges with β-tubulin, and an opening of CC1 at the base of the stalk (Figure 2.13 E). The movements of H1 and CC1 likely constraint the registries that can be explored by the stalk, biasing the distribution towards the high-affinity α registry (Figure 2.13 E). Propagation of this signal to the head would elicit conformational changes that produce a movement of the linker domain, and a displacement of dynein towards the MT minus end.

Our analysis of dynamic salt bridges reveals that cytoplasmic dynein has been selected for

sub-maximal processivity. While kinesin has diversified its functional repertoire through gene duplication and divergence (*48*), cytoplasmic dynein is expressed from a single locus and may have evolved sub-optimal processivity to increase the dynamic range of its regulation. High processivity could also be detrimental when multiple dyneins and kinesins must balance their actions on a single cargo (*49*). Consistent with this idea, intraflagellar dyneins, responsible for long, unidirectional transport within cilia (*50*, *51*), contain neutral or basic residues at the equivalent of H6-E3378 (Figure 2.17), which would likely increase their processivity.

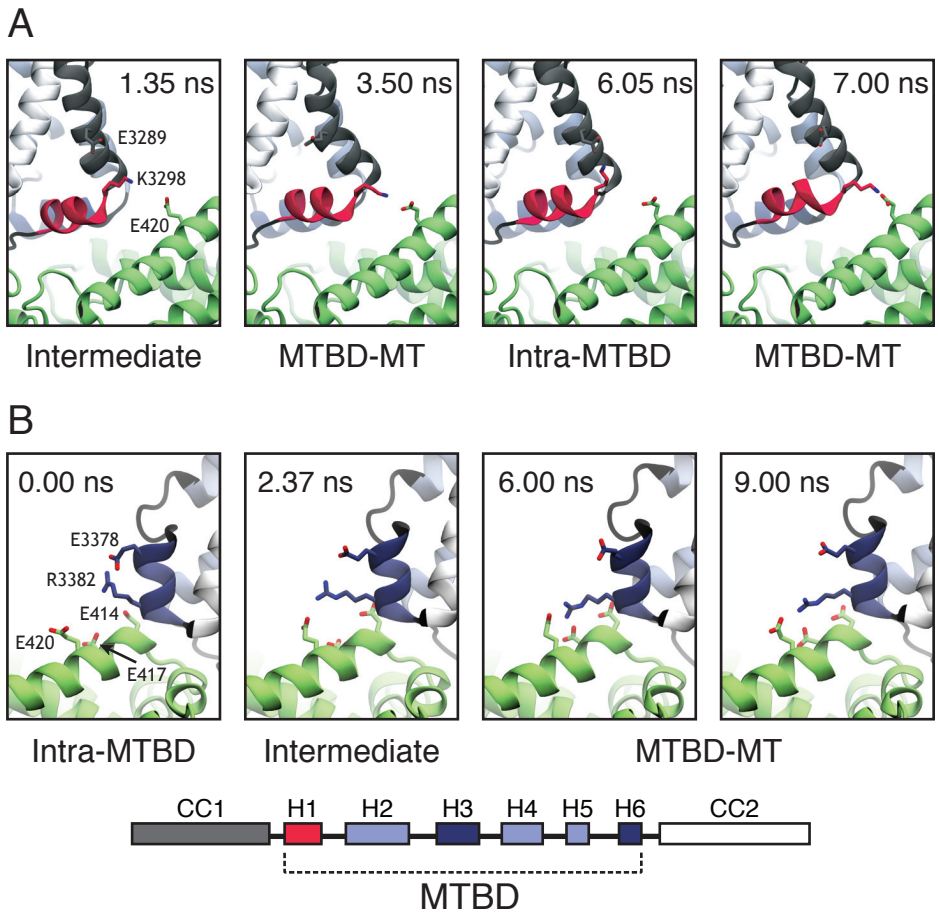


Figure 2.11. Behavior of dynamic salt bridges in the MTBD as determined by MD.
(**A**) K3298 in H1 of the MTBD alternates between an intermolecular salt bridge with E420 on β-tubulin (MTBD-MT) and an intramolecular salt bridge with E3289 on CC1 of the MTBD (intra-MTBD). (**B**) R3382 in H6 of the MTBD alternates between an intermolecular salt bridge with E414 and E420 on α-tubulin (MTBD-MT) and an intramolecular salt bridge with E3378 in H6 (intra-MTBD). Single letter amino acid code and number are indicated for Bos taurus tubulin and Mus musculus cytoplasmic dynein. Time stamps for frames from MD simulations are indicated. Intermediate refers to a position midway between MTBD-MT and intra-MTBD salt bridges.

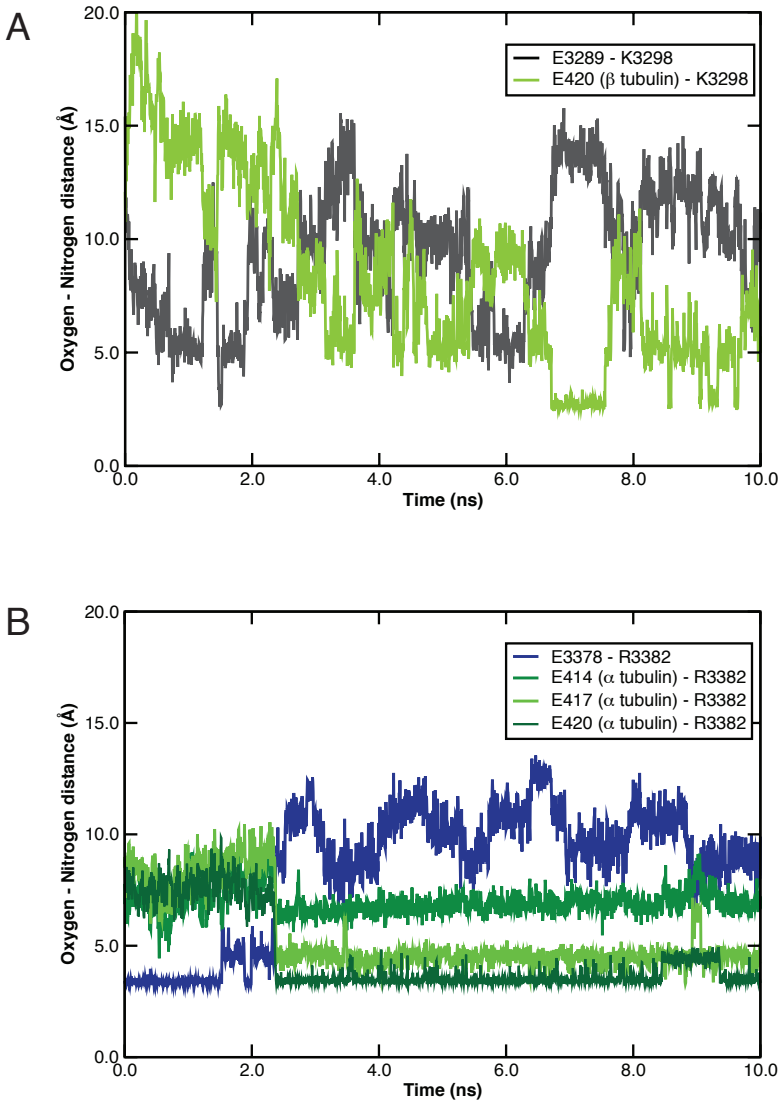


Figure 2.12. Dynamic salt bridges in H1 and H6 of the MTBD as observed by MD simulations.

(**A**) Dynamic salt bridges at H1 are formed between K3298 and either E3298 in the dynein MTBD or E420 in β-tubulin. (**B**) Dynamic salt bridges at H6 are formed between R3382 and either E3378 in the dynein MTBD or E414, E417 and E420 in α-tubulin. For both (A) and (B) the average oxygen-nitrogen distances over time for the indicated salt bridges are shown.

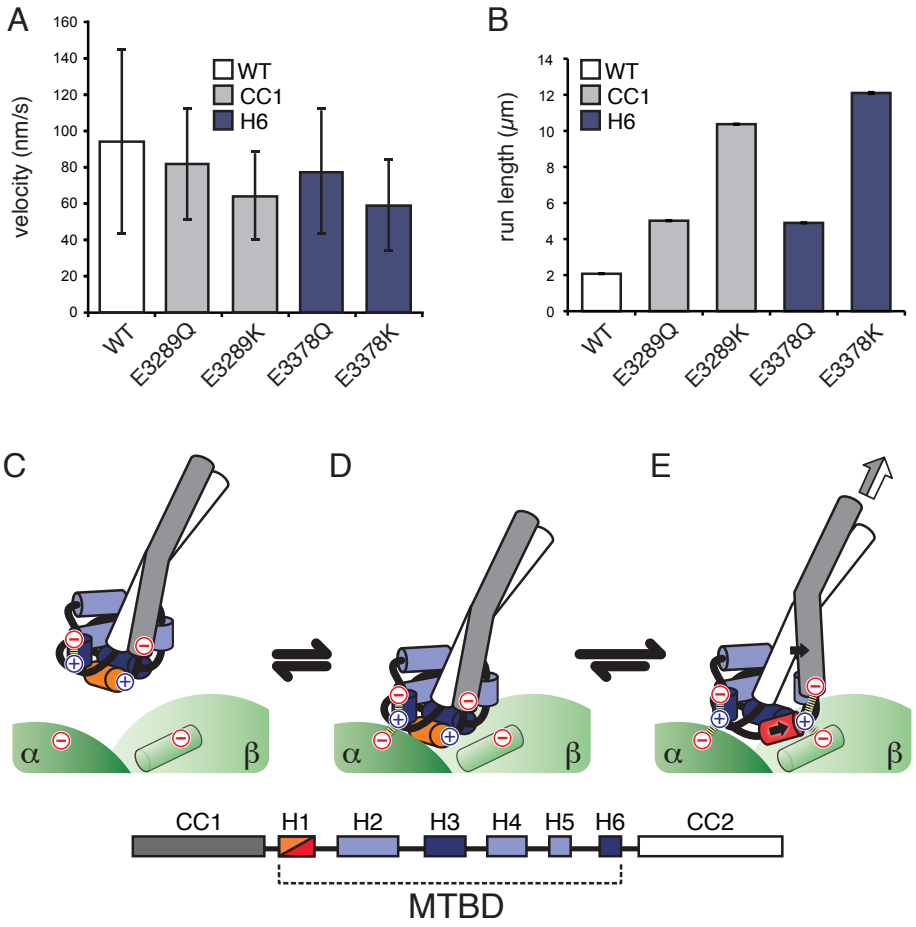


Figure 2.13. Dynamic salt bridges reduce dynein motility.
Bar graphs of (**A**) mean velocities and (**B**) characteristic run lengths of fluorescently labeled *Saccharomyces cerevisiae* dynein bearing the equivalent of the indicated *Mus musculus* mutations moving on MTs. Error bars: standard deviation, SD (A) and standard error of the mean, SE (B). Velocity and run length differences between WT and Q mutants, as well as between Q and K mutations at the same position, are statistically significant (t-test, $P < 0.01$ for velocity, and two-tailed KS-test, $P < 0.01$ for run length). The data for the double mutant (E->K at both CC1 and H6) was omitted because run lengths could only be determined under more stringent motility conditions (Figure 2.15). (**C-E**) Molecular model for the coordination of nucleotide state and MT binding by dynein (see text for details). (**C**) Unbound dynein in the low affinity conformation, H1 is colored orange. (**D**) Initial interaction with a new binding site. (**E**) Repositioning of H1 (now in red) leads to the formation of new ionic interactions with β-tubulin (green cylinder) that stabilize the high-affinity state of the MTBD. The repositioning of H1 is accompanied by a movement in CC1; both movements are indicated by solid black arrows. The conformational change in the MTBD biases the registry of the coiled-coil towards the high-affinity α state, a change that can propagate to the motor domain (white/grey arrow). Ionic interactions are indicated with dashed lines, The identities of the helices in the MTBD are indicated by the key.

Figure 2.14. Dynamic salt bridges temper dynein motility

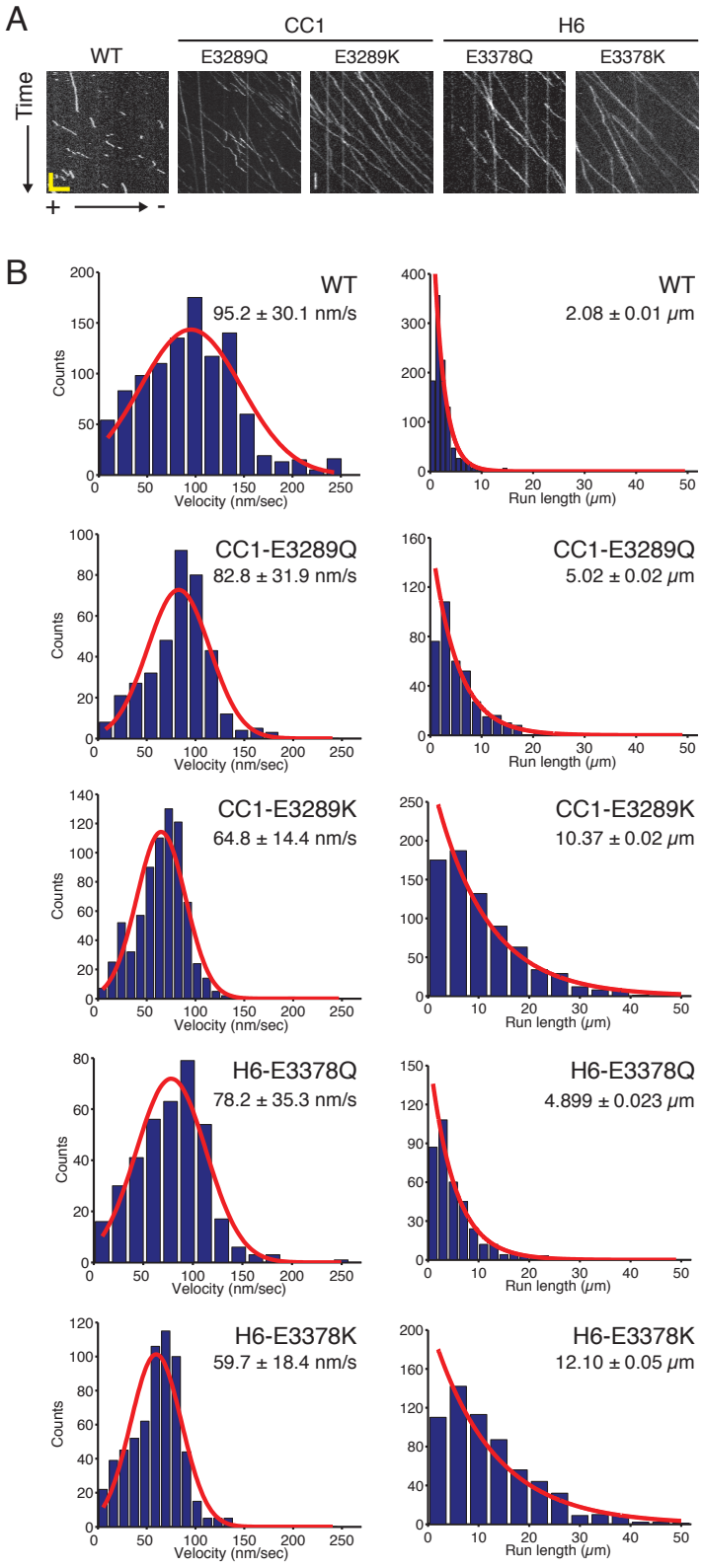


Figure 2.14. Dynamic salt bridges temper dynein motility (Continued)
Data corresponds to that reported in Figure 2.13. (**A**) Representative kymographs of fluorescently labeled dynein and dynein mutants moving along MTs. Each kymograph follows the trajectory of all dynein molecules along a stretch of a single MT. MT polarity is indicated and applies to all panels. Horizontal scale bar, 5 μm; vertical scale bar, 1 min. (**B**) Histograms of velocity and run length of WT dynein and dynein mutants from (A). All velocity data are plotted as mean +/- SD and all run length data are plotted as characteristic run length +/- SE, N>300.

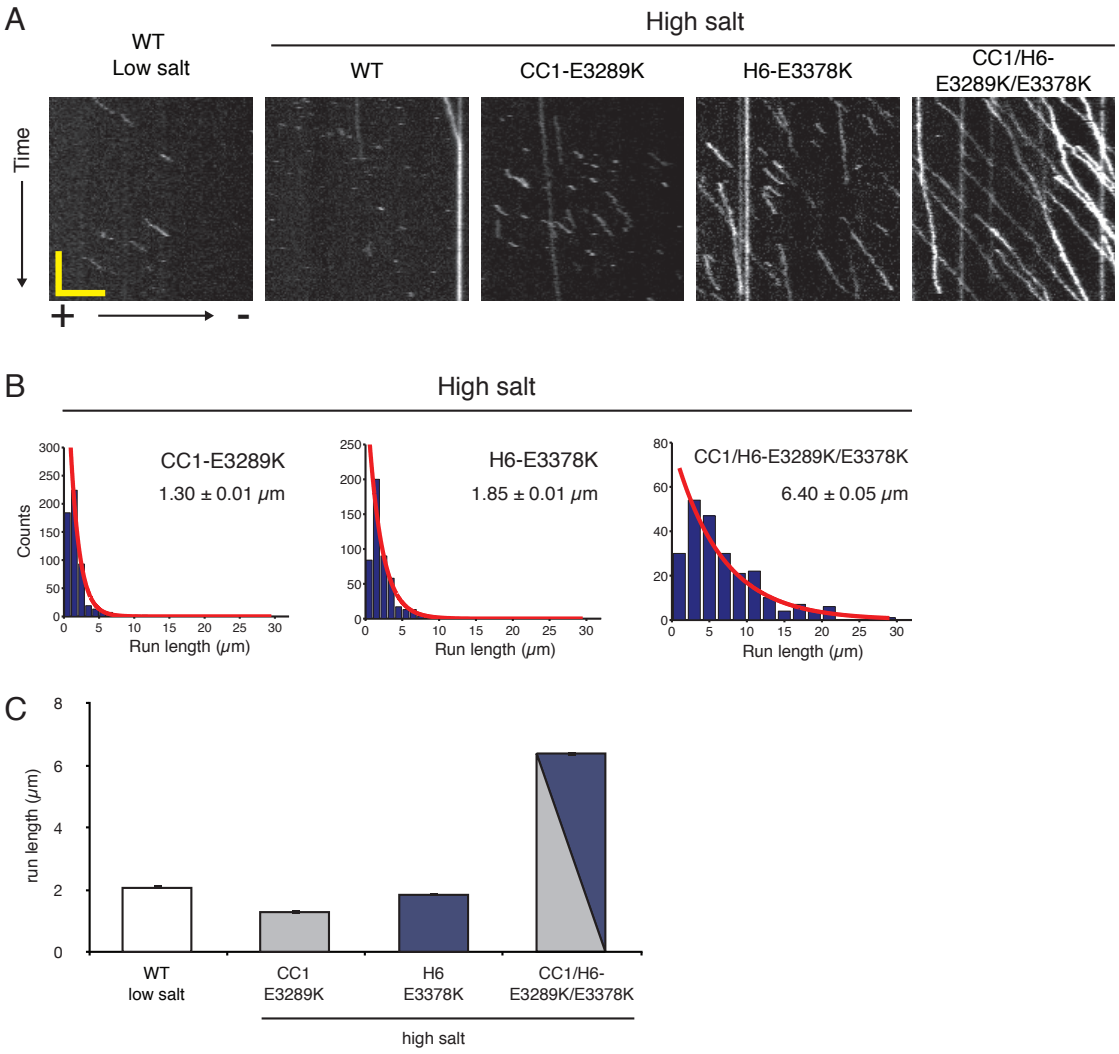


Figure 2.15. Dynamic salt bridge mutations increase dynein processivity under more stringent motility conditions.

(A) Representative kymographs of fluorescently labeled dynein moving along MTs (low salt = 80 mM total ionic strength, high salt = 130 mM total ionic strength). Note that WT dynein motility is measurable only under low salt conditions, whereas CC1-E3289K and H6-E3378K dynein mutants exhibit run lengths in high salt that are similar to WT run lengths in low salt. The combined CC1/H6-E3289K/E3378K double mutant exhibits much longer run lengths. Horizontal scale bar, 5 μm; vertical scale bar, 1 min. (B) Histograms of dynein run length corresponding to (A) are shown with their characteristic run length ± SE, N>250. (C) Quantitation of data show in (A) and (B). The differences between CC1-E3289K and H6-E3378K, and H6-E3378K and CC1/ H6-E3289K/E3378 are significant (two-tailed KS-test, $P<0.01$).

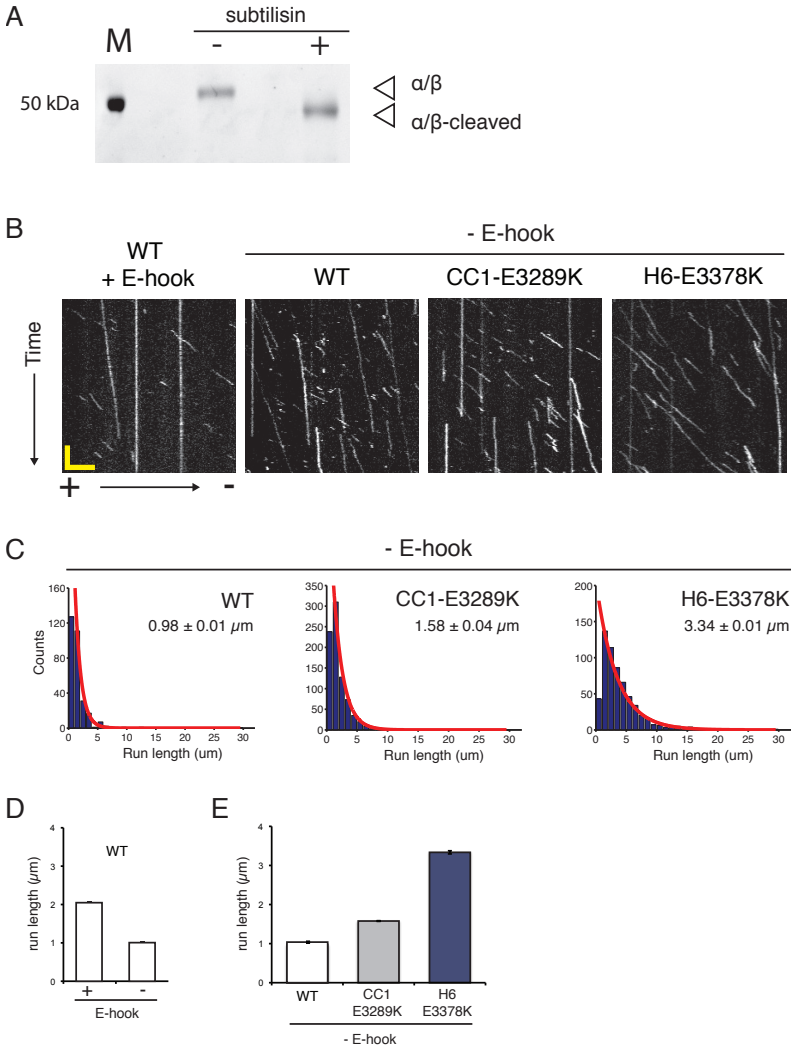


Figure 2.16. Dynamic salt bridge mutations increase dynein processivity independent of tubulin E-hooks.

(**A**) SDS-PAGE analysis of tubulin used in single molecule motility assays. Polymerized MTs were treated with subtilisin, which removes the C-terminal E-hook. Removal of the E-hook causes an increased mobility of α- and β- tubulin on the gel. (**B**) Representative kymographs of fluorescently labeled dynein moving along MTs. The presence or absence of the E-hook is indicated. Note the visibly longer runs in CC1-E3289K and H6-E3378K relative to wild type dynein (WT). Horizontal scale bar, 5 μm; vertical scale bar, 1 min. (**C**) Histograms of dynein run length corresponding to (B) are shown with their characteristic run length ± SE, N>300. (**D**) Quantitation of WT dynein run length on MTs with (+) and without (-) the E-hook. Removal of the E-hook causes a two-fold decrease in run length. The difference is statistically significant (two-tailed KS-test, $P<0.01$). (**E**) Quantitation of dynein run length on MTs without E-hooks. Note that CC1-E3289K causes a two-fold increase in run length and H6-E3378K causes a greater than three-fold increase in run length relative to WT. The increases are statiscally significant (two-tailed KS-test, $P<0.01$). Data in (D) and (E) are plotted as characteristic run length +/- SE.

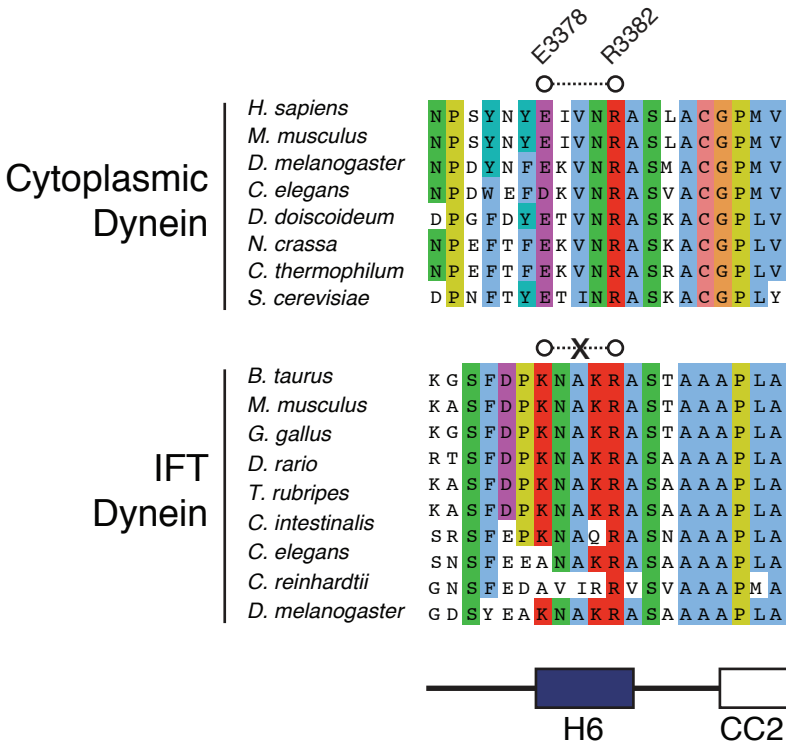


Figure 2.17. Intraflagellar transport dynein (cytoplasmic dynein 2) lacks a key intramolecular salt bridge that tunes the affinity of cytoplasmic dynein.
Alignment of a section of the MTBD from diverse cytoplasmic and intraflagellar transport (IFT) dynein sequences calculated with MAFFT (*52*) and visualized with Jalview (*45*) according to the Clustal coloring scheme. An intramolecular salt bridge, whose disruption increases cytoplasmic dynein processivity (Figure 2.13), is comprised of *Mus musculus* (*Mm*) E3378 and R3382 and is indicated by a dashed line. Note that IFT dynein lacks an acidic residue at the position equivalent to *Mm* E3378, and this position is often basic. This would prevent formation of an intramolecular salt bridge in H6, and indicates that this configuration might enhance IFT dynein processivity.

Table 2.1. Prominent interactions involving the high-affinity state of dynein's MTBD. Percentages calculated from last 10 ns of MD simulations. Interactions listed were observed for at least 1 ns along the 10 ns trajectory. Omitted were intramolecular hydrogen bonds that form the alpha helices of the dynein's MTBD. * Calculated from 15 ns of MDFF+TMD simulations.

High Affinity State Intermolecular Interactions	
MTBD-tubulin Interaction	**occupancy**
R3382-αE417	23%
R3382-αE420	79%
R3382-αG416	40%
K3299-βE431	60%
K3299-βD427	53%
R3342-βE159	51%
N3310-αG410	38%
L3385-αE415	48%
S3384-αG415	27%
A3383-αE415	49%
R3306-βE196	86%*
R3337-βD199	2%*
R3342-βN197	36%*
High Affinity State Intramolecular Interactions	
MTBD Residues	**occupancy**
K3366-D3402	52%
K3405-E3408	40%
Y3369-E3320	65%
H3301-E3304	62%
R3362-D3359	61%
R3406-D3359	65%
Q3397-S3353	38%
R3306-E3343	19%
K3427-D3423	20%
R3406-D3402	37%
K3282-E3278	11%
T3330-Q3335	16%
K3416-D3420	11%
K3264-E3267	22%
Y3400-E3284	34%
K3416-E3413	12%
T3331-E3320	11%

Table 2.2 Prominent interactions involving the low-affinity state of dynein's MTBD. Percentages calculated from last 10 ns of MD simulations. Interactions listed were observed for at least 1 ns along the 10 ns trajectory. Omitted were intramolecular hydrogen bonds that form the alpha helices of the dynein's MTBD.

Low Affinity State Intermolecular Interactions	
MTBD-tubulin Interaction	**occupancy**
A3383-αE415	45%
R3382-αG416	44%
R3382-αE417	61%
R3382-αE420	79%
K3299-βE196	27%
S3307-βR253	16%
L3385-αE415	34%
N3310-αK112	10%
Low Affinity State Intramolecular Interactions	
MTBD Residues	**occupancy**
K3366-D3402	61%
R3366-E3363	43%
R3342-E3328	87%
R3411-E3355	51%
S3353-E3356	15%
K3405-E3408	52%
Y3369-E3320	45%
H3301-E3304	37%
K3392-E3289	57%
K3316-E3320	23%
S3321-Y3375	43%
R3362-D3359	59%
K3272-E3413	54%
S3374-N3372	15%
T3331-E3320	29%
K3366-E3363	38%
K3282-D3279	29%
R3406-D3402	20%

Table 2.3. *S. cerevisiae* strains used in this study.
All yeast strains are based on the W303 background. Note that the following relationship between *Saccharomyces cervisiae* (*Sc*) and *Mus musculus* (*Mm*) dynein residues: *Sc*E3107 = *Mm*E3289 and *Sc*E3197 = *Mm*E3378.

Strain ID	Genotype	Source	Figure
RPY98	*MATa, his3-11,5; ura3-52 leu2-3,112; ade2-1, trp-1, pep4Δ::HIS5, PAC11-13Myc-TRP, pGal-ZZ-Tev-GFP-HA-Dyn1$_{331kDa}$*	*(11)*	Fig. 2. 2-7 D, E
RPY208	*MATa his3-11,5; ura3-52, leu2-3,112; ade2-1, trp-1, pep4Δ::HIS5, prb1Δ, pGAL-ZZ-TEV-GFP-3XHA-GST-DYN1$_{331kDa}$-gsDHA-kanR*	*(11)*	Fig. 2.13 A, B, Fig. 2.14, 2-15, 2-16
RPY237	*MATa, his3-11,5; ura3-52, leu2-3,112; ade2-1, trp-1, pep4**Δ**::HIS5, prb1**Δ**, pac1**Δ**::klURA3, pGAL-ZZ-TEV-GFP-3XHA-GST-DYN1$_{331kDa}$-gsDHA-kanR*	*(11)*	Fig. 2.10
RPY1217	*MATa, his3-11,5; ura3-52, leu2-3,112; ade2-1, trp-1, pep4**Δ**::HIS5, prb1**Δ**, pGAL-ZZ-TEV-GFP-3XHA-GST-DYN1$_{331kDa}$(E3107Q)-gsDHA-kanR*	this study	Fig. 2.13 A, B, Fig. 2.14
RPY1218	*MATa, his3-11,5; ura3-52, leu2-3,112; ade2-1, trp-1, pep4**Δ**::HIS5, prb1**Δ**, pGAL-ZZ-TEV-GFP-3XHA-GST-DYN1$_{331kDa}$(E3107K)-gsDHA-kanR*	this study	Fig. 2.13 A, B, Fig. 2.14, 2-15, 2-16
RPY1233	*MATa, his3-11,5; ura3-52, leu2-3,112; ade2-1, trp-1, pep4**Δ**::HIS5, prb1**Δ**, pGAL-ZZ-TEV-GFP-3XHA-GST-DYN1$_{331kDa}$(E3197Q)-gsDHA-kanR*	this study	Fig. 2.13 A, B, Fig. 2.14
RPY1235	*MATa, his3-11,5; ura3-52, leu2-3,112; ade2-1, trp-1, pep4**Δ**::HIS5, prb1**Δ**, pGAL-ZZ-TEV-GFP-3XHA-GST-DYN1$_{331kDa}$(E3197K)-gsDHA-kanR*	this study	Fig. 2.13 A, B, Fig. 2.14, 2-15, 2-16
RPY1247	*MATa, his3-11,5; ura3-52, leu2-3,112; ade2-1, trp-1, pep4**Δ**::HIS5, prb1**Δ**, pGAL-ZZ-TEV-GFP-3XHA-GST-DYN1$_{331kDa}$(E3107K, E3197K)-gsDHA-kanR*	this study	Fig. 2.15

Acknowledgements

We thank A. Carter (LMB-MRC) for reagents and advice, C. Sindelar (Yale), V. Ramey (UC Berkeley), E. Egelman (U of Virginia), and R. Sinkovits (UCSD) for sharing processing scripts and helpful advice, M. Sotomayor (Harvard) and R. Gaudet (Harvard) for advice concerning MD, J. Hogle (Harvard), M. Strauss (Harvard) and M. Wolf (OIST) for help with film and the use of a film scanner, E. Nogales (UC-Berkeley), N. Francis (Harvard), and D. Pellman (Harvard) for critically reading the manuscript, as well as all the members of the Leschziner and Reck-Peterson Labs for advice and helpful discussions. EM data was collected at the Center for Nanoscale Systems (CNS), a member of the National Nanotechnology Infrastructure Network (NNIN), which is supported by the National Science Foundation under NSF award no. ECS-0335765. CNS is part of Harvard University. MD simulations were run on the Odyssey cluster supported by the FAS Science Division Research Computing Group, Harvard University. SRP is funded by the Rita Allen Foundation, the Harvard Armenise Foundation, and a NIH New Innovator award (1 DP2 OD004268-1). AEL was funded in part by a Research Fellowship from the Alfred P. Sloan Foundation. RHL was supported in part by CONACYT and Fundacion Mexico en Harvard. The cryo-EM map was deposited at the EM Data Bank (EMDB-5439) and pseudo-atomic models at the Protein Data Bank (PDB-3J1T and -3J1U).

References

1. I. Gibbons, Dynein family of motor proteins: Present status and future questions - Gibbons - 2005 - Cell Motility and the Cytoskeleton - Wiley Online Library. *Cell Motil. Cytoskeleton* (1995).

2. P. Höök, R. Vallee, The dynein family at a glance. *J. Cell. Sci.* (2006).

3. R. Vale, The molecular motor toolbox for intracellular transport. *Cell* **112**, 467–480 (2003).

4. R. B. Vallee, G. E. Seale, J.-W. Tsai, Emerging roles for myosin II and cytoplasmic dynein in migrating neurons and growth cones. *Trends in cell biology* **19**, 347–355 (2009).

5. R. Vallee, J. Williams, D. Varma, L. Barnhart, Dynein: An ancient motor protein involved in multiple modes of transport. *J Neurobiol* **58**, 189–200 (2004).

6. S. Burgess, M. Walker, H. Sakakibara, P. Knight, K. Oiwa, Dynein structure and power stroke. *Nature* **421**, 715–718 (2003).

7. A. Roberts *et al.*, AAA+ ring and linker swing mechanism in the dynein motor. *Cell* **136**, 485–495 (2009).

8. I. R. Gibbons, B. H. Gibbons, G. Mocz, D. J. Asai, Multiple nucleotide-binding sites in the sequence of dynein β heavy chain. *Nature* **352**, 640–643 (1991).

9. T. Kon, M. Nishiura, R. Ohkura, Y. Y. Toyoshima, K. Sutoh, Distinct functions of nucleotide-binding/hydrolysis sites in the four AAA modules of cytoplasmic dynein. *Biochemistry* **43**, 11266–11274 (2004).

10. S. L. Reck-Peterson, R. D. Vale, Molecular dissection of the roles of nucleotide binding and hydrolysis in dynein's AAA domains in Saccharomyces cerevisiae. *Proceedings of the National Academy of Sciences of the United States of America* **101**, 1491–1495 (2004).

11. S. L. Reck-Peterson *et al.*, Single-molecule analysis of dynein processivity and stepping behavior. *Cell* **126**, 335–348 (2006).

12. T. Shima, T. Kon, K. Imamula, R. Ohkura, K. Sutoh, Two modes of microtubule sliding driven by cytoplasmic dynein. *Proceedings of the National Academy of Sciences* **103**, 17736 (2006).

13. A. P. Carter, C. Cho, L. Jin, R. D. Vale, Crystal structure of the dynein motor domain. *Science* **331**, 1159–1165 (2011).

14. T. Kon *et al.*, The 2.8 Å crystal structure of the dynein motor domain. *Nature* (2012), doi:

10.1038/nature10955.

15. M. P. Koonce, Identification of a Microtubule-binding Domain in a Cytoplasmic Dynein Heavy Chain. *Journal of Biological Chemistry* **272**, 19714–19718 (1997).

16. A. P. Carter *et al.*, Structure and functional role of dynein's microtubule-binding domain. *Science* **322**, 1691–1695 (2008).

17. R. B. Vallee, M. A. Gee, J. E. Heuser, An extended microtubule-binding structure within the dynein motor domain. *Nature* **390**, 636–639 (1997).

18. I. Gibbons *et al.*, The affinity of the dynein microtubule-binding domain is modulated by the conformation of its coiled-coil stalk. *Journal of Biological Chemistry* **280**, 23960–23965 (2005).

19. T. Kon *et al.*, Helix sliding in the stalk coiled coil of dynein couples ATPase and microtubule binding. *Nat Struct Mol Biol* **16**, 325–333 (2009).

20. N. Mizuno *et al.*, Dynein and kinesin share an overlapping microtubule-binding site. *EMBO J* **23**, 2459–2467 (2004).

21. S. Ludtke, P. Baldwin, ScienceDirect - Journal of Structural Biology : EMAN: Semiautomated Software for High-Resolution Single-Particle Reconstructions. *J Struct Biol* (1999).

22. V. H. Ramey, H.-W. Wang, E. Nogales, Ab initio reconstruction of helical samples with heterogeneity, disorder and coexisting symmetries. *J Struct Biol* **167**, 97–105 (2009).

23. G. M. Alushin *et al.*, The Ndc80 kinetochore complex forms oligomeric arrays along microtubules. *Nature* **467**, 805–810 (2010).

24. C. V. Sindelar, K. H. Downing, The beginning of kinesin's force-generating cycle visualized at 9-A resolution. *The Journal of Cell Biology* **177**, 377–385 (2007).

25. C. V. Sindelar, A seesaw model for intermolecular gating in the kinesin motor protein. *Biophys Rev* **3**, 85–100 (2011).

26. N. Grigorieff, FREALIGN: high-resolution refinement of single particle structures. *J Struct Biol* **157**, 117–125 (2007).

27. J. Löwe, H. Li, K. H. Downing, E. Nogales, Refined structure of alpha beta-tubulin at 3.5 A resolution. *Journal of Molecular Biology* **313**, 1045–1057 (2001).

28. J. A. Mindell, N. Grigorieff, Accurate determination of local defocus and specimen tilt in electron microscopy. *J Struct Biol* **142**, 334–347 (2003).

29. N. Grigorieff, S. C. Harrison, Near-atomic resolution reconstructions of icosahedral viruses from electron cryo-microscopy. *Current Opinion in Structural Biology* **21**, 265–273 (2011).

30. X. Zhang *et al.*, Near-atomic resolution using electron cryomicroscopy and single-particle reconstruction. *Proceedings of the National Academy of Sciences* **105**, 1867 (2008).

31. E. Egelman, A robust algorithm for the reconstruction of helical filaments using single-particle methods. *Ultramicroscopy* **85**, 225–234 (2000).

32. C. V. Sindelar, K. H. Downing, An atomic-level mechanism for activation of the kinesin molecular motors. *Proceedings of the National Academy of Sciences* **107**, 4111–4116 (2010).

33. E. Pettersen, T. Goddard, C. Huang, UCSF Chimera—a visualization system for exploratory research and analysis. *Journal of ...* (2004).

34. D. B. Wells, A. Aksimentiev, Mechanical Properties of a Complete Microtubule Revealed through Molecular Dynamics Simulation. *Biophysical Journal* **99**, 629–637 (2010).

35. L. Trabuco, E. Villa, K. Mitra, J. Frank, K. Schulten, Flexible fitting of atomic structures into electron microscopy maps using molecular dynamics. *Structure* **16**, 673–683 (2008).

36. L. G. Trabuco, E. Villa, E. Schreiner, C. B. Harrison, K. Schulten, Molecular dynamics flexible fitting: A practical guide to combine cryo-electron microscopy and X-ray crystallography. *Methods* **49**, 174–180 (2009).

37. J. Schlitter, M. Engels, P. Krüger, E. Jacoby, A. WOLLMER, Targeted molecular dynamics simulation of conformational change: application to the T↔R transition in insulin. *Molecular simulation* **10**, 291–308 (1993).

38. J. C. Phillips *et al.*, Scalable molecular dynamics with NAMD. *J Comput Chem* **26**, 1781–1802 (2005).

39. A. D. Mackerell, M. Feig, C. L. Brooks, Extending the treatment of backbone energetics in protein force fields: limitations of gas-phase quantum mechanics in reproducing protein conformational distributions in molecular dynamics simulations. *J Comput Chem* **25**, 1400–1415 (2004).

40. W. L. Jorgensen, J. Chandrasekhar, J. D. Madura, R. W. Impey, M. L. Klein, Comparison of simple potential functions for simulating liquid water. *J. Chem. Phys.* **79**, 926 (1983).

41. W. Humphrey, A. Dalke, ScienceDirect - Journal of Molecular Graphics : VMD: Visual molecular dynamics. *Journal of molecular graphics* (1996).

42. W. Qiu *et al.*, Dynein achieves processive motion using both stochastic and coordinated stepping. *Nat Struct Mol Biol* **19**, 193–200 (2012).

43. S. Uchimura, Y. Oguchi, Y. Hachikubo, S. A. I. Ishiwata, E. Muto, Key residues on microtubule responsible for activation of kinesin ATPase. *EMBO J* **29**, 1167–1175 (2010).

44. M. Koonce, I. Tikhonenko, Functional elements within the dynein microtubule-binding domain. *Molecular Biology of the Cell* **11**, 523 (2000).

45. A. M. Waterhouse, J. B. Procter, D. M. A. Martin, M. Clamp, G. J. Barton, Jalview Version 2--a multiple sequence alignment editor and analysis workbench. *J Gerontol* **25**, 1189–1191 (2009).

46. Z. Wang, M. P. Sheetz, The C-terminus of tubulin increases cytoplasmic dynein and kinesin processivity. *Biophysical Journal* **78**, 1955–1964 (2000).

47. L. McNaughton, I. Tikhonenko, N. K. Banavali, D. M. LeMaster, M. P. Koonce, A Low Affinity Ground State Conformation for the Dynein Microtubule Binding Domain. *Journal of Biological Chemistry* **285**, 15994–16002 (2010).

48. E. M. Dagenbach, A new kinesin tree. *J. Cell. Sci.* **117**, 3–7 (2004).

49. M. A. Welte, Bidirectional Transport: Matchmaking for Motors. *Current Biology* **20**, R410–R413 (2010).

50. C. Iomini, V. Babaev-Khaimov, M. Sassaroli, G. Piperno, Protein Particles in Chlamydomonas Flagella Undergo a Transport Cycle Consisting of Four Phases. *The Journal of cell ...* (2001).

51. J. A. Laib, J. A. Marin, R. A. Bloodgood, W. H. Guilford, The reciprocal coordination and mechanics of molecular motors in living cells. *Proceedings of the National Academy of Sciences* **106**, 3190–3195 (2009).

52. K. Katoh, M. C. Frith, Adding unaligned sequences into an existing alignment using MAFFT and LAST. *J Gerontol* **28**, 3144–3146 (2012).

Chapter 3

Regulatory role of the microtubule binding domain in dynein's stepping behavior

Rogelio Hernandez-Lopez, Weihong Qiu, Brian Goodman, William Bret Redwine, Samara Reck-Peterson, Andres E. Leschziner

Contributions

Rogelio Hernandez-Lopez designed the project, performed biochemistry, single molecule data collection and analysis. Weihong Qiu provided help and advice with single molecule experiments. Brian Goodman wrote and provided processing scripts for the analysis of dynein steps. The high affinity monomeric and dimeric dynein strains were created by William Bret Redwine. Andres Leschziner and Samara Reck-Peterson provided mentorship.

Abstract

Cytoplasmic dynein moves along microtubules (MTs) using the energy from ATP hydrolysis but the molecular basis of its stepping behavior remains unresolved.

Here, we have investigated how dynein's MT binding affinity affects its mechanochemical cycle and stepping behavior. Single point mutations (E3107K and E3197K) that increase dynein's affinity for MTs were found to enhance motor processivity and to reduce its stepping rate. While having negligible effect on dynein's ATPase activity, higher MT binding affinity reduces the coupling between ATP hydrolysis and forward stepping and motor's velocity decreases as a consequence. Unexpectedly, the E3107K mutant exhibits a larger step size than that of WT dynein.

Our results highlight the role of dynein's microtubule binding domain in coupling MT binding and release to the motor's activity and suggest that its MT-binding affinity has been tuned to facilitate dynein's movement and regulate dynein's motile properties such as velocity, processivity and step size.

Introduction

Cytoplasmic dynein (referred hereafter as dynein) is a highly versatile and complex cytoskeletal molecular motor. Dynein is involved in key biological processes including intracellular transport, organization of the mitotic spindle, and chromosome segregation during cell division (*1*, *2*). Dynein uses the energy from ATP hydrolysis to step along microtubules (MT) and power nearly all the transport of cargo toward MT minus-ends, located near the nuclear periphery.

Central to all of dynein's biological functions is its ability to take multiple "steps" along its track. This property, known as processivity, requires a high degree of coordination among its mechanochemical elements (Figure 3.1). The dynein holoenzyme is composed of two ~500 kDa units termed "heavy chains", each of which contains a "tail" (*1*), a "linker" (*3*, *4*), six AAA+ (adenosine triphosphatases associated with diverse cellular activities) domains forming a ring (*5*), a "stalk", and a microtubule binding domain (MTBD) (Fig 3.1). Intriguingly, the coupling of ATP hydrolysis by the motor domain with MT binding and release by the MTBD occurs across the 25 nm separation between these two domains (*6*, *7*).

Since the cell interior is crowded with organelles and macromolecules, molecular motors like dynein need to be more than just processive to conduct intracellular transport. To maneuver through and overcome obstacles, cytoskeletal transport requires motors to generate high forces.

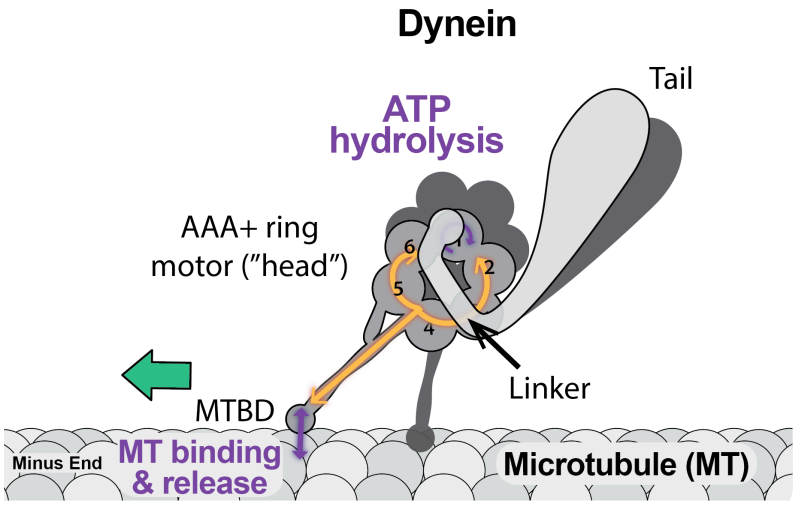


Figure 3.1. Schematic structure of a dynein dimer.
The main structural components of dynein heavy chain are indicated. Dynein couples (orange arrow) ATP hydrolysis in the head with MT-binding and release by the microtubule binding domain (MTBD), to move for long distances along MTs.

Indeed, recent data shows that dynein navigates around MT intersections better than kinesin (*8*) and that tau, a MT-associated protein, can selectively slow kinesin transport along MTs while not affecting dynein (*9*). In particular to bypass obstacles motors should be able to step sideways or backtrack.

Dynein's stepping behavior shows great variability compared with kinesin's or myosin's, some of its steps have an off-axis component and some are backwards (*10*, *11*). Dynein walks by taking a broad distribution of step sizes (*12*). Dynein's stepping is stochastic when the separation between the two motors is short--it does not alternate its motor domains and they rarely pass each other-- but becomes coordinated with the two motor domains alternating steps, when the two motors are far apart (*10*, *11*). This flexible stepping behavior may allow dynein to better navigate obstacles on MTs in a crowded cytoplasm (*10*). The molecular basis of the switch between coordinated and stochastic stepping remains elusive.

Explaining how dynein achieve its variable stepping behavior, requires to understand the activity of dynein's AAA domains and the role of its MTBD.

The activities of the AAA domains on dynein's mechanism have been investigated by single molecule (*12*, *13*), structural (*14*), biochemical (*15*) and mutagenesis studies (*16*). AAA1 is the major site of ATP hydrolysis, while ATP binding at AAA3 seems to function as a switch between motile and paused states (*14*, *17*). The roles of AAA2 and AAA4 are the least understood, but multiple studies suggest they may play some minor roles in dynein activity (*13*, *18*).

In contrast, the role of the MTBD on dynein's processivity and stepping behavior remains poorly understood. Dynein's MTBD is composed of six alpha helices (H1 - H6) (*19*, *20*)(Fig. 2.4). The loop H1-H2 and helices H3 and H6 make direct contacts with the MT (*21*) via

electrostatic interactions. H1 undergoes a large conformational rearrangement that initiates stalk sliding to communicate MT binding to the motor domain (*21*) (Chapter 2).

There are at least two models to explain dynein's variable step size (Fig. 3.2 A): (1) Dynein's MTBD searches for multiple binding sites using small steps, which are not always committed (Fig. 3.2 E)(i.e. dynein scans for binding sites using transient MT associations), resulting in short and long steps and thus a broad distribution of step sizes; (2) Dynein takes single steps of variable sizes that are always committed. The first model predicts that the step size distribution is determined by dynein's interaction with the MTs (i.e. its affinity for MTs); the second that it is determined by the motor domain. We predicted that if the former model is correct, dyneins with higher MT-binding affinity would walk with a tighter distribution of step sizes.

We sought to test this hypothesis for which we needed dynein's with high MT affinity. We previously reported two mutations in dynein's MTBD (E3107K and E3197K) that increase dynein's processivity (*21*). We identified these residues in our pseudo-atomic structure of dynein's MTBD bound to MTs (*21*) (Fig. 3.2A), which we obtained using a combination of cryo-electron microscopy and molecular dynamics simulations (see chapter 2). In *S. cerevisiae* dynein E3107 and E3197 are two highly conserved negative residues that form intramolecular salt bridges within the MTBD. These salt bridges compete with intermolecular salt bridges between the MTBD and tubulin.

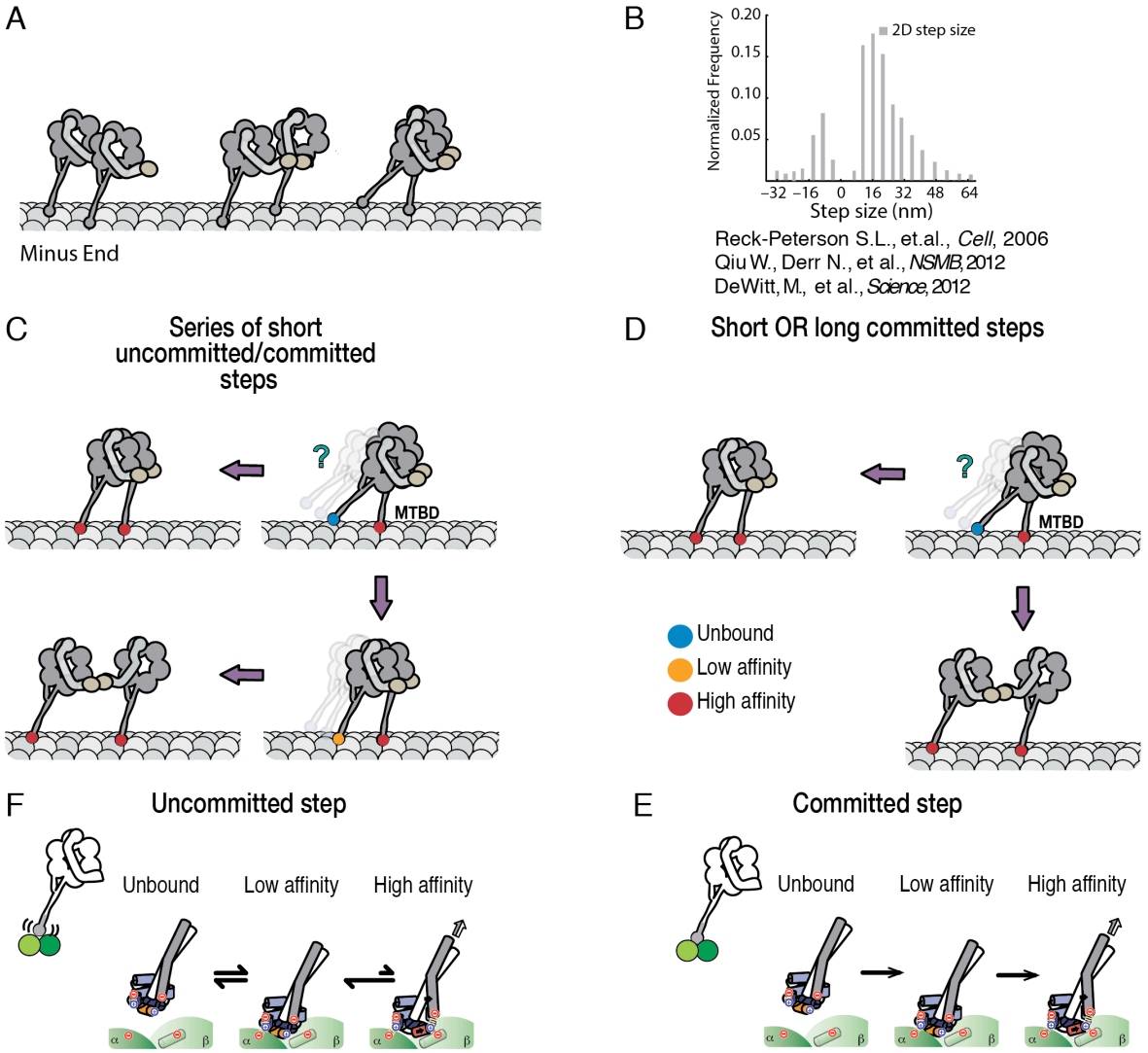


Figure 3.2. Two possible models to explain dynein's variable step size distribution
(A) Schematic of dimeric cytoplasmic dynein walking along a microtubule. For simplicity a mini-dimer taking short and long steps is depicted. **(B)** Previous studies (*10-12*) have stablished the variability of dynein's stepping behavior. Dynein can take long and short steps in the forward (MT-minus end) and backward directions (MT-plus end). Dynein may achieve its variable step size by **(C)** a diffusive search by the MTBD combining series of short, some of them committed and other uncommitted, steps or **(D)** an unknown mechanism that involves committed steps of different sizes (see below) by the microtubule binding domain. **(E)** An uncommitted step involves an equilibrium between the low and high affinity MTBD conformations that biases dynein towards the unbound state rather than fully interacting with the MT. **(F)** A committed step is such that the transition between the unbound, low affinity and high affinity MTBD's conformations is unidirectional.

Mutating the negative residues (glutamate) to positive ones (lysine) dramatically increased dynein's processivity (*21*) suggesting that the mutations increased dynein's affinity for the MT. Therefore these mutants were good candidates for this experiment.

To investigate how MT binding affinity affects dynein's stepping mechanism, we first characterized the mechanochemistry of the hyper-processive dyneins (E3107K, E3107K and E3107K-E3197K) and then performed single molecule analysis of their stepping behavior. We found that the enhanced processivity of the mutants is likely the result of an increased MT binding affinity. We show that an increased MT affinity reduces dynein's stepping frequency and impairs the coupling between ATP hydrolysis and forward motion. Our results show that the MT binding-affinity of dynein's MTBD has a role regulating dynein's mechanochemical cycle, velocity and processivity. Unexpectedly, we also show that different MT-binding sites may have different roles in modulating dynein's stepping behavior, specifically, dynein's step size.

Materials and Methods

S. cerevisiae Strain Construction

The yeast strains used in this study (Table 3.3) are based on the strains expressing monomeric (RPY 1302) or the truncated, GST-dimerized ("minidimer") (RPY308), dynein that have been previously described (*12*). Deletions or modifications of the parental strains were done using PCR-based methods as previously described (*22*), using the URA3/5FOA 'pop-in/pop-out method' (*23*). Shortly, mutations in the MTBD sequence were carried out by sequential URA3 replacement of the MTBD region, transformation with MTBD sequence bearing the desired mutations, and 5FOA selection. Transformations were done using the standard lithium acetate method. All mutations were sequence verified.

Protein expression and purification

Dynein constructs for single molecule assays were expressed, purified and labeled as described previously (*12*). For the ATPase assays the expression and purification was modified as proposed by Redwine (*24*) to obtain large quantities of purified protein. Starter cultures (10 mL) of *S. cerevisiae* were grown overnight with shaking in YPD broth at 30 °C and transferred to medium size cultures (100 mL) the next morning. The cells were incubated for the entire day at 30 °C and transferred at night to a larger culture (2L) of 2X YP with 1% glucose. The cultures were kept at 30 °C until a constant optical density was reached. Protein expression was induced with a 40 % solution of galactose to a final concentration of 2% and the cells were further incubated at 30 °C overnight. The next morning, the cells were harvested by centrifugation and the pellet was frozen using liquid nitrogen.

The frozen cells were lysed using a coffee grinder and the powder was resuspended in the appropriate amount of 4X lysis buffer and quickly thawed in a 37 °C water bath. The resulting lysate was centrifuged at 40,000 x g in a Ti45 rotor (Beckman) for 2 hours at 4° C. The cleared lysate was incubated with a IgG Sepharose Fast Flow resin for 2 hrs. The resin was then washed with lysis buffer and the bound protein was then eluted with a TEV protease at 4 ° C overnight. Large aggregates were removed by centrifugation and the protein was concentrated using an Ultracell 100K MWCO concentrating column. The protein concentration of each construct was determined using gel electrophoresis, Sypro-red (Invitrogen) staining and Actin (Cytoskeleton, Inc) standards.

Tubulin polymerization for ATPase assays

Purified tubulin, from cow brain, was stored in BRB80 (80 mM PIPES-KOH, pH 6.8; 1 mM MgCl2, 1 mM EGTA, 1 mM DTT) to a concentration of 17.4 mg/mL. Tubulin was then polymerized with a stepwise addition of taxol (Sigma Aldrich) as follows: 20 µL aliquots of tubulin stock were thawed quickly and placed on ice. To each aliquot, 10 µL of BRB80 supplemented with 3 mM GTP were added and the mixture was transferred to a 37 °C water bath. After 15, 30, and 45 minutes, additions of 0.5, 0.5, and 1.0 µL of 2 mM taxol were added by gentle swirling. The mixture was then incubated for an additional 1 h at 37 °C. Free tubulin was removed using a 40% glycerol cushion (1X BRB80, 40% glycerol, 20 uM Taxol, 1 mM DTT) by centrifugation at 50,000 rpm in a TLA 100 rotor (Bekman) for 20 min at room temperature. The microtubules were resuspended in assay buffer (30 mM HEPES (pH 7.2), 50 mM potassium acetate, 2 mM magnesium acetate, 1 mM EGTA, 1 mM DTT, and 10 mM taxol). The tubulin concentration in the MTs was determined by denaturing (6M guanidine HCl) a small aliquot and measuring the OD_{280} using an extinction coefficient of 1.15 $(mg/mL)^{-1}$.

Measurements of ATPase activity

The basal and microtubule-stimulated ATPase activities of the hyperprocessive dynein mutants (E3107K, E3197K and double mutant) were measured using an EnzChek phosphatase kit (Molecular Probes, Thermo Fisher Scientific Inc.) as previously described (*12*, *13*). The final reactions (150 µL) were aliquoted in a UV transparent plate (Costar 3635) and consisted of 10 nM dynein (monomeric constructs), 0 - 15 uM taxol-stabilized microtubules, 2 mM Mg-ATP, 200 mM MESG (2-amino-6-mercapto-7-methyl-purine riboside), 1 U/ml purine nucleoside

phosphorylase, and assay buffer (30 mM HEPES (pH 7.2), 50 mM potassium acetate, 2 mM magnesium acetate, 1 mM EGTA, 1 mM DTT, and 10 mM taxol). A SpectraMax384 plate reader (Molecular Devices) was used to monitor the OD_{360} every 12 s for 10 min. To obtain the microtubule affinity constant $K_{m(MT)}$ and basal ATPase activities k_b, data were fit using MATLAB as described previously (*25*).

Single molecule microscopy

High precision analysis of dynein stepping behavior was carried out as previously described (*10*, *12*). GST mini-dimer dyneins were labeled with 655-Qdots (Invitrogen) via a C-terminal Halo-biotin tag and imaged on sea urchin axonemes using motility chambers under Total Internal Reflection Fluorescence (TIRF) illumination. The dynein imaging buffer consisted of 30 mM HEPES (pH 7.2), 50 mM potassium acetate, 2 mM magnesium acetate, 1 mM EGTA, 10% glycerol, 1 mM DTT, 1.05 mg/ml casein, 5 μM Mg-ATP, an oxygen scavenger system (glucose oxidase catalase and glucose 0.2%) and an ATP regeneration system (10 mg/mL piruvate kinase and 10 mM phosphoenolpyruvate). 20 μL of axonemes diluted in BRB12 (12 mM PIPES pH 6.8, 2 mM magnesium chloride and 1 mM EGTA) were incubated in the motility chamber for 2 minutes to allow them to adhere to the coverslip. The unbound axonemes were washed with 5 chamber volumes (100 μL) of BRB12 and then 1 chamber volume of dynein buffer (30 mM HEPES (pH 7.2), 50 mM potassium acetate, 2 mM magnesium acetate, 1 mM EGTA, 10% glycerol, 1 mM DTT, 1.00 mg/ml casein). The chamber was then incubated with 20 μL of biotinylated dynein molecules in the absence of ATP for 2 minutes, washed with 5 chamber volumes of dynein motility buffer to remove unbound dynein molecules and incubated with 50

nM 655 Qdot streptavidin (Invitrogen) for 2 minutes. Unbound Qdots were washed with 7 chamber volumes of dynein motility buffer. To initiate dynein's motility, dynein buffer supplemented with ATP, the oxygen scavenger, and the ATP regeneration system were added to the chamber and the chamber was then sealed with vacuum grease. The sample was imaged with a 405 nm laser at 30 mW on a Zeiss Elyra PS.1 microscope with a 100X 1.49 N.A. oil immersion TIRF objective (Carl Zeiss GmbH, Germany), 1.6x optovar, and an Andor EM-CCD camera. Images were stream recorded with a 100 ms or 50 ms exposure time for 1 minute using the Zen Black (Zeiss) software.

Stepping analysis

Fluorescent spots in each movie frame were identified and then fitted with a 2-D Gaussian to localize their position (*26*). Steps in 1-D and 2-D were determined by a custom program written in MATLAB (Mathworks) as previously described (*10*). Briefly, all valid dwells included in the analysis were at least three frames long. A step was counted only if the dwells before and after contained at least three frames. The resulting stepping traces (x-y coordinates of a Q-dot position) and the corresponding fluorescence intensity profiles were plotted. The traces were visually inspected and were discarded according to the following criteria: a) if the position dwell clusters were not clearly defined (high standard deviation from the mean), b) if the fluorescent intensity was too low to yield high precision localization, c) if the Qdot blinked and disappeared from the field of view for multiple frames that could lead to missed steps. The remaining traces were analyzed with a custom MATLAB 2D-step finding algorithm. To determine the step size and dwell time (the length of pausing between steps), the program implements a Chung-Kennedt edge-detecting algorithm designed for analyzing time series with noise. Steps were counted

when they had a component of either ≥ 4 nm along the principal axis of motion (on-axis step), ≥ 5 nm off-axis (the separation between two adjacent tubulin protofilament), or both.

Results

To test whether our MTBD super processive mutants (*21*) (E3107K and E3197K) have higher MT binding-affinity than WT dynein, we measured their basal and microtubule-stimulated ATPase activities. We performed these assays using monomeric rather than dimeric constructs to eliminate other effects (e.g. coordination between the two heads) that may difficult the interpretation of our results. We previously engineered a monomeric dynein construct that contains a 331 kDa minimal yeast motor domain (*27*). This minimal construct (referred to as "wild-type dynein" in this experiment) lacks the dimerization domain and therefore does not bind the dynein light or intermediate chains. The parental yeast strain (RPY1302) (*27*) does not contain Pac1, the Lis1 homologue in yeast, which has been shown to bind dynein's motor domain and increase its affinity for MTs (*27*, *28*). Point mutations changing the conserved glutamate residues to lysines (E3107K, E319K) were introduced into the MTBD (Figure 3.2 A) as single or double mutations. Recombinant dyneins with and without the MTBD mutations were purified from *S. cerevisiae* with a N-terminal affinity tag (Figure 3.2 B). We measured their basal and microtubule-stimulated ATPase activities (Figure 3.2 C) at saturating concentration of ATP (2 mM). The MT concentration at the half maximal ATPase activity, $K_{m(MT)}$, and maximal ATPase activity, k_{cat}, values (Table 3.1) were obtained from fitting each data set to the equation (*18*)

$$k_{obs} = (k_{cat} - k_b)\frac{[tubulin]}{K_{m(MT)} + [tubulin]} + k_b$$

where k_{obs} and k_b are observed and basal ATPase rates, respectively.

In agreement with the striking increase in processivity seen in single molecules assays (see chapter 2 (*21*) Fig. 2.13 B), the single mutants E3107K and E3197K show a 6- to 7-fold higher binding affinity for MTs, $K_{m,MT}$, when compared to wild-type dynein (Table 3.1). Interestingly, the double mutant displays a ~25-fold increase in MT-binding affinity and nearly a 2-fold reduction of the maximum MT-stimulated ATPase rate (Table 3.1). The maximal ATPase activity, k_{cat}, of E3107K, E3197K and wild type were comparable, suggesting that higher MT binding affinity does not interfere with the motor's ability to hydrolyze ATP. The increase in affinity and reduction of ATPase activity of the double mutant (E3107K-E3197K) seems to be the result of a cooperative effect of the two mutations. We find that this effect is also present in the context of a dynein dimer.

We next determined whether higher affinity for MTs had an effect on dynein's stepping rate and the step size distribution of individual molecules. We purified and labeled dynein with a single 655 Q-dot (via a C-terminal HaloTag) and observed GST-dynein homodimers moving along axonemes by total internal reflection microscopy (Fig. 3.3 A). In GST-based dimerization, a glutathione S-transferase domain (GST) replaces dynein's tail and forms a stable dimer**.** GST–dynein (referred to as "wild-type dynein" in this experiment) has *in vitro* (velocity and step size) properties similar to those of native yeast dynein (*10-12*, *29*), suggesting that the native dimerization interface is not required for motility and does not affect the stepping behavior.

Figure 3.3 Single point mutations in dynein's microtubule binding domain (MTBD) increase its affinity for microtubules.

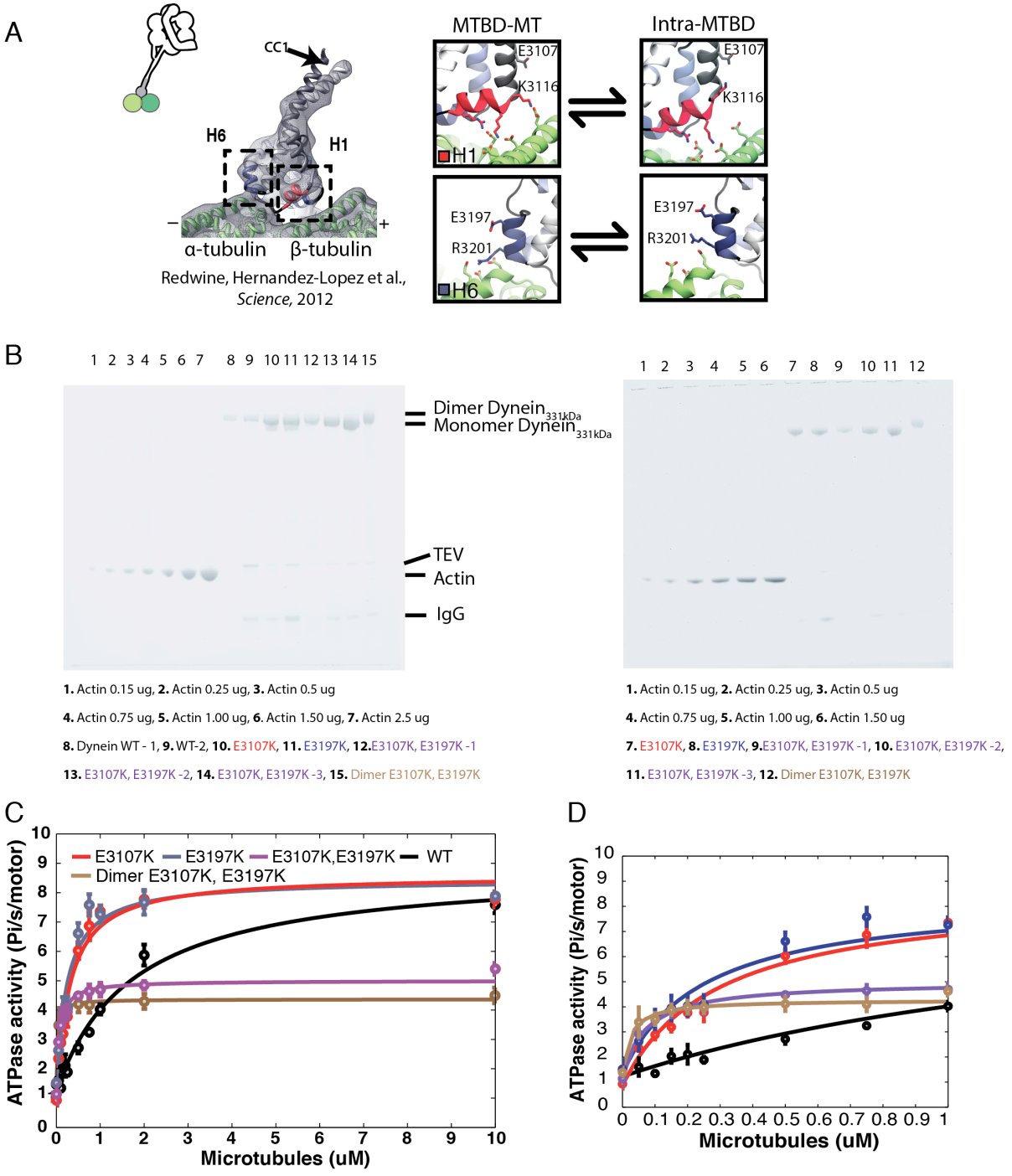


Figure 3.3 Single point mutations in dynein's microtubule binding domain (MTBD) increase its affinity for microtubules (Continued)
(A) Left: Cryo-EM structure of dynein's MTBD bound to microtubules (*21*). A pseudoatomic model of the high-affinity MTBD-MT complex is displayed as ribbons within the cryo-EM density. H1 and H6, two of the main helices that interact with the MT are highlighted. **Right:** Dynamic saltbridges in the MTBD-MT interaction showing the residues E3107 and E3197 involved in tempering the interaction of dynein with the α/ β - tubulin dimer as seen by molecular dynamics simulations (See Figure 2.11). The inset shows dynein's MTBD in relation with the rest of the motor . The E3107 and E3197 residues were mutated to positively charged residues (E3107K, E3197K) in a background of a minimal *S. cerevisiae* cytoplasmic dynein monomer (RPY1302) or mini-dimer (RPY208). In this figure, the monomeric construct RPY1302 is referred to as "wild type dynein".
(B) Representative sypro-stained NUPAGE gels of recombinant cytoplasmic dynein constructs purified from S. cerevisiae. Actin standards were loaded onto the gel to quantify the protein concentration. All purified constructs show minor amounts of IgG and TEV from the purification process. In some cases more than one prep was carried out to obtain enough protein for the ATPase assays. (C) Microtubule stimulated ATPase activity of wild type and dynein MTBD mutants at 2 mM ATP. (D) Detailed view of the microtubule-stimulated ATPase activity at low microtubule concentrations. $K_{m,(MT)}$ values for wild type (WT), E3107K, E3197K, both and in the dimer are 1.74, 0.29, 0.25, 0.071 and 0.025 μM. Each dot represent the average value and the error bars the standard error from the mean from three measurements (See Table 3.1).

Table 3.1. ATPase activity of Dynein's MTBD mutants

	Basal ATPase	MT-stimulated ATPase		
	k_b (s^{-1})	$K_{m\ (MT)}$(μM)	k_{cat} (s^{-1})	R^2
WT	1.22 ± 0.40	1.74 ± 0.78	8.89 ± 1.16	0.981
E3107K	0.88 ± 0.87	0.29 ± 0.15	8.59 ± 0.87	0.973
E3197K	1.38 ± 0.97	0.25 ± 0.14	8.45 ± 0.76	0.962
E3107K, E3197K	1.19 ± 0.41	0.071 ± 0.03	5.00 ± 0.21	0.978
Dimer-E3107K, E3197K	1.39 ± 0.46	0.025 ± 0.02	4.28 ± 0.20	0.952

At 5 μM ATP, all dynein molecules (wild-type, E3107K, E3197K and E3107K/E3197 mutants) showed processive motility (Fig. 3.4 C,D and Fig. 3.5). We tracked the position of individual dynein molecules with nanometer precision (Fig. 3.3B) by fitting a 2D gaussian to the point spread function of the Qdot and utilized a 2D step finding algorithm to determine the average position and step size of individual molecules in two dimensions.

The stepping rate and its underlying kinetic mechanism can be characterized by analyzing the distribution of dwell times separating step transitions (*30-32*). Consistent with previous reports (*11*), our analysis of dwell times (i.e. the time between steps) of the WT dynein at low ATP concentration (5 μM) revealed a distribution that can be best fit to a convolution of two exponential functions with different decay constants (Fig. 3.6 A, Fig.3.8) (*11*). The fast rate k_1 = 14.4 s^{-1}, is a composite of multiple rates along dynein's mechanochemical cycle but it may be dominated by the ATP hydrolysis event, whereas the slow rate k_2= 1.5 s^{-1} is the rate limiting step, most likely corresponding to ATP binding under this conditions (*11*). These values are in very good agreement with the ones previously measured at 12 μM ATP (k_1 = 14.1 s^{-1} , k_2= 2.1 s^{-1}) (*11*).

We next analyzed the stepping rate of the mutants. E3107K and E3197K showed a larger frequency of long dwell times compared to that of the wild-type dynein (Fig. 3.6 A). The double mutant exhibited longer dwell times. These results show that an increased affinity for MTs has a direct effect on the stepping rate of individual molecules.

Figure 3.4 Stepping behavior of head-labeled GST-Dyn$_{331KDa}$ WT and MTBD high affinity mutants.

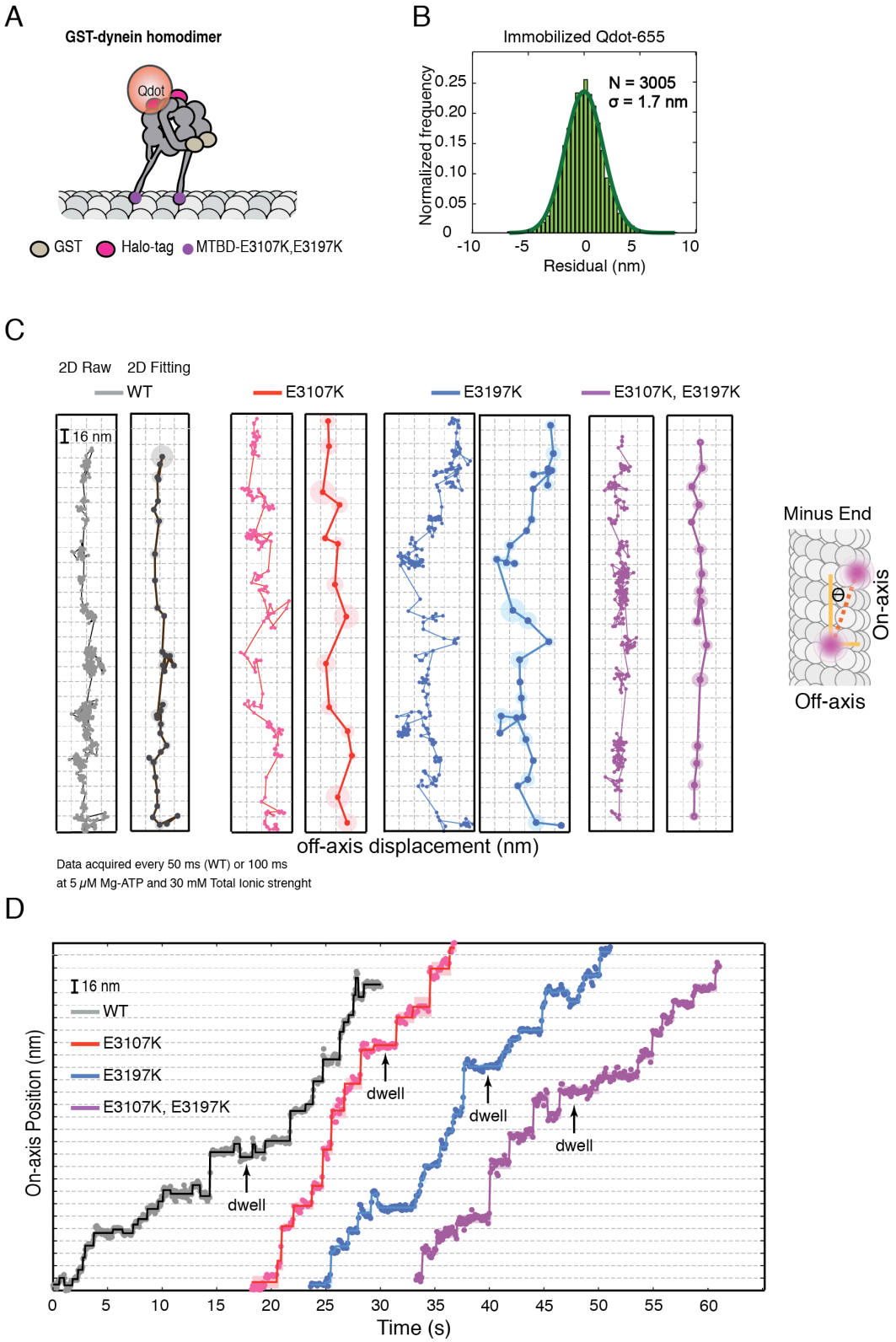


Figure 3.4 Stepping behavior of head-labeled GST-Dynein331$_{kDa}$ wild-type and MTBD mutants (Continued)

(A) Schematics of a GST-dimerized dynein (*12*) bearing the E3107K, E3197K mutations in its MTBD. The construct is labeled with a streptavidin-coated 655-Quantum dot via a halo-biotin tag located in its C-terminus for high-precision stepping experiments. **(B)** To determine the localization precision of our tracking procedure, 655-Qdot were immobilized on a coverslip and imaged using the same laser intensity and exposure time as the experimental conditions used to image dynein. The position of each Quantum dot was determined by fitting a 2D gaussian to the point spread function of each fluorophore. The histogram shows the length distribution between the raw x-y position and the average position. The standard deviation (**σ**) of this distribution indicates the localization precision of our tracking procedure. **(C)** Representative two-dimensional traces of dynein MTBD mutants. In this figure the GST-mini dimer RPY208 construct (*12*) (Table 3.3) is referred to as "wild-type dynein".

The left panel of each construct shows the raw 2D stepping trace (dots connected with colored lines). The right panel show the average position and steps as determined by the 2D step finding algorithm. The lighter colored circles represent the standard deviation of the average position at each step. The grid lines have a spacing of 16 nm along each direction. **(D)** One-dimensional projection along the movement direction (On-axis) of the 2D traces shown in (C). Colored dots are the raw positions, lines represent the steps determined by the 2D step finder and the light colored rectangles indicate the standard deviation of each step along the projection axis. All stepping experiments were carried out at 5 μM Mg-ATP and 30 mM total ionic concentration.

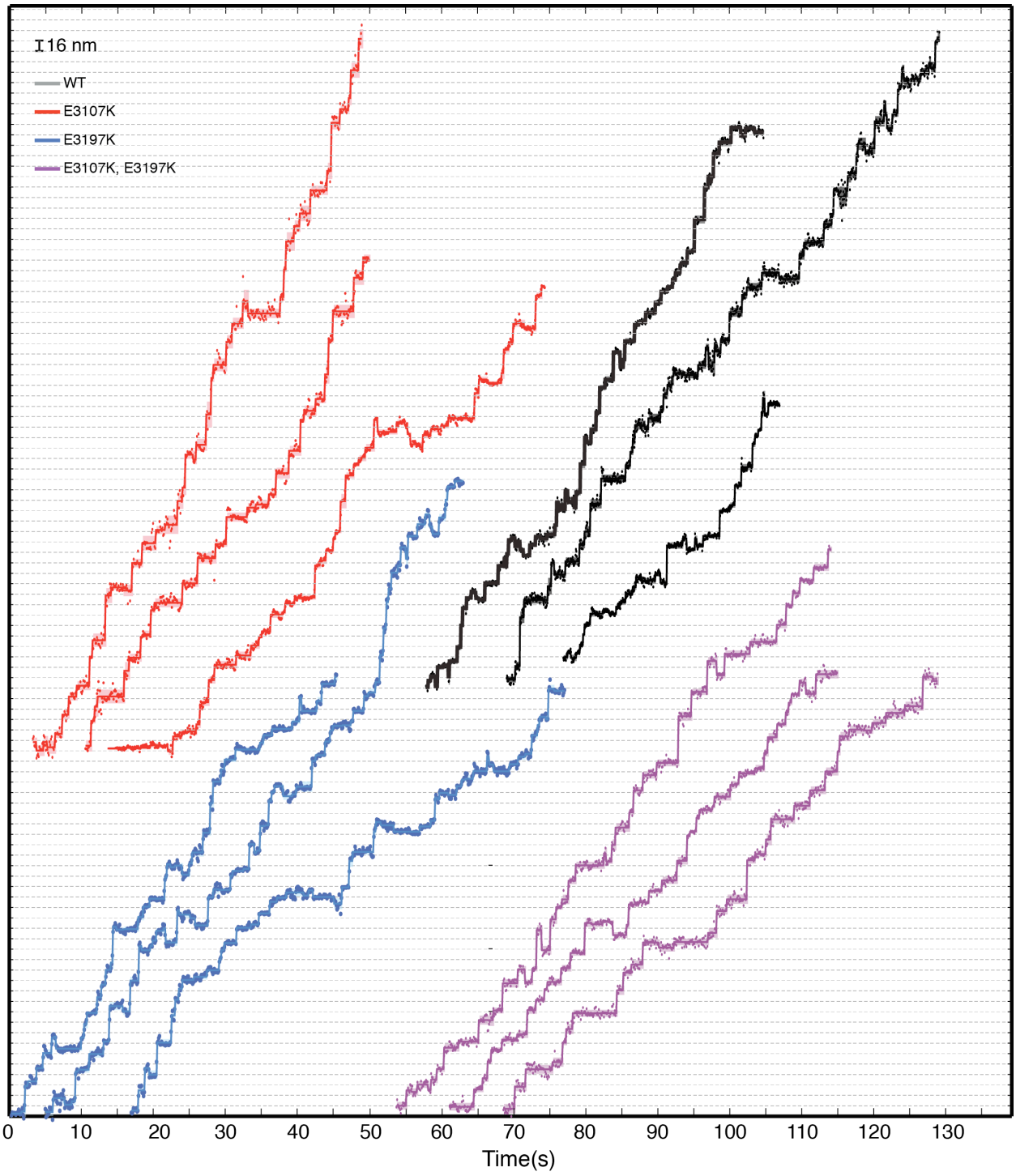


Figure 3.5 On-axis dynein stepping of head-labeled GST-Dynein331$_{kDa}$ wild-type and MTBD high affinity mutants.

More examples of on-axis traces of 655-labeled dynein WT and MTBD mutants. See figure 3.4 for details. The raw data is shown as dots while the lines were generated by the 2D step finder algorithm (see methods section), lighter colored rectangles represent the standard deviation from the average position at each step.

Figure 3.6 An increased affinity for MTs reduces dynein's stepping rate.

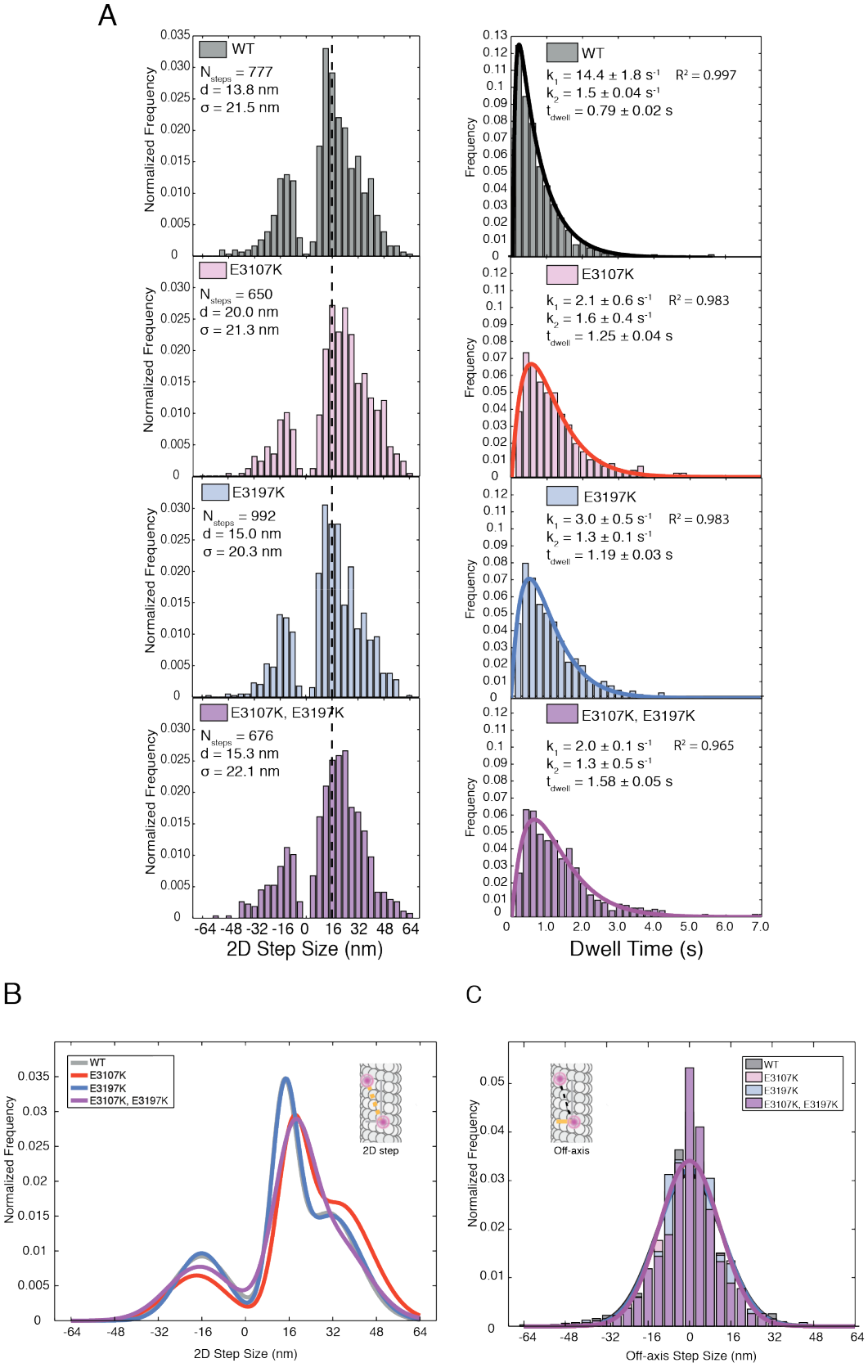


Figure 3.6 An increased affinity for MTs reduces dynein's stepping rate (Continued)
(A) Histograms of two-dimensional step size and dwell-times for WT and high affinity MTBD dynein mutants. The number of steps considered for the analysis, the average step size and the standard deviation of each population are indicated in each plot. The dwell time histograms fit to a convolution of two exponential functions with unequal decay constants. The stepping rate constants are indicated in each plot (Table 3.2). **(B)** Fit of the 2D step size distributions shown in **(A)**. Notice that the E3197K mutant has the same step-size distribution than WT with a peak centered at ~16 nm, whereas the E3107K shows its peak at a larger step size. **(C)** The Off-axis distribution of step sizes and fit show a similar behavior for the WT and MTBD mutants suggesting that the large steps observed in the E3107K mutant are due to an increase of the steps On-axis component.

Table 3.2 Stepping rate constants of WT and high-affinity MTBD mutants

	k_1 (s^{-1})	k_2 (s^{-1})	R^2
WT	14.4 ± 1.8	1.5 ± 0.04	0.997
E3107K	2.1 ±0.6	1.6±0.4	0.983
E3197K	3.0±0.5	1.3±0.1	0.983
E3107K,E3197K	2.0±0.1	1.3±0.5	0.965

The dwell time histograms of head-labeled single and double MTBD mutant dyneins are best described by a convolution of two unequal exponential rate constants (Table 3.2). In all three cases both rates are comparable: E3107K (k_1 = 2.1 s^{-1} , k_2= 1.6 s^{-1}), E3197K (k_1 = 3.0 s^{-1} , k_2= 1.3 s^{-1}) and the double mutant (k_1 = 2.0 s^{-1} , k_2= 1.3 s^{-1}), suggesting that ATP binding is no longer the only rate-limiting step as in the case of the WT dynein.

Based on our two-dimensional step size analysis, WT dynein labeled with a single Qdot on the motor domain has an average step size of 13.8 nm (Fig. 3.6 A). Similarly, the E3197K mutant, showed a step size distribution with an average step size of 15 nm (two-sample Kolmogorov-Smirnov (KS) test, alpha level of 1%, p-value=0.74). In contrast, the E3107K mutant has an average step size of ~20 nm (Fig. 3.6 B), significantly different from that of WT dynein (KS test, alpha level of 1%, p-value=$4x10^{-9}$) or that of the E3197K mutant (KS test, alpha level of 1%, p-value=$7x10^{-9}$). Intriguingly, the double mutant E3107K-E3197K displayed an average step size of 15.3 nm, similar to WT (KS test, p-value=0.016, alpha level of 1%).

As reported previously by Qiu *et al.* (*10*), we found for all four dynein constructs in this study, most dynein steps were forward steps (WT = 76%, E3107K 82%, E3197K 78% and E3107K, E3197K 78%). Analysis of the off axis component of dynein steps revealed a similar behavior for the single and double mutants, when compared to that of WT dynein (Fig. 3.6 C). These results suggest that the increased population of long steps in the E3107K mutant is due to a larger on-axis component of their steps. To further characterize the apparent difference in dynein's step size, we analyzed in more detail the on-axis step size distributions for both the WT dynein and the E3107K mutant (Fig. 3.7 A).

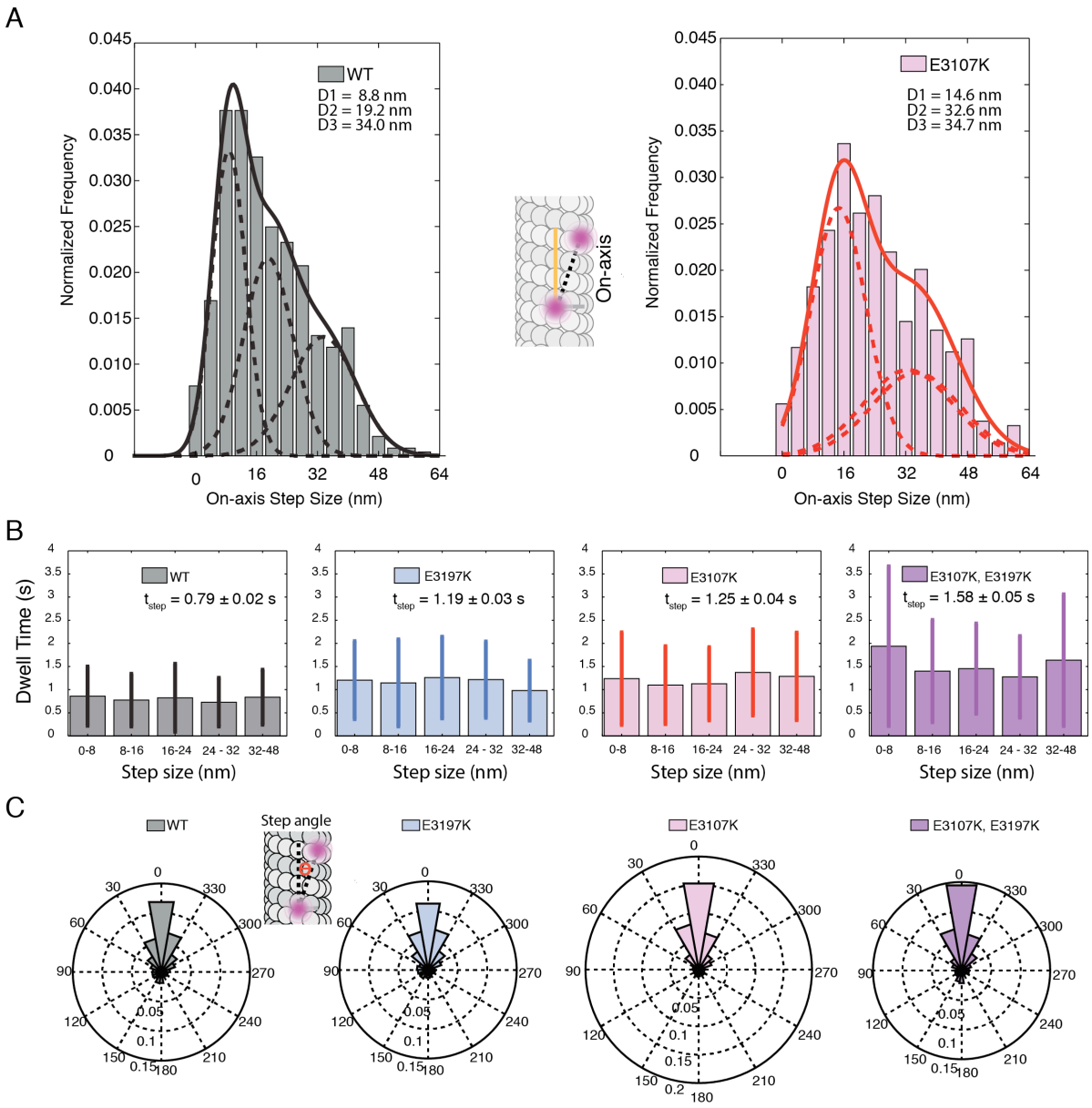


Figure 3.7 The E3107K mutation causes dynein to take longer on-axis steps
(A) Histograms of the on-axis step size for the WT dynein and E3107K mutant. The WT distribution was fitted to 3 populations centered around ~8 nm, ~19 nm and ~34 nm respectively. In the E3107K mutant there is a larger population of long ~15 nm and ~32 nm steps. **(B)** The dwell time for the different step sizes in 8 nm increments is shown for the WT and MTBD mutants. The error bars represent the standard deviation of each distribution. The average dwell time of the entire distribution is reported as mean±SE **(C)** Angular histograms of step angles for the WT and high affinity dynein mutants. The step angle is defined as the angle between each step vector and the direction of the on-axis movement. Left and right steps are between $0° < \theta < 180°$ and $180° < \theta < 360°$ respectively. Forward steps are between $0° < \theta < 90°$ and $270° < \theta < 360°$ whereas backward steps are between $90° < \theta < 270°$.

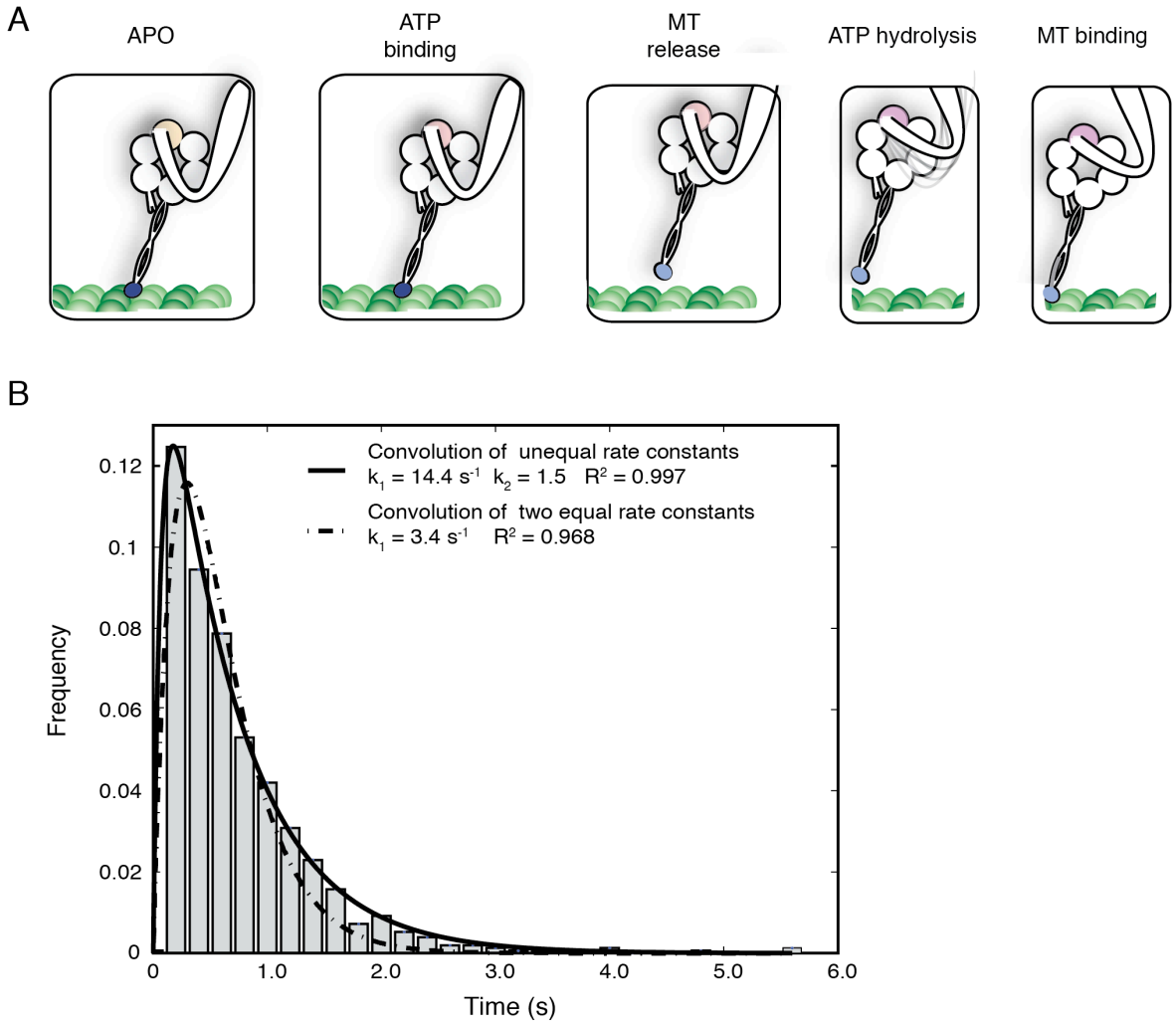


Figure 3.8 Dynein's catalytic cycle and rates constants of head-labeled WT dynein
(A) The beginning of a dynein step requires ATP binding, MT release, ATP hydrolysis and binding to a new MT-site. At low ATP concentrations the stepping rate of WT dynein is determined by the rates of ATP binding (slow) and hydrolysis (fast). In contrast, in the high affinity mutants the rate of stepping is best described by two slow steps. We propose that ATP binding and MT-release are rate-limiting. **(B)** The stepping rate of WT dynein is best fit by a convolution of two unequal rate constants. The figure shows the dwell time histogram of head-labeled WT dynein at 5 µM ATP. Data were fit to a convolution of two unequal exponential rate constants (k_{step} =A* (e^{-k1t} - e^{-k2t}), black curve) and to a convolution of two equal exponential rate constants (k_{step} =A*t* e^{-kt}, dashed curve). The stepping rate is best described by the convolution of two different constants.

We found a good fit when the WT on-axis step size distribution was expressed as the convolution of three gaussian distributions centered at 8.8, 19.2 and 34 nm, consistent with previous reports (9.3 nm, 17.5 nm, 32.9 nm) (*11*). In contrast, the distribution of the E3107K mutant was best described by three gaussian functions centered at 14.6, 32.6 and 34.7 nm. The observed distances match well the separation between tubulin binding sites (multiples of 8 nm) along the MT long axis.

We wondered whether long pauses were correlated with long steps. We analyzed the duration of the pause before a step as a function of step size, and found that dynein dwells the same time irrespective of the magnitude of the step size (Figure 3.7 B). However, the higher the MT affinity, the longer the average dwell time.

In summary, we have found that increased MT binding affinity enhances the processivity of dynein and reduces its stepping rate, most likely by slowing down MT-release. The waiting time before a step depends on the MT binding affinity irrespective of the step size. The E3197K mutation that shows a 7-fold increase in MT-affinity does not have a different step size distribution than that of the WT dynein. Unexpectedly, the E3107K mutant that has a 6-fold higher MT-affinity than WT, displays a higher percentage of long steps than previously described (*10*, *11*). This increase in step size is accounted by an increase in the relative populations of 16 and 32 nm steps relative to 8 nm steps.

Discussion

In this study we have explored the regulatory role of MT-binding affinity of the MTBD in dynein's mechanochemical cycle and stepping. Previous work on dynein's motility mechanism (*13*, *17*) has focused on characterizing the role of nucleotide binding and hydrolysis of the different AAA domains.

Our results combined with previous single molecule assays (*21*) (see chapter 2) show that MT-binding affinity significantly affect dynein's velocity, processivity and ATPase activity. These studies provide new insights into how MT-binding and release by the MTBD can affect the main hydrolytic cycle and stepping behavior of the dynein motor.

Increased MT-binding affinity directly impacts dynein processivity. The E3107K mutation (located in CC1) displays a 6-fold increase in MT-binding affinity that results in a 5-fold increase in the run-length of dynein (*21*). Similarly, the E3197K mutations (located in helix H6) shows a 7-fold increase in MT-binding affinity and a 6-fold increase in processivity. Interestingly, introducing both mutations has a cooperative effect, resulting in a 25-fold increase in binding affinity and a 20-fold increase in dynein's run length. A processive run is terminated when both motors simultaneously detach from the MT track. Higher MT-binding affinity would thus result in reduced probability of dissociation from MTs. These results provide a molecular explanation to the super processive behavior of the E3107K and E3197K mutants (*21*). Previously, a point mutation blocking ATP hydrolysis at AAA4 (walker B mutant E/Q) in a dimeric dynein construct was found to increase dynein's MT-affinity by 5-fold, resulting in a 2-fold increase in processivity (*13*). This suggests that ATP hydrolysis by the motor affects MT binding affinity and therefore motor processivity. However, this effect was most likely due to a unknown mechanism

that involves the coordination between the two heads of dynein because both WT and AAA4 mutant monomers show similar MT-binding affinity (*13*). Here, we have shown, by directly introducing mutations in the MTBD, increase in the MT-binding affinity causes enhanced processivity.

The 2-fold reduction of ATPase activity in the double mutant E3107K/E3197K shows that MT binding and release plays an important role in dynein's mechanochemical cycle. This effect could be explained -either by a direct allosteric communication through the coiled-coil that impairs nucleotide binding or hydrolysis by the AAA domains in the motor or by affecting dynein's kinetic cycle, such that the motor spends a longer time in states associated with tight MT binding or both.

In support of the kinetic effect, our analysis of dwell times show that an increased affinity for MTs slows down dynein's stepping rate. Single molecule studies suggest that a single event of ATP hydrolysis is required for dynein to take a step (*11*, *12*). Each step requires the tight coupling of multiple events that include ATP binding, MTBD release from the MT, ATP hydrolysis and binding to a new MT site (Fig. 3.8 B). At saturating concentrations of ATP (>1 mM) the stepping rate will be limited by ATP hydrolysis, however at intermediate and low (< 10 μM, below the $K_{m,ATP}$ 26 μM (*13*)) ATP concentrations, it is though that ATP binding becomes rate limiting. Indeed, our analysis show that at 5 μM ATP the dwell time distribution of head-labeled WT dyneins is best described by the convolution of two unequal rate constants (Fig. 3.8 B) in agreement with previous measurements (*11*). This is consistent with a model where dynein walks in an uncoordinated manner (*10*, *11*) and each step can be described by a fast and a slow rates (*11*). In contrast, if dynein walks hand-over-hand, the distribution would be best fit by a

convolution of two identical heads (Fig. 3.8 B) stepping at a single rate. The fast rate (k_1 = 14.4 s^{-1}) observed in the WT stepping has been interpreted as the ATP hydrolysis rate and the slow one (k_2 = 1.5 s^{-1}) as the ATP binding rate (*11*).

The underlying stepping mechanism of the high MT-binding affinity mutants seems to be different. Their dwell time histograms can be best described as the convolution of two exponential functions with unequal rates (Fig. 3.6 A). In each case, one likely corresponds to the ATP binding rate (k~1.5 s^{-1}) and the other corresponds the rate of MT-release. Another possibility to explain the stepping rate variation is that ATP hydrolysis has slowed down, however the values for the rate constants (k~2-3 s^{-1}) and our ATPase activity measurements argue against that notion. A third possibility is that the histograms are described by the convolution of two equal exponential functions, however, this would imply a hand-over-hand motility mechanism for all the high affinity mutants but not the WT. We cannot exclude an scenario where two ATP molecules bind at two different rates, however our results across mutants would imply a different modulation of ATP binding as a function of MT-binding affinity for which there is no biochemical evidence. ATPase measurements and stepping rate studies at different ATP concentrations are needed to confirm our model. A direct measurement of the MT-release rate would also add support to our idea.

We favor the idea that these two rates correspond to the events of ATP binding and MT-release. Therefore, higher MT-affinity slows down MT-release, leading to a slower stepping rate.

A slower stepping rate in the high affinity mutants explains their reduction in velocity. Using the average dwell time and the average head step size of WT and MTBD mutants we estimated the average velocity at low (5 μM) ATP concentrations as $v = d_{step}/t_{dwell}$. WT dynein moves at a

speed of 17.5 nm/s, E3107K at 16 nm/s, E3107K at 12.6 nm/s and the double mutant at 9.7 nm/s. This trend is in agreement with the average velocity measured using kymographs at saturating concentrations of ATP (*21*): WT 95 nm/s, E3107K 64.8 nm/s, E3107K 59.7 nm/s and the double mutant 51.4 nm/s. Taken together, our single molecule assays, ATPase activity measurements and stepping analysis support the idea that an increased affinity for the MT reduces dynein's stepping rate.

Our ATPase and velocity data suggest that the high affinity single mutants undergo "futile" ATP hydrolysis cycles that do not lead to forward movement. At saturating concentrations of ATP (~1 mM) the velocity can be seen as $v = k_{cat} * d_{step}$. Given that the single mutants show a similar ATPase activity and step size than WT, their velocity should have remained constant. In fact, the E3107K mutant should have moved faster due to its larger step size. Intriguingly, the reduction of ATPase activity of the double mutant thus suggests that the combination of the two single mutations restores at least partially the coupling between ATP hydrolysis and movement.

While other studies have begun to show that the activity of the AAA domains affect dynein's motility and its mechanochemical cycle, the role of the MTBD and its affinity for MTs has not been explored until now. How MT-affinity affects the affinity for ATP at AAA1 and other AAA sites has yet to be determined.

Our data revealed an unexpected function of dynein's MTBD. Intriguingly, the large steps observed for the E3107K mutant suggest a higher coordination of the two dynein heads and a potential role of the MTBD as a switch between coordinated and stochastic motility. The E3107 residue is located in CC1 (Fig. 3.3 A) and interacts with a lysine located in H1, shown to undergo a large conformational rearrangement upon MT binding (*21*). In contrast, E3197 is at the top of

H6, which remains rigid in the high and low affinity MTBD conformations but it is in close proximity to the C-terminal tails of beta-tubulin. Perhaps different MT-binding sites in dynein's MTBD are used as sensors of the C-terminal tails of tubulin or the activity of microtubule associated proteins to allow dynein to respond to its environment or bypass obstacles.

Our results support the idea that dynein's MT-binding affinity and consequently the rates of MT binding and release have been optimized for turnover by the motor and imply a two way communication between the motor domain and the MTBD. To better understand the communication between the MTBD and the motor domain that ultimately explains dynein stepping behavior, more experiments will be needed to directly probe the stepping pattern of each individual head with high affinity MTBD mutants and the nucleotide state of each AAA domain.

Table 3.3. S. cerevisiae strains used in this study. All yeast strains are based on the W303 background.

Strain ID	Genotype	Source	Figure
RPY208	*MATa his3-11,5 ura3-52 leu2-3,112 ade2-1 trp-1 pep4Δ::HIS5, prb1Δ, pGAL-ZZ-TEV-GFP-3XHA-GST-DYN1$_{331KDa}$-gsDHA-KanR*	{ReckPeterson: 2006jo}	Figure 3.4 to Figure 3.7
RPY1218	*MATa, his3-11,5; ura3-52, leu2-3,112; ade2-1, trp-1, pep4Δ::HIS5, prb1Δ, pGAL-ZZ-TEV-GFP-3XHA-GST-DYN1$_{331kDa}$(E3107K)-gsDHA-kanR*	{Redwine: 2012cr}	Figure 3.4 to Figure 3.7
RPY1235	*MATa, his3-11,5; ura3-52, leu2-3,112; ade2-1, trp-1, pep4Δ::HIS5, prb1Δ, pGAL-ZZ-TEV-GFP-3XHA-GST-DYN1$_{331kDa}$(E3197K)-gsDHA-kanR*	{Redwine: 2012cr}	Figure 3.4 to Figure 3.7
RPY1247	*MATa, his3-11,5; ura3-52, leu2-3,112; ade2-1, trp-1, pep4Δ::HIS5, prb1Δ, pGAL-ZZ-TEV-GFP-3XHA-GST-DYN1$_{331kDa}$(E3107K, E3197K)-gsDHA-kanR*	{Redwine: 2012cr}	Figure 3.4 to Figure 3.7
RPY1302	*MATa; his3-11,15; ura3-1; leu2-3,112; ade2-1; trp1-1; pep4Δ::HIS5; prb1Δ PAC11-13Myc-TRP1, pac1Δ::HPH, PGAL-ZZ-TEV-DYN1$_{331KDa}$*	{Toropova: 2014bt}	Fig. 3.3
RPY1392	*MATa; his3-11,15; ura3-1; leu2-3,112; ade2-1; trp1-1; pep4Δ::HIS5; prb1Δ PAC11-13Myc-TRP, pac1Δ::HPH, PGAL-ZZ-TEV-DYN1$_{331KDa}$ E3107K*	This study	Fig. 3.3
RPY1393	*MATa; his3-11,15; ura3-1; leu2-3,112; ade2-1; trp1-1; pep4Δ::HIS5; prb1Δ PAC11-13Myc-TRP, pac1Δ::HPH, PGAL-ZZ-TEV-DYN1$_{331KDa}$ / E3197K*	This study	Fig. 3.3
RPY1394	*MATa; his3-11,15; ura3-1; leu2-3,112; ade2-1; trp1-1; pep4Δ::HIS5; prb1Δ, PAC11-13Myc-TRP, pac1Δ::HPH, PGal-ZZ-TEV-DYN1$_{331kDa}$-E3107K/E3197K*	This study	Fig. 3.2

Acknowledgements

I like to thank Adam Wier, Indrajit Lahiri, Weihong Qiu and Hugo Arellano-Santoyo for their valuable comments and critical reading of this chapter. We thank all the members of the Leschziner and Reck-Peterson Labs for advice and helpful discussions. Single molecule data was collected at Harvard's Center for Biological Imaging, supported by an SIG award (RR1S1027990) from the NIH.

References

1. R. Vallee, J. Williams, D. Varma, L. Barnhart, Dynein: An ancient motor protein involved in multiple modes of transport. *J Neurobiol* **58**, 189–200 (2004).

2. R. Vale, The molecular motor toolbox for intracellular transport. *Cell* **112**, 467–480 (2003).

3. S. Burgess, M. Walker, H. Sakakibara, P. Knight, K. Oiwa, Dynein structure and power stroke. *Nature* **421**, 715–718 (2003).

4. A. Roberts *et al.*, AAA+ ring and linker swing mechanism in the dynein motor. *Cell* **136**, 485–495 (2009).

5. I. R. Gibbons, B. H. Gibbons, G. Mocz, D. J. Asai, Multiple nucleotide-binding sites in the sequence of dynein β heavy chain. *Nature* **352**, 640–643 (1991).

6. A. P. Carter, C. Cho, L. Jin, R. D. Vale, Crystal structure of the dynein motor domain. *Science* **331**, 1159–1165 (2011).

7. T. Kon, K. Sutoh, G. Kurisu, X-ray structure of a functional full-length dynein motor domain. *Nat Struct Mol Biol*, 1–6 (2011).

8. J. L. Ross, H. Shuman, E. L. F. Holzbaur, Y. E. Goldman, Kinesin and dynein-dynactin at intersecting microtubules: motor density affects dynein function. *Biophysical Journal* **94**, 3115–3125 (2008).

9. R. Dixit, J. L. Ross, Y. E. Goldman, E. L. F. Holzbaur, Differential Regulation of Dynein and Kinesin Motor Proteins by Tau. *Science* **319**, 1086–1089 (2008).

10. W. Qiu *et al.*, Dynein achieves processive motion using both stochastic and coordinated stepping. *Nat Struct Mol Biol* **19**, 193–200 (2012).

11. M. A. DeWitt, A. Y. Chang, P. A. Combs, A. Yildiz, Cytoplasmic Dynein Moves Through Uncoordinated Stepping of the AAA+ Ring Domains. *Science* **335**, 221–225 (2012).

12. S. L. Reck-Peterson *et al.*, Single-molecule analysis of dynein processivity and stepping behavior. *Cell* **126**, 335–348 (2006).

13. C. Cho, S. L. Reck-Peterson, R. D. Vale, Regulatory ATPase sites of cytoplasmic dynein affect processivity and force generation. *J. Biol. Chem.* **283**, 25839–25845 (2008).

14. G. Bhabha *et al.*, Allosteric communication in the Dynein motor domain. *Cell* **159**, 857–868 (2014).

15. S. L. Reck-Peterson, R. D. Vale, Molecular dissection of the roles of nucleotide binding and hydrolysis in dynein's AAA domains in Saccharomyces cerevisiae. *Proceedings of the National Academy of Sciences of the United States of America* **101**, 1491–1495 (2004).

16. T. Kon, M. Nishiura, R. Ohkura, Y. Toyoshima, K. Sutoh, Distinct functions of nucleotide-binding/hydrolysis sites in the four AAA modules of cytoplasmic dynein. *Biochemistry* **43**, 11266–11274 (2004).

17. M. A. DeWitt, C. A. Cypranowska, F. B. Cleary, V. Belyy, A. Yildiz, The AAA3 domain of cytoplasmic dynein acts as a switch to facilitate microtubule release. *Nat Struct Mol Biol* **22**, 73–80 (2014).

18. T. Kon, M. Nishiura, R. Ohkura, Y. Y. Toyoshima, K. Sutoh, Distinct functions of nucleotide-binding/hydrolysis sites in the four AAA modules of cytoplasmic dynein. *Biochemistry* **43**, 11266–11274 (2004).

19. A. P. Carter *et al.*, Structure and functional role of dynein's microtubule-binding domain. *Science* **322**, 1691–1695 (2008).

20. H. Schmidt, R. Zalyte, L. Urnavicius, A. P. Carter, Structure of human cytoplasmic dynein-2 primed for its power stroke. *Nature* (2014), doi:10.1038/nature14023.

21. W. B. Redwine *et al.*, Structural basis for microtubule binding and release by dynein. *Science* **337**, 1532–1536 (2012).

22. M. S. Longtine *et al.*, Additional modules for versatile and economical PCR-based gene deletion and modification in Saccharomyces cerevisiae. *Yeast* **14**, 953–961 (1998).

23. C. Guthrie, G. R. Fink, *Guide to yeast genetics and molecular biology.* (Methods in Enzymology, 1991), pp. 1–863.

24. W. B. Redwine, *The Structural Basis for Microtubule Binding and Release by Dynein* (2012).

25. M. Nishiura *et al.*, A single-headed recombinant fragment of Dictyostelium cytoplasmic dynein can drive the robust sliding of microtubules. *J. Biol. Chem.* **279**, 22799–22802 (2004).

26. R. E. Thompson, D. R. Larson, W. W. Webb, Precise nanometer localization analysis for individual fluorescent probes. *Biophysical Journal* **82**, 2775–2783 (2002).

27. K. Toropova *et al.*, Lis1 regulates dynein by sterically blocking its mechanochemical cycle. *Elife* **3**, – (2014).

28. J. Huang, A. J. Roberts, A. E. Leschziner, S. L. Reck-Peterson, Lis1 Acts as a "Clutch" between the ATPase and Microtubule-Binding Domains of the Dynein Motor. *Cell* **150**, 975–986 (2012).

29. A. Gennerich, A. P. Carter, S. L. Reck-Peterson, R. D. Vale, Force-induced bidirectional stepping of cytoplasmic dynein. *Cell* **131**, 952–965 (2007).

30. M. Rief *et al.*, Myosin-V stepping kinetics: a molecular model for processivity. *Proceedings of the National Academy of Sciences of the United States of America* **97**, 9482–9486 (2000).

31. A. Yildiz, M. Tomishige, R. D. Vale, P. R. Selvin, Kinesin walks hand-over-hand. *Science* **303**, 676–678 (2004).

32. A. Yildiz, J. N. Forkey, S. A. McKinney, T. Ha, Y. E. Goldman, Myosin V Walks Hand-Over-Hand: Single Fluorophore Imaging with 1.5-nm Localization. *Science* (2003).

Chapter 4

Structural basis for processive motility and microtubule depolymerase activity by the yeast kinesin-8/Kip3

Rogelio Hernandez-Lopez, Hugo Arellano Santoyo, Ema Stokasimov, David Pellman,

Andres E. Leschziner

Contributions

Rogelio Hernandez-Lopez carried out electron microscopy (EM) sample preparation, EM data collection, 3D reconstruction and molecular modeling. Hugo Arellano Santoyo performed biochemistry, EM sample preparation, EM data collection and single molecule experiments. Ema Stokasimov carried out biochemistry, EM sample preparation and made yeast strains. David Pellman and Andres Leschziner provided mentorship.

Abstract

Kinesins are microtubule based motors that play critical roles regulating microtubule dynamics and intracellular transport. Motors of the Kinesin-8 family have a conserved role in microtubule length control required for many cellular processes including spindle elongation and chromosome segregation. The yeast kinesin-8/Kip3 is a plus-end directed highly processive motor and a plus-end specific depolymerase. How these distinct functions have been acquired and are spatially coordinated given the highly conserved motor domain remains unknown. Using cryo-electron microscopy and molecular modeling, we present models of how Kip3 binds to the lattice and to the end region of microtubules . We identified and tested, using fluorescence imaging, specific residues within Kip3 important for its processivity, plus-end dwelling and depolymerization activity. Our results suggest a conserved structural mechanism for how Kip3 performs its multiple functions.

Introduction

Kinesins are ATP-driven molecular motors that play critical roles in the regulation of the microtubule (MT) cytoskeleton dynamics. Their activity controlling the size and position of the mitotic spindle, kinetochore clustering and microtubule nucleation is important for cell division, cell migration and cell-cell communication (*1*). Such functional diversity is achieved by directly interacting with MTs, or indirectly, through the transport of other factors along MTs (*2*).

The structure of MTs is conserved in all eukaryotes (*3*). MTs form *via* head to tail and lateral association of α-and ß-tubulin heterodimers, resulting in a cylindrical arrangement of ~25 nm in diameter. The MT exhibits polarity—its two opposite ends are dynamically and chemically distinct. MT growth and disassembly occur *via* association and dissociation of tubulin dimers at the "plus-end," where ß-tubulin subunits are exposed. The "minus-end," which contains exposed α-tubulin subunits, is more stable. In the cell, minus-ends are often located near the nucleus where they can attach to the microtubule-organizing centers and centrioles. In contrast, the plus-ends are found near the cell periphery and undergo phases of rapid growth and shrinkage, a behavior known as dynamic instability (*4*). Dynamic instability is an intrinsic MT property driven by binding, hydrolysis and exchange of GTP by the αß-tubulin units. However, many kinesins and other microtubule associated proteins play an important role regulating this behavior.

Kinesin-8s have an evolutionary conserved role in microtubule length control in cells (*5*-*9*). Like other members of the kinesin family, kinesin-8s use the energy from ATP-hydrolysis to move along the MT lattice. Remarkably, they are know to be some of the most processive motors (*6*, *7*)and have the unconventional ability to regulate the dynamics of MT plus-ends (*6*-*9*).

Kip3, the budding yeast kinesin-8, is a homodimer of catalytic and MT-binding subunits (Figure 4.1 A). The major functional elements of each subunit (Figure 4.1B) include: (a) a "tail" domain required for passive MT binding and sliding (*10*), (b) a coiled-coil "stalk" required for dimerization; (c) a "head" or "motor domain" that contains elements responsible for MT-binding and ATP hydrolysis (*11*), and (d) a flexible "neck linker" region joining the catalytic head with the coiled-coil.

The functional motifs by which kinesin-8s are thought to regulate the plus-end activity and high processivity remain unknown. A low resolution cryo-EM study suggests that in addition to the conserved MT binding surface, an extended loop 2 (L2) in kinesin-8 makes a contact with alpha-tubulin (*11*). This study proposed that the additional interaction is responsible for both, increasing kinesin-8 processivity and favoring a bent conformation of the terminal tubulin at the plus-end (*11*). The role of loop2 in depolymerization is appealing given that a similar extended L2 is also found in members of the kinesin-13 family of non-motile depolymerases. Mutating the family conserved KVD sequence in L2 reduces kinesin-13 depolymerizing activity (*12*, *13*). However, unlike kinesin-13s, the most potent MT-depolymerases so far identified, kinesin-8s are weak depolymerases and do not have the KVD sequence in their loop2. Thus, it is not clear how differences between the L2 sequences of kinesin-8s and kinesin-13s could explain such differences in activity.

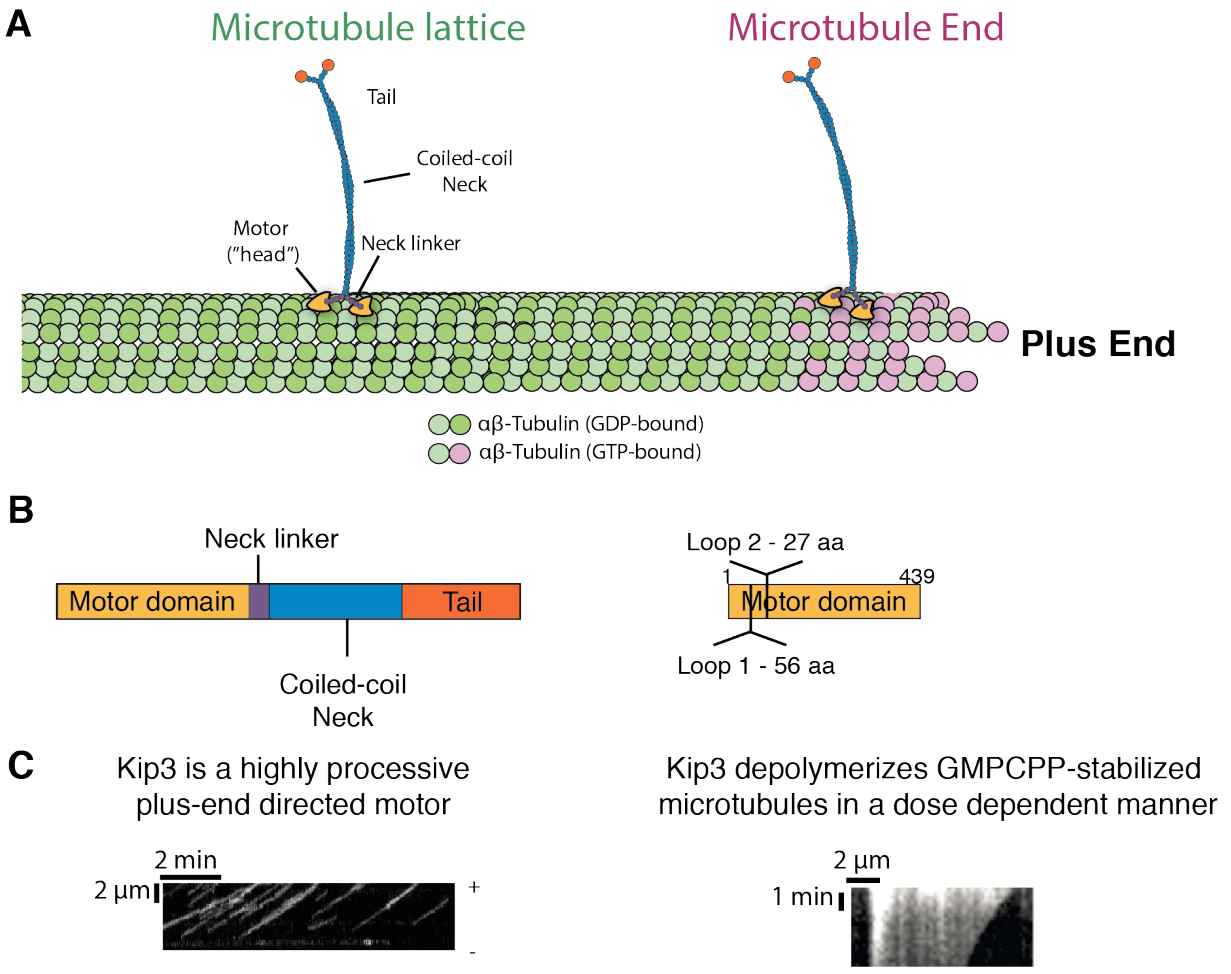


Figure 4.1 The yeast kinesin8/Kip3 is a highly processive plus-end directed motor that is able to dwell at MT-ends and alter their dynamics.

(A) Schematic view of Kip3 moving along microtubules (MTs). Members of the kinesin-8 family are plus-end directed motors that are able to dwell at the plus end and alter their dynamics. The figure depicts a microtubule with its "GTP cap", GTP-bound β-tubulin. The microtubule plus-end is highly dynamic and chemically distinct from the lattice. The addition and removal of tubulin subunits at the plus-end is regulated by microtubule associated proteins and members of the kinesin superfamily. **(B)** left: Schematic of the domain organization of kinesin-8s. The main functional domains are: a N-terminal motor domain, a flexible neck-linker, a coiled-coil neck important for dimerization and an additional MT-binding site known as the "tail", important for MT-sliding. Right: Schematic view of the construct used in this study for cryo-EM imaging. Kip3-specific loop1 and loop 2 inserts were removed to minimize conformational flexibility. The inserts are dispensable for motility and depolymerization activity and yield higher protein stability. The number of residues that were removed from each insert are indicated.

Figure 4.1 The yeast kinesin8/Kip3 is a highly processive plus-end directed motor that is able to dwell at MT-ends and alter their dynamics (Continued)
(C) Left: Kip3 is a highly processive motor, its characteristic run length is ~6 μm. Representative kymographs of fluorescently labeled Kip3 moving along taxol-stabilized MTs. The kymograph follows the trajectory of several Kip3 molecules along a stretch of a single MT. MT polarity is indicated. Horizontal scale bar, 2 min; vertical scale bar, 2 μm. Right: Kip3 depolymerizes GMPCPP-stabilized MTs in a Kip3 dosage dependence manner. Representative kymograph of a fluorescently labeled GMPCPP-stabilized MT in the presence of Kip3. Horizontal scale bar, 2 μm ; vertical scale bar, 1 min.

Moreover while kinesin-13s are non-motile, kinesin-8s are highly processive motors (*6*, *9*). The role of L2 in kinesin-8s processivity or MT-end regulation activity remains untested.

The dual function of kinesin-8s for motility and regulation of MT dynamics raises a fundamental mechanistic question (*5*): do kinesin-8s interact with tubulin when they walk along the lattice in the same manner or differently than the interaction that occurs at the MT-end?

Understanding the mechanism by which kinesin-8 undertakes the apparently divergent activities of MT-motility and MT-end dynamics regulation would be aided by a structural comparison of kinesin-8 bound to the MT-lattice (GDP) and to the MT-plus end (GTP).

Here, we describe high resolution cryo-electron microscopy (cryo-EM) structures of the kinesin-8/Kip3 motor domain bound to static mimics of the microtubule lattice (GDP-taxol) and MT-end (GTP-like, GMPCPP). Our results provide insight into the mechanisms of motility and MT-end depolymerization by Kinesin-8s.

Materials and Methods

S. cerevisiae strain construction

They are in the W303-1A background as previously described (*8*). For EM studies, Kip3 specific loop1 and loop 2 inserts were removed from the WT Kip3 coding sequence (1-436) to build a monomeric Kip3-ΔL1ΔL2 construct.

Protein expression and purification

Kip3 constructs for electron microscopy studies were expressed and purified as described previously (*8*). Protein expression was driven by a galactose inducible promoter (*14*) on 2 μ plasmids (pRS425 backbone). Starter cultures of *S. cerevisiae* were grown in YPD broth and induced with galactose to a final concentration of 2%. The cells were grown for 18 h at 30 °C before collecting them by centrifugation. The cells were disrupted by mechanical force using a coffee grinder and the yeast powder was thawed, and then resuspended in lysis buffer (50 mM $NaPO_4$, 500 mM NaCl, 10% glycerol, 0.5 mM ATP-Mg, 40 mM imidazole, 2 mM dithiothreitol, 1% Triton X-100, protease inhibitor cocktail tablets (Roche) and 2 mM phenylmethylsulphonyl fluoride at pH 7.4) at 4 °C.

A Dounce homogenizer was used to further lyse cells at 4 °C. After centrifugation at 180,000g for 45 min at 4 °C, the supernatant was collected and incubated with a Ni^{2+} Sepharose resin (GE Healthcare) for 30 min at 4 °C. The resin was then washed 3 times with buffer (50 mM $NaPO_4$, 500 mM NaCl, 10% glycerol, 0.1 mM ATP-Mg, 25 mM imidazole, 0.1 mM dithiothreitol, protease inhibitor cocktail tablets and 1 mM phenylmethylsulphonyl fluoride at pH 7.4). For single molecule studies, the protein was labelled with 10 μM TMR (Promega) for 1.5 h at 4 °C before elution. The bound protein was then eluted using elution buffer (50 mM HEPES, 300 mM NaCl, 50 mM EDTA, 5 mM $MgCl_2$, 50 μM ATP-Mg and 0.1 mM dithiothreitol at pH 7.4). The protein fractions were adjusted to 250 mM NaCl and loaded onto a Uno S1 (Bio-rad) ion exchange column equilibrated with 50 mM HEPES, 250 mM NaCl and 50 μM ATP-Mg at pH 7.4. The protein was eluted by a linear gradient from 0 to 1 M NaCl over 15 column volumes. Peak fractions were supplemented with 10% sucrose and large aggregates were removed by

centrifugation at 200,000g for 5 min at 4 °C. The supernatant was collected and 20 µL aliquots were snap-frozen in liquid nitrogen and stored at −80 °C.

Tubulin polymerization for Cryo-EM

Highly purified, glycerol-free tubulin (Cytoskeleton, Inc.) was resuspended in BRB80 (80 mM PIPES-KOH, pH 6.8; 1 mM MgCl2, 1 mM EGTA, 1 mM DTT) to a concentration of 10 mg/mL. To prepare taxol-stabilized microtubules, tubulin was polymerized with a stepwise addition of taxol as follows: 20 µL of tubulin stock was thawed quickly and placed on ice. 10 µL of BRB80 supplemented with 3 mM GTP were added and the mixture was transferred to a 37 °C water bath. After 15, 30, and 45 minutes, additions of 0.5, 0.5, and 1.0 µL of 2 mM taxol were added by gentle swirling. The mixture was then incubated for an additional 1 h at 37°C.

GMPCPP microtubules were polymerized using GMPCPP seeds (20 µM tubulin, 1mM GMPCPP, 1mM $MgCl_2$, 1mM DTT in BRB80). A 1 µL aliquot of seeds was transferred to a 37 °C water bath. After 30 minutes, 40 µL of elongation mix (2 µM tubulin, 0.5 mM GMPCPP, 0.5 mM MgCl2, 1 mM DTT in BRB80) were added and the mixture was then incubated for additional 4.5 -5 hours at 37 °C.

Grid preparation and imaging

Purified Kip3-ΔL1ΔL2 protein was buffer exchanged to cryo buffer (50 mM Tris-HCl, pH 8.0, 1 mM MgCl2, 1 mM EGTA, 1 mM DTT supplemented with 2mM AMPPNP) and desalted using a ZEBA spin desalting column. The protein was recovered by centrifugation at 15.000 rcf for 2 min. A final spin at 30,000 x g in a TLA 100 rotor (Beckman) for 10 min at 4 °C was

carried out to remove big aggregates.

C-flat 1.2/1.3-2C holey carbon grids (Protochips) were glow-discharged for 20 s at 20 mA in an table top plasma cleaner (Electron Microscopy Sciences). Taxol-stabilized MTs were diluted to 0.5 mg/mL in cryo buffer supplemented with 100 μM taxol and GMPCPP microtubules were diluted to 0.25 mg/mL in BRB80 buffer. 4 μL of MTs were added to a grid and allowed to absorb for 30 s. The solution was manually blotted from the side with a torn Whatman #1 filter paper. Next, 4 μL of desalted AMPPNP-kinesin were added and allowed to bind to the MTs for 30 s. The solution was blotted manually again, and the process of addition and blotting of kinesin was repeated for a total of four times. The final blotting was done inside the humidity chamber of a Vitrobot Mark IV (FEI) set at 22° C and 100% humidity. The grids were then rapidly plunged into a liquid nitrogen-cooled ethane slush. Grids were stored in liquid nitrogen until imaging.

Grids were imaged on a FEI Titan Krios (Janelia HHMI Research Campus), equipped with two direct electron detectors, an image corrector for spherical aberration correction, a Gatan Image Filter (GIF), and a high-brightness field emission gun (X-FEG). The two direct electron detectors are a pre-GIF FEI Falcon and a post-GIF Gatan K2 Summit. Images of Kip3 decorating Taxol-MTs or GMPCPP MTs were collected using either a FEI Falcon or a Gatan K2-summit direct detectors, and nominal magnification of 59,000. (Falcon) and 50,000 (K2-summit). Final accumulated electron doses were 25 electrons/Å^2 for the Falcon camera and 40 electrons/Å^2 for the K2-camera. Images using the K2-camera were collected in super-resolution mode. The total exposure time was 4 seconds, fractionated into 20 subframes, each with an exposure time of 0.2 s. The calibrated magnifications resulted in images of 1.07 Å/px (Falcon) and 0.52 Å/px (K2

camera in super resolution) on the specimen. Images were recorded using a semi-automated acquisition program, FEI automated sofware (Falcon Camera) and Serial EM (K2-summit) with a defocus range from 1.5 to 3.5 μm.

Another two data sets of Kip3-decorated GMPCPP Microtubules were collected on a TF30 Polara electron microscope (FEI) operated at 300 kV and equipped with a K2-summit direct detector. Images were recorded in super resolution counting mode at a nominal magnification of 39,000x corresponding to a calibrated super-resolution pixel size of 0.49 Å/px. The total exposure time was 5 s, resulting in a total accumulated dose of 40 electrons/$Å^2$ divided into 20 subframes, each with an exposure time of 0.25 s. Images were acquired using Serial EM with a defocus range from 2.0 to 3.5 μm.

Image processing and three-dimensional reconstruction

Inspection, defocus estimation, microtubule picking and stack creation were performed within the Appion processing environment (*15*). Images were selected for processing on the basis of high decoration, straight MTs, and the absence of crystalline ice. The contrast transfer function (CTF) was estimated using CTFFIND (*16*)with a 500 μm step search. A second CTFFIND run with a 100 μm step search was carried out to refine the initial defocus values. Micrographs whose estimated resolution was lower than 8 Å with 0.8 confidence were excluded. Microtubules were manually selected and box files containing square segments of 720 pixels centered around the MT were written at a spacing of 80 Å. Pixel intensities were normalized using XMIPP and segments were decimated 3-fold. Reference free 2D-classification of particles binned by a factor of 3 were subjected to 5 rounds of iterative multivariate statistical analysis

(MSA) and multi-reference alignment (MRA) using CAN as described previously (*17-21*). We also carried out the particle extraction, normalization and reference-free 2D classification using Relion (*22*). We found that both methods are reliable to sort MT segments on the basis of degree of decoration and protofilament number (PF) giving roughly the same population distribution of highly decorated 13 or 14 protofilament microtubules (Data not shown). After analyzing the power spectrum and one-dimensional projection of class averages, good quality particles assigned to highly decorated 13 and 14 protofilament MTs were selected for further processing. A summary of the Cryo-EM data collection and processing is shown in Table 4.1.

For 3D reconstruction we utilized a protocol described previously (*21*) with some modifications. Synthetic models for a turn of a 13- and a 14-protofilament undecorated microtubules (PDB 1JFF (*23*)) were used to generate initial low resolution volumes (20 Å) at the calibrated magnification using SPIDER. These volumes were used as references in a multi-model projection matching classification and reconstruction using custom scripts of EMAN2/SPARX (*21*). Projections along the main microtubule axis are created using an angular step that is decreased incrementally form 4 to 1 degrees. A 10 degree out of plane tilt was also included to create references for aligment.

After each reconstruction cycle, helical parameters for three-dimensional reconstructions were obtained using the hsearch_lorentz program (*24*). The helical symmetry was imposed in real space and the protofilament with all the Kip3-tubulin correctly aligned was extracted using a wedge mask. This “correct” protofilament was used to build a new average model with the MT-seam present to start a new refinement cycle.

We included the CTF correction and further sorted the MT segments using a likelihood-based

classification recently implemented in FREALIGN (*25*). When the classification converged, the stacks were split into 13 or 14 PF MTs particle stacks for further refinement of the alignment parameters. For refinement in Frealign, the euler angles were refined first without any symmetry constrains, the helical parameters were determined using the hsearch_lorentz program (*24*) and the symmetry was imposed using a pseudo-helical symmetry operator implemented in FREALIGN without further refinement of helical parameters. In this algorithm, each 80 Å segment is included multiple times in the reconstruction, using the Euler angles and shifts, to generate symmetrically equivalent views. Due to the presence of the seam in the 13 or 14 PF MTs, each segment was inserted 12 or 13 times. A SPIDER script was used to rebuild the MT containing the correct seam position, as described (*19*, *26*). The best alignment parameters obtained with data binned by a factor of 2 were used as initial parameters to further refine the unbinned data.

The 3D-reconstructions obtained from the data collected with the Falcon camera were used as initial models to process the K2-camera data sets.

Dose fractioned super-resolution stacks were aligned to remove beam induced-motion and binned 2x2 using the *motioncorr* UCSF software (*27*). After motion correction the sum image was used for initial processing in Appion.

The same processing protocol was used as described above. Initially, 3D-reconstructions were obtained using the averaged particles from the 20 subframes of motion corrected images. Particles above the overall average score in Frealign were excluded from the final reconstructions. Further refinement using the best particles but averaged from subframes 5-12 improved the resolution further to the final values. The first 5 frames contained most of the

motion and the later frames accumulate radiation damage.

The final resolution of each reconstruction was estimated by calculating the Fourier Shell Correlation of the entire reconstruction or a single tubulin dimer extracted from odd and even volumes as previously described (*21*).

For the best Kip3-MT(taxol), a local resolution analysis and resolution guided local filtration were performed using ResMap (*28*) and Blocres (*29*). The two approaches were consistent with the visual inspection of our reconstruction after sharpening the maps. The resolution of the map containing the Kip3-MT interface is higher than elements away from the MT surface. The average resolution of the 14PF Kip3-MT(taxol) map calculated from half volumes is 4.4 Å (FSC 0.143 criterion), whereas the tubulin portion is at 3.5 - 4.0 Å, average 3.8 Å (FSC 0.143 criterion) resolution, consistent with our ability to see bulky side chains and the nucleotide densities and the taxol molecule bound to tubulin. For visualization of the high resolution features and model building, the final map was sharpened with a a B-factor of -150 $Å^2$ using the program BFACTOR, with the high resolution cutoff determined by the FSC 0.143 criterion.

Pseudo-atomic model building with flexible fitting molecular dynamics

Due to the different resolutions of our 3D reconstruction, a multistep protocol of molecular dynamics flexible fitting with different maps was carried out to build pseudo-atomic models of the Kip3-microtubule complexes. To obtain the model of the Taxol-stabilized microtubule, the map was filtered at 3.8 Å and segmented to obtain densities comprising two tubulin dimer units using UCSF Chimera (*30*). Atomic coordinates for two tubulin dimers (PDB 3J6G) derived from a 5.5 Å cryo-EM map (EMDB 5895) (*21*) were used for rigid body docking using UCSF Chimera. Symmetry restrained molecular dynamics flexible fitting (MDFF) (*31-33*) was utilized

to refine the backbone position and orientation of the sidechains observed in our cryo-EM map. A system comprising two tubulin dimers was embedded in a box of water molecules using the VMD plugin "Solvate" with a 10 Å distance from the closest protein atoms to the box edge. The VMD plugin "Autoionize" was used to randomly place potassium and chloride ions that simulate a final KCl concentration of 0.05 M. All-atom molecular dynamics simulations were performed using the software NAMD 2.9 (*34*), the CHARMM27 force field with CMAP correction terms (*35*) and the TIP3P water model (*36*). Previously derived topology parameters for the GDP, Mg, GTP (*37*) and taxol (*38*) were utilized during the simulations. The system was minimized for 2000 steps followed by 10 ns of MDFF at 300 K using a force-scaling factor (ξ) of 0.3 kcal/mol and constraints on secondary structure elements and chiral atoms. During MDFF simulations, the temperature was kept constant at 300K using Langevin dynamics with a damping coefficient of 5 ps-1. The long-range electrostatic interactions were calculated using the Particle Mesh Ewald method (PME) and the van der Waals interactions were computed with a 10 Å cutoff using periodic boundary conditions. After this initial symmetry restrained-MDFF simulation the system was equilibrated for 100 ps in the NPT ensemble at 300 K and 1 atm using the Nose-Hoover Langevin piston with a 200 fs decay period and a 50 ps^{-1} damping time constant for the pressure and 0.1 ps^{-1} for the temperature. PME was used for long-range electrostatic interactions and a 12 Å cutoff (switching function at 10 Å) for van der Waals interactions. A uniform integration step of 2 fs was used during NPT simulations. The system was subjected to 10 more ns of symmetry-restrained MDFF at 300 K using a force-scaling factor (ξ) of 0.3 kcal/mol.

After these simulations, we observed that the residues close to the inter-dimer interface were not correctly positioned. This most likely was due to the absence of the adjacent tubulin

dimers that were not present in our initial simulations. To refine the positions of the residues in the interdimer tubulin interface, a system comprising two MT protofilaments (PFs) and 4 tubulin dimers was built. Through periodic boundary conditions (PBC), the PFs were effectively infinite. The coordinates for the additional dimers were obtained by displacing the coordinates of the tubulin monomers and nucleotides by 83.0 Å in the z-direction. To place the water and ions, we added an extra monomer on the plus-end of each PF. The system was embedded in a box of water molecules using the VMD plugin "Solvate" with a 10 Å distance from the closest protein atoms to the box edge. The extra monomers and nucleotides were removed, and the water layer was trimmed to have a length of 166 Å along the z-axis, corresponding to the length of two tubulin dimers. The resulting system was used to place potassium and chloride ions that simulate a final KCl concentration of 0.05 M.

The system was minimized for 2000 steps followed by 3 ns of symmetry restrains MDFF at 300 K using a force-scaling factor (ξ) of 0.3 kcal/mol and 15 ns using force-scaling factor (ξ) of 1.0 kcal/mol and constraints on proline backbone to maintain the cis-conformation and chiral atoms. The map portion comprised one lateral interface and four tubulin interdimer interfaces. Two tubulin dimers were under the map forces, the additional monomers were constrained on the Cα atoms using a 200 kcal/mol$Å^2$ force constant.

Kip3-tubulin homology model

A full-chain protein structure prediction for the Kip3-ΔL1ΔL2 was carried out using the Robetta server (http://robetta.bakerlab.org/). Robetta uses Rosetta and parses protein chains into putative domains that are modeled either by homology modeling or ab-initio. The coordinates for two

tubulin dimers obtained above we used to build a tubulin-Kip3 system. The 2 tubulin-Kip3 dimers were rigid body docked into our density filtered at 4.4 Å, the output system was solvated and ions were randomly placed as described above. The system was minimized for 1000 steps followed by 20 ns of MDFF/TMD at 300 K using a force-scaling factor (ξ) of 1 kcal/mol and constraints on prolines and chiral atoms. In this cases the forces were just applied to the backbone to avoid over-fitting due to the lower resolution of our map.

Motility and depolymerization assays

Single molecule motility assays were performed as previously described (*8*). Microtubules were immobilized on a cover slip and the motors were added to the motility chamber in motility buffer, BRB80 pH=7.2 supplemented with 0.5 mg/mL casein, 5% glycerol, 2 mM ATP, 20 μM taxol, 50 mM KCl and an oxygen scavenger system. Images were recorded every 2 s for 20 minutes at 100 ms exposure time. For depolymerization assays GMPCPP-stabilized microtubules were used instead of taxol-stabilized MTs.Wide field images were recorded every 15 s fro 10 minutes. The protein concentration was adjusted to 24 nM.

Results

In order to gain insight into the kinesin-8's mechanism for high processivity and regulation of MT-end dynamics, we used the budding yeast kinesin-8, Kip3 as a model. Kip3 is a highly processive plus-end directed motor that is able to dwell at the plus-end of microtubules (*7*). Kip3 depolymerizes guanylyl 5′-α,β-methylenediphosphonate (GMPCPP)-stabilized microtubules,

which are thought to mimic MT-ends, (*6*, *9*) and has been shown to be a catastrophe factor on dynamic microtubules *in vitro* (*39*).

To obtain a structural understanding of the Kip3-microtubule interaction at high resolution, we took advantage of recent developments in cryo-electron microscopy. We collected images of MTs highly decorated with a monomeric Kip3 construct (Figure 4.1 C) using electron direct detectors (Figure 4.6), and adapted image processing methodologies (*19*, *21*) to solve structures of Kip3-bound to microtubules stabilized by taxol or GMPCPP (Figure 4.3). A recent cryo-EM study (*21*) showed that the structure of GDP-taxol tubulin and GMPCPP-tubulin are highly similar (At ~4.5 - 5.5 Å resolution), however, previous single molecule studies (*6*, *8*, *9*) and recent functional assays (Arellano Santoyo et. al., unpublished data) suggest a differential activity of Kip3 on taxol and GMPCPP-stabilized microtubules and a strong correlation between experiments on stabilized and dynamic microtubules.

To minimize flexible domains that often limits the resolution of structural studies, we deleted two Kip3-specific loop 1 and loop 2 insertions (~100 aminoacids) (Figure 4.1C) from the WT Kip3 sequence. These insertions shown to be irrelevant for motility and depolymerization (Figure 4.5). We obtained cryo-EM maps of monomeric Kip3-ΔL1ΔL2 (referred to here as "Kip3") bound to the MT-lattice and the MT-end initially at ~6-7 Å (Figure 4.3) and subsequently at 4.4 Å overall and 3.5 Å for a large portion of the tubulin (GDP-taxol state) density and Kip3-tubulin interface. (Figure 4.2, Figure 4.7). Ongoing work is focused on improving the resolution of the Kip3-MT-(GMPCPP) reconstruction. However even at the current resolution of our reconstructions we noticed some differences that we describe below.

Kip3 binds to α-tubulin and β-tubulin at the intradimer interface as previously reported for other members of the kinesin family (*26*, *40*, *41*) both at the MT-lattice and the MT-end (Figure 4.3). Our Kip3-MT(GDP-taxol) reconstruction has enough resolution to refine the position of most side chains in the αβ-tubulin heterodimer (Figure 4.8) and to reliably build a model for the Kip3 backbone and some side chains into the EM-density (Figure 4.2, Figure 4.9), therefore allowing us to have a high resolution model of the Kip3-MT-lattice interaction.

To obtain a pseudo-atomic model of the Kip3-tubulin (GDP-taxol) state, we used molecular dynamics (MD) and our cryo-EM reconstruction. First, we rigid-body docked an atomic-resolution model of the tubulin dimer (*21*) into our cryo-EM map filtered at 3.8 Å and used symmetry restrained molecular dynamics flexible fitting (MDFF) (*31-33*) in explicit solvent to refine the side chains of the tubulin structure. We then fitted a Kip3 homology model into our map and used explicit-solvent MDFF to resolve steric clashes and position secondary structure elements visible in our EM map at 4.4 Å.

Figure 4.2. High resolution Cryo-EM structure of Kip3 bound to Taxol-stabilized microtubules.

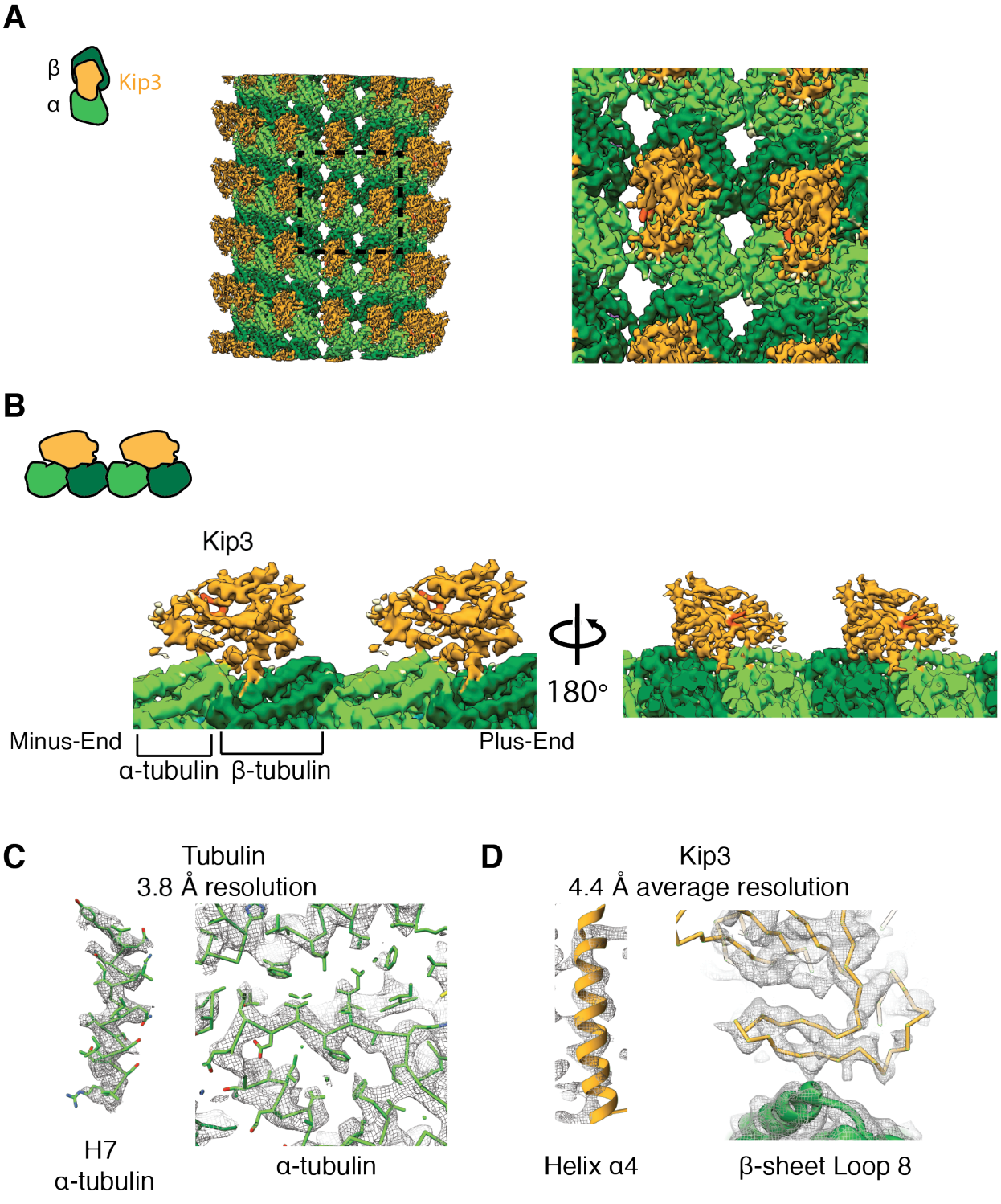


Figure 4.2. High resolution Cryo-EM structure of Kip3 bound to Taxol-stabilized microtubules (Continued)

(A) Cryo-EM 3D reconstruction of Kip3 bound to taxol-stabilized MTs at 4.4 Å resolution. Kip3 is depicted in yellow, α-tubulin and β-tubulin in light and dark green respectively. **(B)** Two different views of the reconstruction are shown. The MT minus- and plus-end are indicated. **(C)** Representative cryo-EM densities (mesh) and the refined atomic model for the taxol-stabilized tubulin dimer. The map was filtered at 3.8 Å resolution. (D) Representative cryo-EM densities for two domains in the Kip3-MT interface. Notice that the two β-strands in loop8/β5 are well resolved.

Figure 4.3 Cryo-EM reconstructions of Kip3 bound to the MTs stabilized by taxol or GMPCPP.

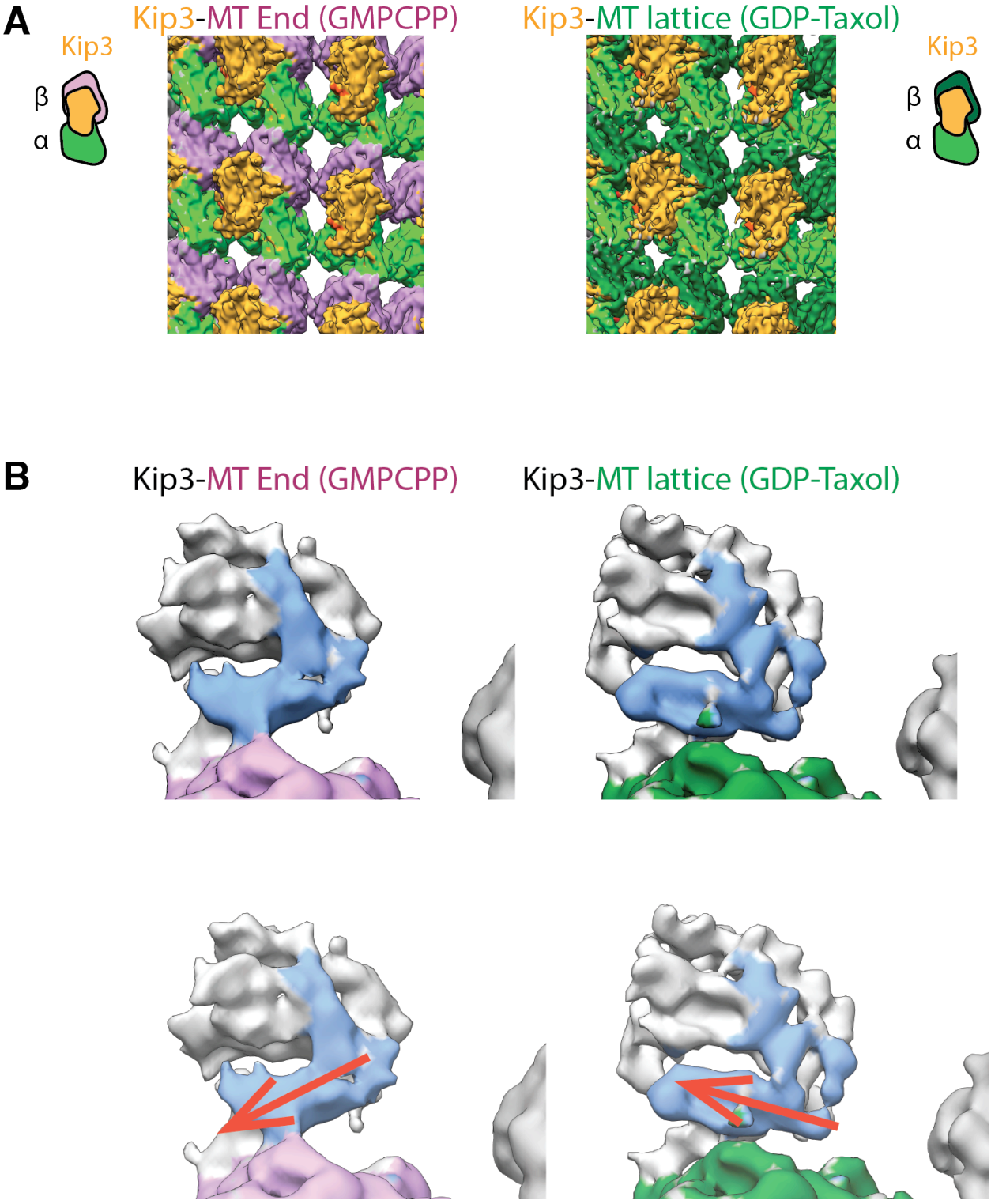


Figure 4.3 Cryo-EM reconstructions of Kip3 bound to the MTs stabilized by taxol or GMPCPP (Continued)
(A) Cryo-EM 3D map of Kip3 bound to GMPCPP-stabilized and taxol-stabilized MTs. The GMCPP bound tubulin has been proposed to be a mimic of the GTP-bound tubulin present in the GTP-cap at MT plus-ends. Kip3 is depicted in orange, α-tubulin, GTP β-tubulin and GDP-taxol β-tubulin in light green, pink and dark green respectively. The Kip3-MT(GMPCPP) map has been filtered at 5.6 Å resolution whereas the Kip3-MT(GDP-Taxol) at 5.0 Å resolution. The kip3 densities in both states are very similar in most parts. **(B)** Same views of the Kip3-MT 3D reconstruction. The red arrows highlight a putative motion of the Loop8/β5. shown in light blue, as a function of the microtubule state.

Most of the Kip3 sequence in our construct is visible at the average map resolution, however the loops L2, L11 and L12 are more flexible and are distinguishable at lower resolution (~7.5 Å)(Figure 4.4 A, Figure 4.7).

Our cryo-EM map shows 3 points of density between Kip3 and tubulin (GDP-taxol). The helices α4, α5 and α6 directly contact the microtubule as previously shown for other kinesins (*41*, *42*). There are two additional points of density at a lower threshold corresponding to L2 and L8 regions. These densities are not resolved at the average resolution, likely due to conformational flexibility.

To gain a further understanding of the Kip3 interactions with the MT-lattice, we identified Kip3 residues interacting with tubulin residues during our MDFF simulations. The majority are positively charged residues, highly conserved in the kinesin super family (K394, R391, R397, N364 and K430), mutating them to alanine results in MT-binding defects (*43*). We focused on residues that are conserved in the kinesin-8 family or seemed to be Kip3 specific and investigated their function using single molecule assays.

In our MD simulations, basic residues R351, R353 and R356, located at the end of α4 and loop 11, formed dynamic saltbridges with acidic residues on the MT surface (Figure 4.4 C). Due to the electrostatic nature of these interactions, we hypothesized these residues to be important in microtubule binding affinity, therefore affecting Kip3‘s processivity and plus-end dwelling.

To test this hypothesis we mutated these residues to alanine, purified and labeled Kip3 dimers, and performed single molecule motility assays using fluorescence microscopy. The R353A, R356A double mutant shows a significant decrease in Kip3’s run length and plus-end dwell time with nearly a three-fold increase in velocity (Figure 4.4). These results suggest that

positively charged residues in L11 have been selected to increase processivity and allow plus-end dwelling. The increased velocity suggests that these residues may also be involved in regulating the ATPase activity of the motor.

An arginine residue in loop12 (R384) was observed to have electrostatic interactions with negatively charged residues on β-tubulin (Figure 4.4B,C). Mutating this residue to alanine did not have an effect on motor velocity, however it showed an increase in the plus-end dwell-time that correlated with a 2-fold increase on depolymerization activity. This result was unexpected because it suggests that disrupting a favorable interaction between Kip3 and the microtubule antagonizes other interactions at a different site that potentially control the plus-end dwelling and activation of depolymerization. Given our results on the R353A, R356A double mutant, we propose that the site responsible for dwell time and depolymerization activity is the arginine-rich loop 11. Further experiments will test this hypothesis.

We noticed an intramolecular interaction between H268 in Loop 8 (L8/β5) and F333 located in β7 (Figure 4.4 C). This interaction seems to constrain the distance and angle between the tip of L8 and the β-sheets in the kinesin core. Moreover, the H268-F333 interaction restrained a salt-bridge between R262 and E419 (β-tubulin) as seen in our MD simulations. Interestingly, our Kip3-MT-end (GMPCPP) structure suggests a different L8 conformation when compared to our Kip3-MT-lattice structure (Figure 4.3 B). Therefore, we hypothesized that the L8 conformation may be relevant in Kip3's depolymerization mechanism and that the H268 - F333 intramolecular interaction might weaken the Kip3-MT interaction. Abolishing this interaction should result in an enhanced interaction of the R269 residue with the microtubule and a different L8 conformation.

Figure 4.4 Key residues in Kip3's loop 11, loop8 and loop 12 regulate its processivity, dwell time and depolymerization activity.

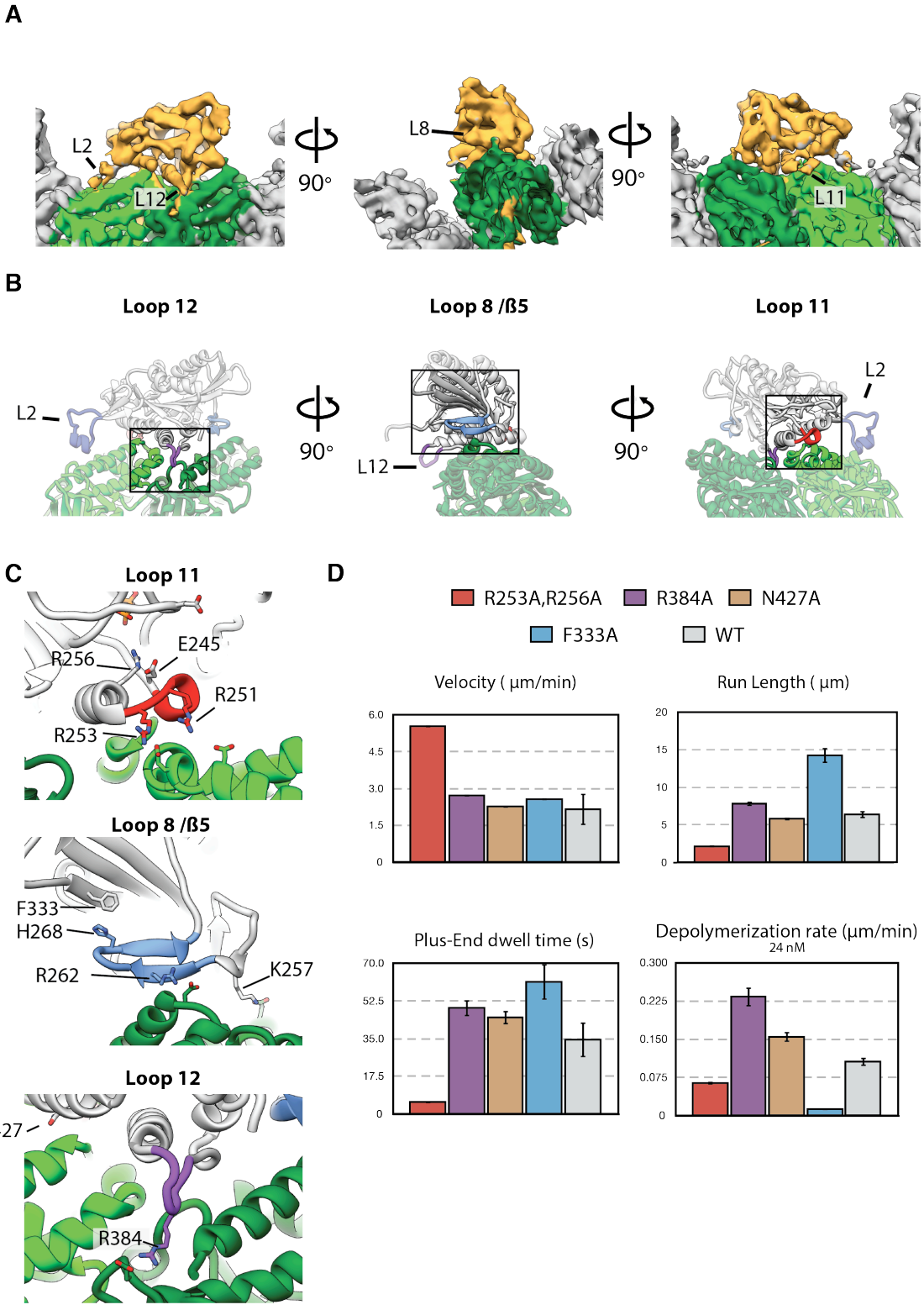


Figure 4.4 Key residues in Kip3's loop 11, loop8 and loop 12 regulate its processivity, plus-end dwell time and depolymerization activity (Continued)
(A) Different views of the Kip3-MT(GDP-taxol) 3D reconstruction locally filtered to visualize the density corresponding to loop 11 and loop 12. (See Figure 4.7 C). **(B)** The corresponding vies for the pseudo-atomic model for the Kip3-MT(GDP-taxol) complex are shown. Salt bridges between Kip3 and the MT, as detected by molecular dynamics simulations in the pseudo-atomic model, are highlighted and labeled. **(C)** Enlarged views of the highlighted areas shown in B. The residues involved in electrostatic interactions with the MT and the F333-H268 intramolecular interaction are labeled. **(D)** Mean velocities, characteristic run lengths, and mean plus-end dwell times of fluorescently labeled Kip3 bearing the indicated mutations moving on taxol stabilized MTs. The plot to the right and bottom shows the mean depolymerization rates of Kip3 mutants at 24 nM concentration on GMPCPP-stabilized MTs. Error bars indicate the standard error of the mean SE.

To test these predictions, we mutated the F333 residue to alanine, purified Kip3 dimers, and tested its depolymerization activity on GMPCPP-MTs and its motility on taxol-stabilized MTs. In support of our hypothesis, the F333A mutation significantly increased its processivity and plus-end dwell time, suggesting a tighter interaction between Kip3 and the microtubule. Future experiments will be devoted to explain the impaired depolymerization activity of this mutant. One possibility is that the H268-F333 is part of the mechanism required for depolymerization by restraining the interaction of R269 with the MT. The other is that the L8 conformation has been optimized for its interaction with the microtubule and disrupting H268-F333 changed this conformation.

Discussion

Our results provide valuable insight into the kinesin-8 mechanism and a molecular model for Kip3's enhanced processive motility and MT-end depolymerization activity.

Similarly to conventional kinesin, Kip3's motility most likely requires the neck-linker mediated coordination of its two motor domains. However, the arginine-rich loop 11 and loop 2 contribute to enhance Kip3's interaction with negatively charged residues on the MT surface and the tubulin C-terminal tails (Arellano Santoyo et al., Unpublished results) therefore increasing Kip3's processivity. Consistent with this idea, our EM map shows interactions of L2 and L11 with the MT, most likely due to the arginine rich-sequences present in those Kip3 regions. In support of the electrostatic effect, single molecule studies on conventional kinesins and cytoplasmic dynein have shown that the motor processivity can be enhanced by the addition of positively charged residues in kinesin's neck linker (*44*) and dynein's MTBD (*19*). A similar

electrostatic mediated mechanism has been proposed to explain the processivity of a chimeric kinesin consisting of the catalytic core of KIF1A fused to the conventional kinesin neck linker (*45*). The positively charged (Lysine-rich) region in loop 12 of the KIF1A motor interacts with the tubulin terminal tails and the electrostatic interaction prevents kinesin from diffusing away from the MT.

The initiation of the depolymerization activity may occurs as follows: upon reaching the MT-end, Kip3 transitions to a tightly bound state that most likely involves a conformational rearrangement of loop8, stabilized by additional salt bridges with β-tubulin and interactions between the arginine rich loop 11 and α-tubulin. The loop 8 conformational movement is likely dynamic, however at the MT-end the distribution is biased towards the docking of loop8 on the MT, mediated by the F333-H268 interaction. This reorganization of interactions results in plus-end dwelling and depolymerization activity.

Our analysis of the intramolecular Kip3 interactions and its interaction with the microtubule reveals that key elements for these activities are the arginine-rich loop 11 and the conformation of Loop 8. In support of the role of the L8 conformation in depolymerization activity and motility, non-motile depolymerases of the kinesin-13 family have the loop 8 tip, away from the β-sheet core (Figure 4.10). This is in marked contrast to the loop8 conformation of motile kinesins. I propose a dynamic interaction between positively charged residues in loop8 and β-tubulin at the MT-end. This biases the tubulin conformation toward a bent-conformation not compatible with the MT-end, thus promoting depolymerization.

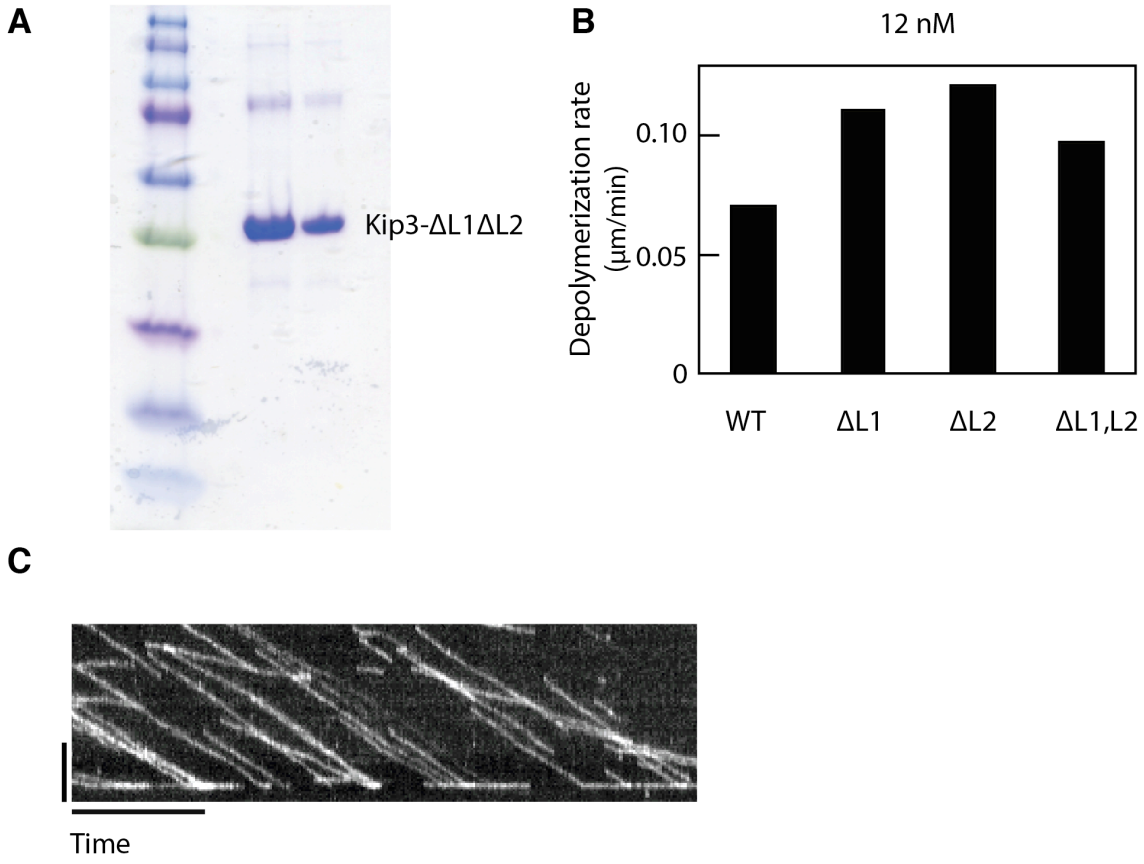


Figure 4.5 Kip3 specific L1 and L2 inserts are dispensable for motility and depolymerization *in vitro*

(A) SDS-PAGE coomassie stained gel of Kip3-ΔL1ΔL2 monomeric construct used for cryo-EM studies **(B)** Depolymerization activity of Kip3 WT, Δloop1, Δloop2 and Δloop1-Δloop2 dimers on GMPCPP-stabilized microtubules. **(C)** Representative kymograph of labeled Kip3-ΔL1ΔL2 dimers moving on a taxol-stabilized microtubule.

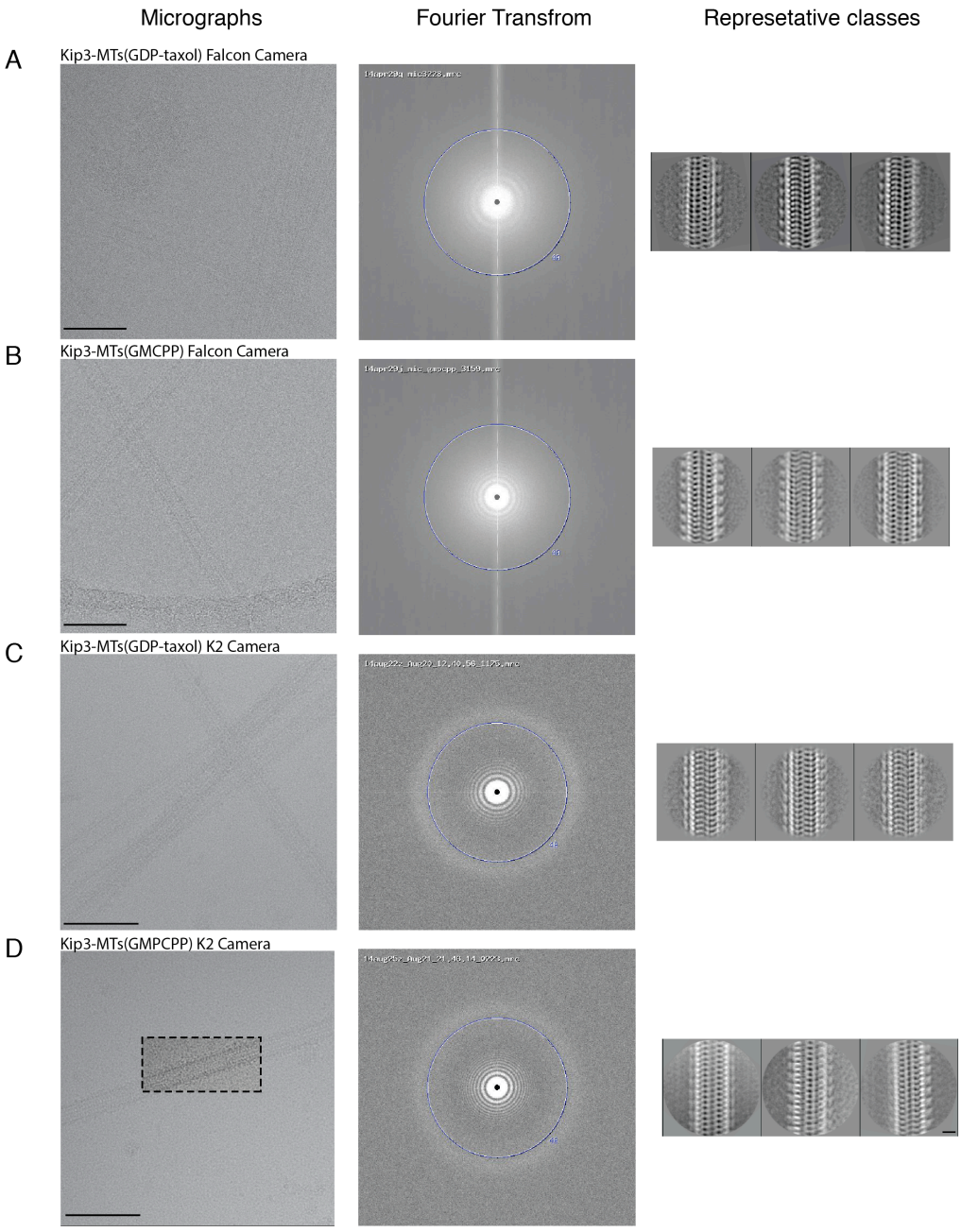


Figure 4.6 Representative Micrographs and classification of different data sets.
(A)-(D) Representative micrographs, corresponding Fourier transform (FT) and representative two-dimensional class averages of Kip3 decorated microtubules. Two data sets were collected using a Falcon direct detector at a 1.07 Å/px and two more using a K2-summit direct detector at a 1.04 Å/px in super resolution and movie mode in a FEI Titan Krios operated at 300 kV.
For the K2 data sets, the sum of 20 aligned frames and their corresponding FT are shown. See Table 4.1 for a summary of collected data. The scale bar on the micrographs is 100 nm, the ring on the Fourier transform is at 1/4 Å and the scale bar on the class averages is 10 nm.

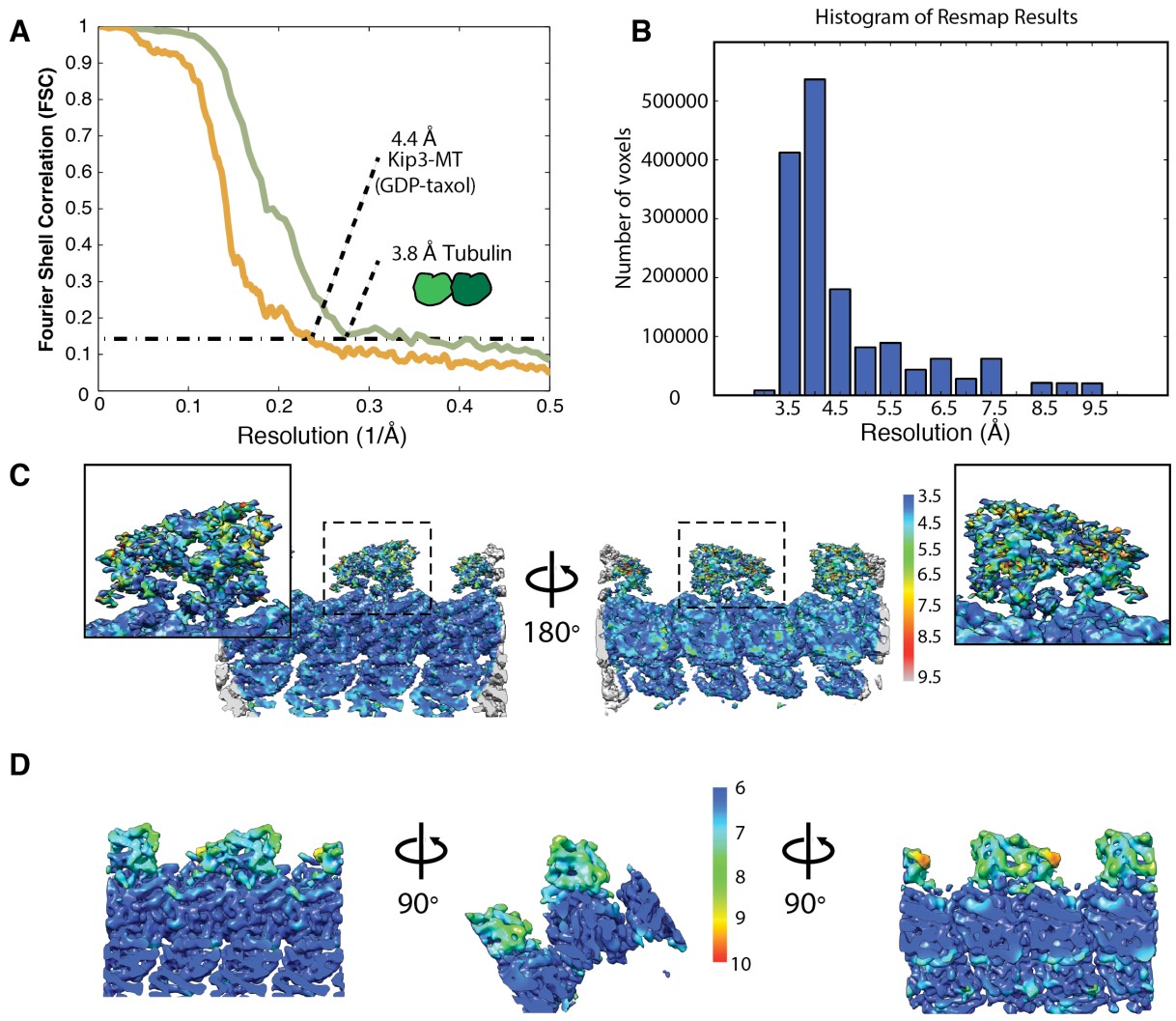


Figure 4.7 Resolution analysis of Kip3-MTs (GDP-Taxol) 3D reconstruction.
(A) Fourier Shell Correlation (FSC) curves of the final 3D reconstruction calculated from half-data sets. The resolution is reported using a cutoff of 0.143. The curves corresponding to the entire reconstruction and one tubulin dimer (GDP-taxol) are shown in orange and green respectively. **(B-C)** A portion of the map comprising one Kip3-tubulin complex was segmented from the final reconstruction and analyzed using ResMap (*28*). The resolution is distributed from 3.5 to 7.5 Å. The tubulin density and the Kip3-tubulin interface have a resolution of 3.5 - 4.5 Å. The map is colored according to the heat map
(D) A similar analysis was carried out using blocres (*29*), different views of the map filtered and colored according to the calculated local resolution are shown. Both studies are consistent in the distribution of resolutions however Bsoft underestimates de resolution of the entire map. This result has been noticed and discussed before in (*28*).

Figure 4.8 Cryo-EM densities of selected regions of tubulin (GDP-taxol)

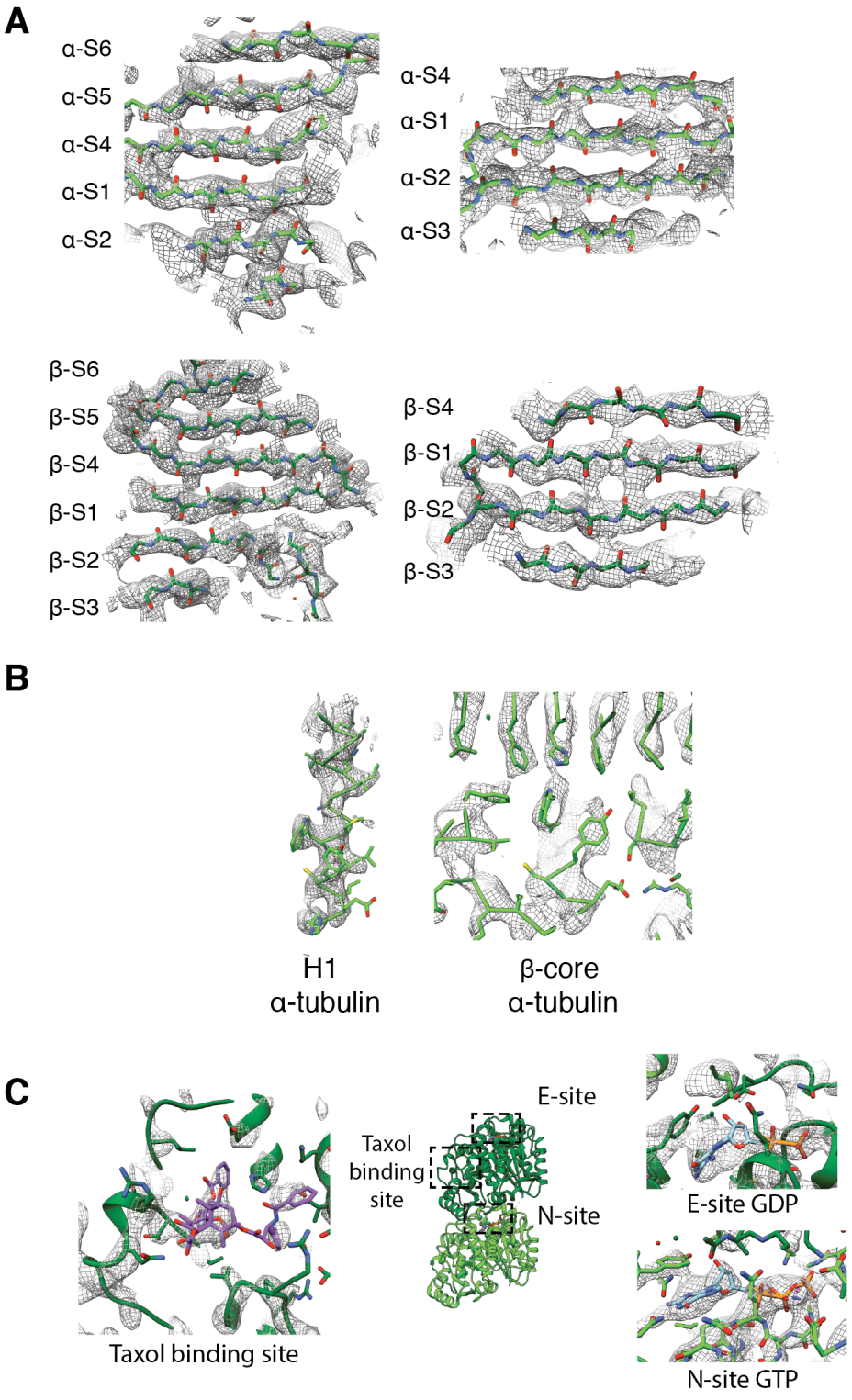


Figure 4.8 Cryo-EM densities of selected regions of tubulin (GDP-taxol) (Continued)

(A) Cryo-EM densities of individual beta strands in α- and β-tubulin. The density is shown as a mesh superimposed on atomic model. The map was low-pass filtered to 3.8 Å and amplified by a temperature factor of -150 $Å^2$. **(B)** Representative densities of selected regions of α-tubulin. Notice that the density of several bulky residues is well resolved. **(C)** Cryo-EM densities corresponding to the nucleotide binding sites and taxol.

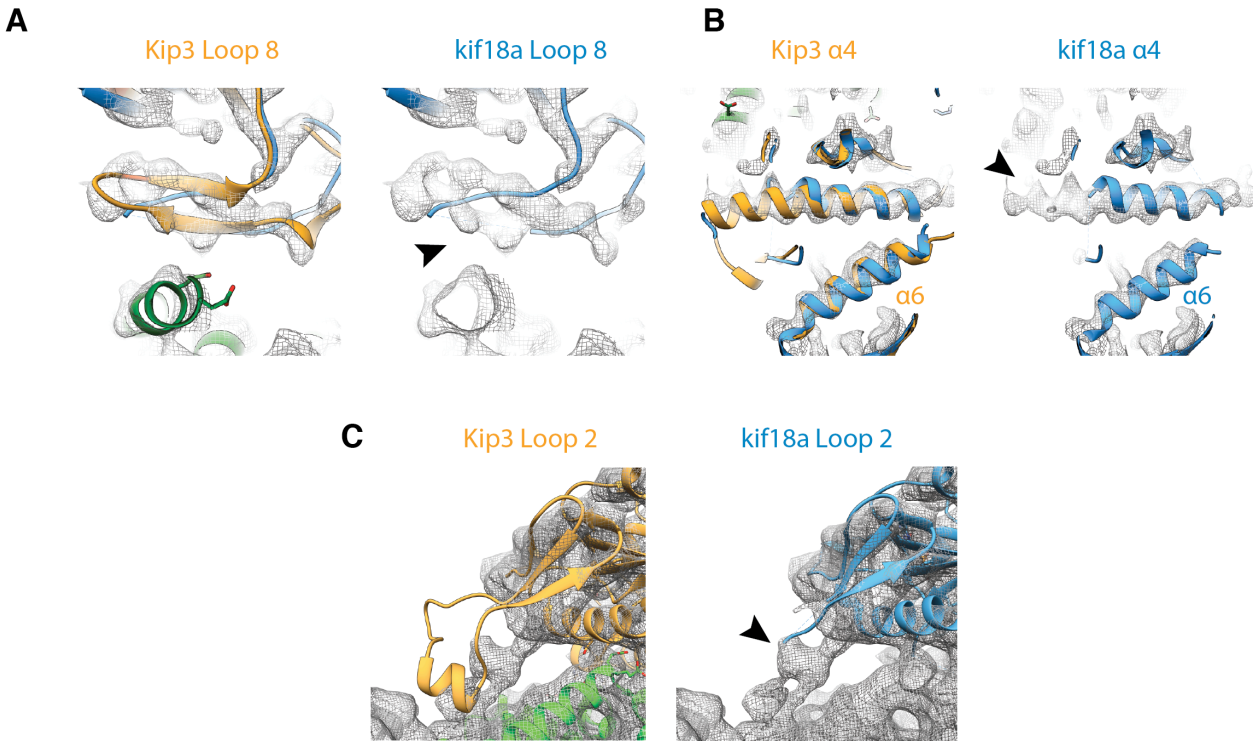


Figure 4.9 Comparison of the MT-bound yeast/Kip3 and free human/Kif18A kinesin-8s models

(A) Views of the loop8, **(B)** α4, α6 and **(C)** loop2 in the models built for the yeast kinesin8/Kip3 obtained by Cryo-EM (this study) and human kinesin8/Kif18A obtained by X-ray crystallography (PDB 3lre) (*11*). The Cryo-EM density for the Kip3-MTs (GDP-taxol) is superimposed on both models. The map was filtered at 4.4 Å and amplified by a temperature factor of -150 $Å^2$ in (A-B) and at 7- 8 Å (local resolution) to display the loop 2 view (C) as it has lower resolution. A portion of α4 and the loops 8 and 2 are not present in the human kinesin8/ kif18A PDB model (arrowheads), in contrast, they are resolved by Cryo-EM.

Figure 4.10 Structural and sequence alignment of the loop 8 and loop 2 region of representative members of the motile, non-motile depolymerase and motile depolymerase kinesins

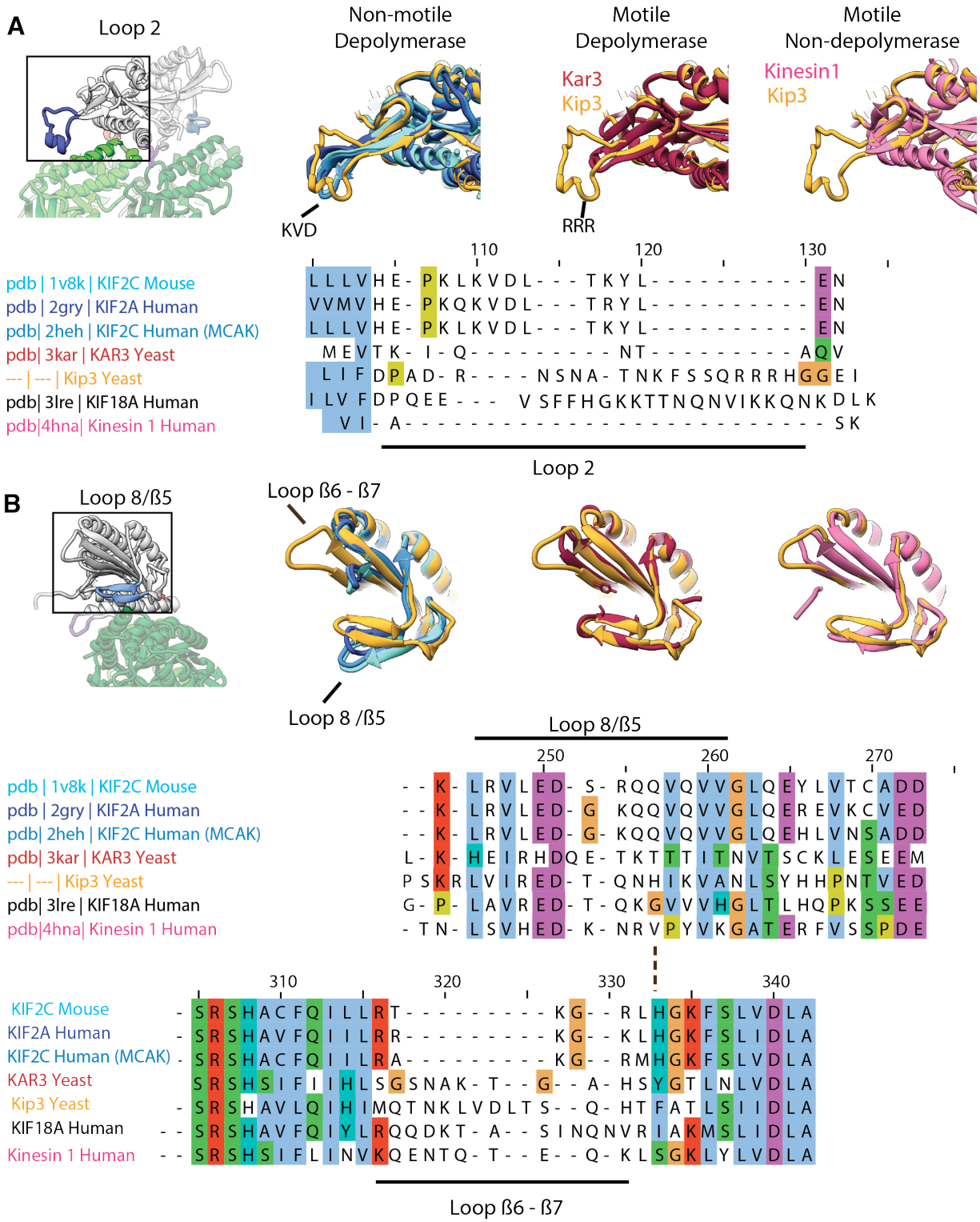


Figure 4.10 Structural and sequence alignment of the loop 8 and loop 2 region of representative members of the motile, non-motile depolymerases and motile depolymerases kinesins (Continued)

The yeast kinesin-8/Kip3 is a plus-end directed motor that dwells at the MT plus-end and depolymerizes GMPCPP-stabilized microtubules, specifically from their plus ends (*6*, *9*). Kip3 has also been shown to be a catastrophe factor on dynamic microtubules *in vitro* (*39*).
(A) Structural alignment of the Loop 2 region of representative members of the non-motile depolymerase (blue), motile depolymerase (red) and motil (pink) kinesin families. The extended loop 2 of members of the kinesin-13 family of depolymerases has been suggested as the element responsible for depolymerazation activity (*12*). Similarly to kinesin-13s, Kip3 has an extended loop region, however replacement of the Kip3 loop 2 for the one of kinesin-1 does not affect Kip3's depolymerization activity (Arellano-Santoyo et al., Unpublished data). **(B)** Structural alignment of the Loop 8 region and β-sheet core. Notice that Kar3 and Kip3 have extended β6-β7 loops when compared to the kinesin-13 family.

Other motile depolymerases such as the yeast kinesin-14/Kar3 have a similar Loop 8 conformation when compared to Kip3. Kar3 is a minus-end directed kinesin shown to have-plus end depolymerization activity. In Kar3 a Tyrosin-Threonine interaction (Figure 4.10 B) could perform a similar function to the F333-H268 interaction observed in Kip3.

The kinesin superfamily has members that perform multiple activities ranging from intracellular transport, MT-end dynamics regulation and MT-sliding. While the kinesin core is highly conserved, fined tuned for ATP hydrolysis, members of the super family have evolved their diverse functionality by modulating intramolecular interactions and their interaction with the microtubule. Our results provide a framework to further dissect the mechanism of the kinesin-8 family and other multi-functional kinesins.

Table 4.1. Summary of Cryo-EM data collected

	kip3-MTs (Taxol)	kip3-MTs (GMPCPP)	kip3-MTs (Taxol)	kip3-MTs (GMPCPP)	MTs (GMPCPP)	kip3-MTs (GMPCPP)
Microscope	Titan Krios	Titan Krios	Titan Krios	Titan Krios	Titan Krios	FEI Polara
Voltage (kV)	300	300	300	300	300	300
Detector	Falcon	Falcon	K2-summit	K2-summit	K2-summit	K2-summit
Frames	1	1	20	20	20	20
Exposure time (s)	1	1	4	4	5	5
Total dose ($e^{-1}/Å^2$)	25	25	40	40	40	40
Processed Micrographs	1121	1183	1194	284	246	643
Pixel size of processed data	1.07	1.07	1.04	1.04	1.04	0.98
Number of extracted particles	49,205	49042	67040	8890	8132	29090
14 PF Particles	4,958	14537	23955			
Final 14 PF particles		7209	14934			
Asymmetric units in 14 PF		100,926	209,076			
Resolution 14PF map	ND	5.7	4.4			
13 PF Particles	7,580	3402	29154			
Final 13 PF particles			19532			
Asymmetric units in 13 PF			253,916			
Resolution 13PF map	ND	ND	4.4			

Acknowledgements

We thank C. Sindelar (Yale), V. Ramey (UC-Berkeley) and Gabriel Lander (UC-Berkeley), for sharing processing scripts and helpful advice, M. Strauss (Harvard), Zhihen Yu (HHMI-Janelia) and Jason de la Cruz (HHMI-Janelia) for help collecting EM data. Hugo Arellano-Santoyo for reading the first version of this chapter, as well as all the members of the Leschziner and Pellman Labs for advice and helpful discussions. EM data was collected at the EM facility of the Howard-Hughes Medical Institute at Janelia. Image processing and MD simulations were run on the Orchestra cluster at Harvard Medical School and the Odyssey cluster supported by the FAS Science Division Research Computing Group, Harvard University. This work also used the Extreme Science and Engineering Discovery Environment (XSEDE), which is supported by National Science Foundation grant number ACI-1053575.

References

1. A. Akhmanova, M. O. Steinmetz, Tracking the ends: a dynamic protein network controls the fate of microtubule tips. *Nat Rev Mol Cell Biol* **9**, 309–322 (2008).

2. D. R. Drummond, Regulation of microtubule dynamics by kinesins. *Seminars in Cell and Developmental Biology* **22**, 927–934 (2011).

3. K. Roberts, J. S. Hyams, *Microtubules* (1979).

4. T. Mitchison, M. Kirschner, Dynamic instability of microtubule growth. *Nature* (1984).

5. X. Su, R. Ohi, D. Pellman, Move in for the kill: motile microtubule regulators. *Trends in cell biology* **22**, 567–575 (2012).

6. V. Varga *et al.*, Yeast kinesin-8 depolymerizes microtubules in a length-dependent manner. *Nature Publishing Group* **8**, 957–962 (2006).

7. V. Varga, C. Leduc, V. Bormuth, S. Diez, J. Howard, Kinesin-8 motors act cooperatively to mediate length-dependent microtubule depolymerization. *Cell* **138**, 1174–1183 (2009).

8. X. Su *et al.*, Microtubule-sliding activity of a kinesin-8 promotes spindle assembly and

spindle-length control. *Nat Cell Biol* **15**, 948–957 (2013).

9. M. L. Gupta, P. Carvalho, D. M. Roof, D. Pellman, Plus end-specific depolymerase activity of Kip3, a kinesin-8 protein, explains its role in positioning the yeast mitotic spindle. *Nature Publishing Group* **8**, 913–923 (2006).

10. X. Su *et al.*, Mechanisms underlying the dual-mode regulation of microtubule dynamics by Kip3/kinesin-8. **43**, 751–763 (2011).

11. C. Peters *et al.*, Insight into the molecular mechanism of the multitasking kinesin-8 motor. *EMBO J* **29**, 3437–3447 (2010).

12. T. Ogawa, R. Nitta, Y. Okada, N. Hirokawa, A Common Mechanism for Microtubule Destabilizers—M Type Kinesins Stabilize Curling of the Protofilament Using the Class-Specific Neck and Loops. *Cell* (2004).

13. C. A. Moores, R. A. Milligan, Lucky 13-microtubule depolymerisation by kinesin-13 motors. *J. Cell. Sci.* **119**, 3905–3913 (2006).

14. P. Hovland, J. Flick, M. Johnston, R. A. Sclafani, Galactose as a gratuitous inducer of GAL gene expression in yeasts growing on glucose. *Gene* **83**, 57–64 (1989).

15. G. C. Lander *et al.*, Appion: an integrated, database-driven pipeline to facilitate EM image processing. *J Struct Biol* **166**, 95–102 (2009).

16. J. A. Mindell, N. Grigorieff, Accurate determination of local defocus and specimen tilt in electron microscopy. *J Struct Biol* **142**, 334–347 (2003).

17. T. Ogura, K. Iwasaki, C. Sato, Topology representing network enables highly accurate classification of protein images taken by cryo electron-microscope without masking. *J Struct Biol* **143**, 185–200 (2003).

18. V. H. Ramey, H.-W. Wang, E. Nogales, Ab initio reconstruction of helical samples with heterogeneity, disorder and coexisting symmetries. *J Struct Biol* **167**, 97–105 (2009).

19. W. B. Redwine *et al.*, Structural basis for microtubule binding and release by dynein. *Science* **337**, 1532–1536 (2012).

20. G. M. Alushin *et al.*, The Ndc80 kinetochore complex forms oligomeric arrays along microtubules. *Nature* **467**, 805–810 (2010).

21. G. M. Alushin *et al.*, High-Resolution Microtubule Structures Reveal the Structural Transitions in αβ-Tubulin upon GTP Hydrolysis. *Cell* **157**, 1117–1129 (2014).

22. S. Scheres, ScienceDirect.com - Journal of Structural Biology - RELION: Implementation of a Bayesian approach to cryo-EM structure determination. *J Struct Biol*

(2012).

23. J. Löwe, H. Li, K. H. Downing, E. Nogales, Refined structure of alpha beta-tubulin at 3.5 A resolution. *Journal of Molecular Biology* **313**, 1045–1057 (2001).

24. E. Egelman, A robust algorithm for the reconstruction of helical filaments using single-particle methods. *Ultramicroscopy* **85**, 225–234 (2000).

25. D. Lyumkis, A. F. Brilot, D. L. Theobald, N. Grigorieff, Likelihood-based classification of cryo-EM images using FREALIGN. *J Struct Biol* **183**, 377–388 (2013).

26. C. V. Sindelar, K. H. Downing, An atomic-level mechanism for activation of the kinesin molecular motors. *Proceedings of the National Academy of Sciences* **107**, 4111–4116 (2010).

27. X. Li *et al.*, Electron counting and beam-induced motion correction enable near-atomic-resolution single-particle cryo-EM. *Nat Meth* **10**, 584–590 (2013).

28. A. Kucukelbir, F. J. Sigworth, H. D. Tagare, Quantifying the local resolution of cryo-EM density maps. *Nat Meth* **11**, 63–65 (2013).

29. J. Heymann, D. Belnap, Bsoft: image processing and molecular modeling for electron microscopy. *J Struct Biol* **157**, 3–18 (2007).

30. E. Pettersen, T. Goddard, C. Huang, UCSF Chimera—a visualization system for exploratory research and analysis. *Journal of ...* (2004).

31. L. Trabuco, E. Villa, K. Mitra, J. Frank, K. Schulten, Flexible fitting of atomic structures into electron microscopy maps using molecular dynamics. *Structure* **16**, 673–683 (2008).

32. L. G. Trabuco, E. Villa, E. Schreiner, C. B. Harrison, K. Schulten, Molecular dynamics flexible fitting: A practical guide to combine cryo-electron microscopy and X-ray crystallography. *Methods* **49**, 174–180 (2009).

33. K.-Y. Chan *et al.*, Symmetry-Restrained Flexible Fitting for Symmetric EM Maps. *Structure* **19**, 1211–1218 (2011).

34. J. C. Phillips *et al.*, Scalable molecular dynamics with NAMD. *J Comput Chem* **26**, 1781–1802 (2005).

35. A. D. Mackerell, M. Feig, C. L. Brooks, Extending the treatment of backbone energetics in protein force fields: limitations of gas-phase quantum mechanics in reproducing protein conformational distributions in molecular dynamics simulations. *J Comput Chem* **25**, 1400–1415 (2004).

36. W. L. Jorgensen, J. Chandrasekhar, J. D. Madura, R. W. Impey, M. L. Klein, Comparison

of simple potential functions for simulating liquid water. *J. Chem. Phys.* **79**, 926 (1983).

37. D. B. Wells, A. Aksimentiev, Mechanical Properties of a Complete Microtubule Revealed through Molecular Dynamics Simulation. *Biophysical Journal* **99**, 629–637 (2010).

38. A. Mitra, D. Sept, Taxol allosterically alters the dynamics of the tubulin dimer and increases the flexibility of microtubules. *Biophysical Journal* **95**, 3252–3258 (2008).

39. M. K. Gardner, M. Zanic, C. Gell, V. Bormuth, J. Howard, Depolymerizing kinesins Kip3 and MCAK shape cellular microtubule architecture by differential control of catastrophe. *Cell* **147**, 1092–1103 (2011).

40. A. Goulet *et al.*, The Structural Basis of Force Generation by the Mitotic Motor Kinesin-5. *Journal of Biological Chemistry* **287**, 44654–44666 (2012).

41. J. Atherton *et al.*, Conserved mechanisms of microtubule-stimulated ADP release, ATP binding, and force generation in transport kinesins. *Elife* **3**, e03680–e03680 (2014).

42. Z. Shang *et al.*, High-resolution structures of kinesin on microtubules provide a basis for nucleotide-gated force-generation. *Elife* **3**, e04686–e04686 (2014).

43. G. Woehlke *et al.*, Microtubule interaction site of the kinesin motor. *Cell* **90**, 207–216 (1997).

44. K. S. Thorn, J. A. Ubersax, R. D. Vale, Engineering the processive run length of the kinesin motor. *J Cell Biol* **151**, 1093–1100 (2000).

45. Y. Okada, N. Hirokawa, Mechanism of the single-headed processivity: diffusional anchoring between the K-loop of kinesin and the C terminus of tubulin. *Proceedings of the National Academy of Sciences of the United States of America* **97**, 640–645 (2000).